Low-temperature Crystallization of Sodium Bismuth Titanate Thin Films

A thesis submitted in partial fulfilment of the requirements for the award of the degree of

DOCTOR OF PHILOSOPHY

in

PHYSICS

by

ANDREWS JOSEPH

Reg.No.13PHPH03



School of Physics
University of Hyderabad
Hyderabad-500046
Telangana, India
January-2023

DECLARATION

I, ANDREWS JOSEPH, hereby declare that the matter embodied in this thesis entitled "Low-temperature Crystallization of Sodium Bismuth Titanate Thin Films" submitted to the University of Hyderabad in partial fulfillment for the award of Doctor of Philosophy in Physics is an original research work carried out by me under the supervision of Prof. K. C James Raju in School of Physics, University of Hyderabad, Telangana, India. I also declare that this work has not been submitted previously in part or in full to this University or any other university or institution for the award of any degree or diploma.

A report on plagiarism statistics from university of Hyderabad library is also enclosed.

Andrews Joseph Reg.No.13PHPH03

Place: Hyderabad

Date: 12.1.2023



CERTIFICATE

This is to certify that the research work presented in the thesis entitled "Low-temperature Crystallization of Sodium Bismuth Titanate Thin Films" submitted by ANDREWS JOSEPH bearing the registration number 13PHPH03, in the partial fulfillment of the requirement for the award of the Degree of Doctor of Philosophy (Ph. D) in Physics at School of Physics is a bonafide work carried out by him under my supervision and guidance.

This thesis is free from plagiarism and has not been submitted previously in part or in full to this University or any other University or institution for the award of any degree or diploma. Further, the student has the following publications before submission of the thesis for adjudication.

- 1. Andrews Joseph, J. Pundareekam Goud, Sivanagi Reddy Emani, K. C. James Raju "Study of amorphous and crystalline phases of sodium bismuth titanate thin films by optical and Raman spectroscopy," J Mater Sci: Mater Electron 28:4362–4370 (2017).
- 2. Andrews Joseph, S. R. Emani, and K.C James Raju, Optical properties of sodium bismuth titanate thin films, Ferroelectrics 518 (1), 184 (2017).
- 3. Andrews Joseph, K.C James Raju, Effect of ex-situ microwave annealing of NBT thin films (under preparation)
- 4. Andrews Joseph, Akhil Raman, Arun B and K.C James Raju, The role of laser fluence on the physical properties of NBT thin films (under preparation)
- 5. Andrews Joseph and K.C James Raju Excimer laser-induced crystallization of Sodium Bismuth Titanate Thin films (under preparation).

Conference Proceedings

1. Andrews Joseph, J. Pundareekam Goud, Sivanagi Reddy Emani, and K.C. James Raju "Microwave Dielectric and Optical Properties of Pulsed Laser Deposited Na_{0.5}Bi_{0.5}TiO₃ Thin Film" AIP Conference Proceedings 1731, 080039 (2016).

Conferences/Symposium/ Workshops attended

- 1. Andrews Joseph, J. Pundareekam Goud, Sivanagi Reddy Emani and K.C James Raju, "Microwave Dielectric And Optical Properties Of Pulsed Laser Deposited Na0.5Bi0.5TiO3 Thin Films" 60th DAE Solid State Physics Symposium (DAE-SSPS2015) held at Amity University UP, Noida, Uttar Pradesh during December 21-25, 2015(Poster presentation)
- 2. Andrews Joseph, Processing and Characterization of Thin Films, workshop, UGC-NRC, School of Physics, University of Hyderabad, 2018.
- 3. Andrews Joseph, Sivanagi Reddy Emani and K. C. James Raju, "Optical Properties of Sodium Bismuth Titanate Thin Films" ICTAM-AMF10 during 7-11 Nov.2016 at University of Delhi. (Poster presentation)

Further, the student has passed the following course towards the fulfillment of course work required for Ph.D.

S. No.	Course code	Name	Credits	Pass/Fail
1	PY801	Advanced quantum mechanics	4	Pass
2	PY803	Advanced Statistical mechanics	4	Pass
3	PY804	Advanced electromagnetic theory	4	Pass
4	PY821	Research Methodology	4	Pass

Dean

School of Physics

Place: Hyderabad Date: 12. 1. 2023

DEAN

School of Physics

University of Hyderabad University of Hyderabad HYDERABAD - 500 046

Prof. K. C James Raju School of Physics,

University of Hyderabad.

Dr. K.C. James Raju Professor School of Physics University of Hyderabad Hyderabad-500 046. INDIA

Dedicated to Family and Friends

Acknowledgements

Doctoral research life has been an exciting period for me. I have been benefitted from various persons and institutions from the beginning since I joined the University of Hyderabad till the completion of this thesis. I convey my gratitude to all of them.

I take this opportunity to express my sincere gratitude to my supervising guide and the Dean, School of physics Prof. K.C James Raju. A lot has been learned from him as a research supervisor which needs to be carried forward. I would like to specially thank him for his guidance, valuable scientific discussions, inspiring attitude, and support throughout the research work.

Besides my supervisors, I would like to thank my doctoral review committee members: Prof. S.V.S Nageshwar Rao and Dr. Venkataiah Gorige, for their interest, valuable discussions, insightful comments, and encouragement. I am heartily thankful to the former Deans, Prof. Seshu Bai, Prof. Bindu A Bamba and Prof. Ashok Chatterji, for providing me with the necessary facilities in the School of Physics.

I would like to thank to present and former Vice Chancellors of the University of Hyderabad, Prof B J Rao, Prof. Apparao Podile and Prof. Ramakrishna Ramasamy.

I am grateful to Prof. S.V.S Nageshwar Rao, Prof. M. Ghanashyam Krishna, and Prof. Rajaram, coordinators of the Center for Nanotechnology (CFN), University of Hyderabad (UoH), for allowing me to access clean room facility, and Prof. Seshu Bai, coordinator of UGC-NRC for allowing me to use required characterization facilities.

I am very grateful to my seniors and group mates, Dr. S. Ramakanth, Dr. Ajeeth Kumar, Dr. Sandeep Sharma, Dr. J Pundareekam Goud, Dr. MS Alkathy, Dr. T. Anil, Dr.S. Bashaiah, Dr. S. V. N. Reddy, Dr Suresh, Akhil Raman, Arun, Nikhil, Srikanth, Shivikram, Surjithnath, Rakesh, Sravan Gnanashekar, Bibhudatta, Shiva for their moral support and valuable discussions during my Ph.D.

I would like to greatly acknowledge UoH for providing financial support under the BBL scheme and DST-SERB for providing financial support under various grants and projects.

My sincere thanks to the School of Physics office staff, Mr. Abraham, Mr. Ravi Babu, Mr. Sudharshan, Mrs. Deepika, Mrs. Sailaja, Mrs. Vijaya Lakshmi, Mr. Shekar, Mr. K. Srinivas, Mr. Prasad, Suresh Babu, Mukunda Reddy and Narsimha Rao. I thank Ms.

Sunitha and Ms. Santhosh (FESEM) and Mr. Naresh (XRD) for accepting to help with my experiments, CIL staff, Dr. S. Manjunath, Mr. Suresh, Mr. Pavan kumar, Mr. Sudhakar, Mr. Rajesh, Mr. Nagaraju, and CFN staff, Pankaj, Durgaprasad, Prashanth, Sandya, Grasy and Srikanth for their help and technical support.

I am greatly honoured to pay my deepest gratitude to my Father and Mother Joseph Mathew and Salomi Joseph. I could not have come to this stage without their support. I would like to acknowledge my brother Eltho Joseph for his constant support throughout my life. Finally, I offer my regards to all who supported me during the completion of my work.

Andrews Joseph

Table of contents

		Title	Page No
Ackn	owledge	ements	ii
Table	of cont	ents	iv
List	of figure	S	viii
List	of tables		xiii
Acro	nyms		iv
Abstı	•		iv
11000			
Cha	nter 1•	Introduction	
1.1	_	uction	02
1.2		electrics	02
1.3		skite Materials	04
1.4		free piezoelectrics	06
1.5		equirement and advantages of Laser annealing	07
1.6	Litera	ture survey	08
	1.6.1	Sodium Bismuth Titanate (Na _{0.5} Bi _{0.5} TiO ₃)	08
	1.6.2	Sodium Bismuth Titanate thin films	09
	1.6.3	Laser-induced crystallization	11
	1.6.4	Nucleation and growth	13
	1.6.5	Tunable Microwave Devices	17
1.7	Motiv	ation	18
1.8	Object	tives of the Thesis	19
1.9	Thesis	soutline	20
1.10	Refere	ence	23
Cha	pter 2:	Experimental Procedures	
2.1	Introd	uction	30
2.2	Target	t preparation Procedure	30
2.3	Pulsed	d Laser Deposition	32
	2.3.1	NBT deposition by PLD	33
	232	Laser Annealing Setup	34

2.4	Chara	acterization Technique	35
	2.4.1	X-ray Diffraction (XRD)	35
	2.4.2	Field Emission Scanning Electron Microscopy (FESEM)	37
	2.4.3	UV- visible NIR spectroscopy	39
	2.4.4	Profilometer	40
	2.4.5	Raman Spectroscopy	40
	2.4.6	Dielectric spectroscopy	41
		2.4.6.1 Low frequency dielectric constant of Bulk materials	41
		2.4.6.2 Dielectric spectroscopy of Thin films: Interdigitated capacitor	43
	2.4.7		45
	2.	P-E Loop measurement	46
2.5		References	48
Cha	pter 3:	: In-situ crystallization behaviour of Na _{0.5} Bi _{0.5} TiO ₃	
3.1	Introd	luction	51
3.2	Exper	rimental Details: Deposition of NBT thin film	51
3.3	Resul	ts and Discussions	52
	3.3.1	Structural properties	52
	3.3.2	Microstructural properties	54
	3.3.3	UV -VIS-NIR Spectroscopy	55
	3.3.4	Raman spectroscopy	61
3.4	Micro	owave dielectric properties of NBT thin films	65
3.5	Refere	ences	69
Cha	pter 4:	: Dielectric, Ferroelectric and Tunable Microway	e
Prop	perties	of Na _{0.5} Bi _{0.5} TiO ₃ Thin Films	
4.1	Introd	luction	73
4.2	Depos	sition of NBT thin films	74
4.3	Struct	tural and microstructure properties	75
4.4	Low-l	Frequency dielectric properties of NBT thin films	76
	4.4.1	Room temperature dielectric properties of NBT Thin films	76
	4.4.2	Temperature dependent Impedance spectroscopy	79
4.5	Broad	d band high frequency dielectric measurement	82
	4.5.1	Conformal mapping of IDC structure	82

	4.5.2	Fabrication of IDC	84
	4.5.3	Measurement of permittivity and tunability	85
4.6	Ferroe	electric properties	89
4.7	Concl	usion	91
4.8	Refere	ences	92
Cha	_	Effect of microwave annealing and laser fluence BT thin films	
5.1	Introd	uction	95
5.2	Micro	wave annealing of NBT thin films	95
	5.2.1	Experimental Procedure	95
	5.2.2	Structural characterization	96
	5.2.3	Optical properties	98
	5.2.4	annealed samples	101
5.3	Effect	of laser fluence	102
	5.3.1	Structural characterization	103
	5.3.2	FE-SEM and EDX	104
	5.3.3	Optical Properties	106
	5.3.4	Microwave dielectric properties	109
5.4	Concl	usion	110
5.5	Refere	ences	111
Cha	pter 6:	Laser Induced crystallization of NBT thin films	
6.1	Introd	uction	113
6.2	Laser-	induced crystallization mechanism	114
	6.2.1	Laser annealing as a non-isothermal process.	114
	6.2.2	Transient Pressure Mechanism for Femtosecond Laser annealing	116
6.3	Exper	imental work	117
	6.3.1	Deposition of Amorphous NBT thin films	117
	6.3.2	Laser annealing of NBT thin films	117
6.4	Effect	s of number of laser shots	117
6.5	Effect	of laser fluence	124
6.6	Effec	t of thin film deposition pressure	126
6.7	Effect	of Bismuth deficiency on laser annealing	129
6.8	Broad	band Microwave Dielectric Properties of Laser annealed films	131

	List of Publications	
7.2	Future Scope of work	142
7.1	Summary	139
Chaj	pter 7: Summary and future work	
6.10	References	136
6.10	Conclusions	134
	thin films.	
6.9	Comparison of laser annealing and microwave furnace annealing of	133

List of figures

Chapter-1

Figure No.	Description	Page No.
1.1	Ferroelectric hysteresis loop	03
1.2	Classification of dielectric materials.	04
1.3	Schematic diagram of ABO ₃ perovskite	05
1.4	Piezoelectric coefficient of prominent lead-free materials and PZT.	06
1.5	Laser absorption and subsequent process. Shaded regions represent free plasma	12
1.6	Diagrammatic representation of free energy changes as a function of processing temperature for both amorphous and crystalline phase. Here ΔG denote the driving force for crystallization, Tmp is the melting point.	13

Chapter-2

Figure No.	Description	Page No.
2.1	Ball Mill with Zirconia Jar loaded	31
2.2	Flow chart representation NBT Target preparation process	31
2.3	Pulsed Laser Deposition System	33
2.4	Laser annealing instrumentation	35
2.5	Principles of X-ray Diffraction	36
2.6	Bruker D8 advanced diffractometer for bulk (b) Bruker D8 discovered for thin films (GIXRD).	37
2.7	Electron matter interaction	37
2.8	Block Diagram of FESEM instrumentation	38
2.9	Principle of Energy Dispersion Spectroscopy	39
2.10	(a) UV-VIS-NIR spectrophotometer (b)Transmission spectra of NBT thin film deposited on fused silica	40
2.11	(a) Illustration of stylus profilometer-based film thickness measurement (b)Thickness measurement result for NBT thin films	40

2.12	(a)HR 800 Horiba Jobin Yvon confocal micro-Raman spectrometer. (b) diagrammatic representation of the Raman process	41
2.13	Dielectric measurement set up with furnace	42
2.14	Images of (a) BDS 1200 and (b) Novotherm-HT 1200.	43
2.15	Block diagram of interdigitated capacitor	43
2.16	Block diagrams of stages in photolithography	44
2.17	(a) Microstrip SOLT Standards (Dotted Lines indicate Calibrated Reference Planes) (b) Agilent VNA.	46
2.18	Schematic diagram of the P-E hysteresis loop of Ferroelectric materials [23]	46

Chapter –3

Figure No.	Description	Page No.
3.1	XRD of NBT thin films deposited at various temperatures.	53
3.2	FESEM images of NBT thin films deposited at different substrate temperatures.	54
3.3	Transmission spectra of NBT films deposited at various substrate temperatures and inset show fitted asymptote for Tmax obtained for films deposited at 550°C.	
3.4	(a) The refractive index of NBT thin films deposited at various substrate temperatures (b) The Extinction coefficient (k) of deposited NBT thin films.	
3.5	Variation of dielectric constant and dielectric loss of NBT thin films with wavelength	60
3.6	Deconvoluted Raman spectra of NBT thin films deposited at various temperatures (Here Green lines are individual peak, red lines are cumulative fit and black dots are experimental data). The inset shows the portion where Raman spectra are measured.	
3.7	Raman scattering and conservation of wave vector in a crystal.	64
3.8	The SPDR fixture used for dielectric measurement.	66

Chapter – 4

Figure No	Description	Page No.
4.1	X-Ray Diffraction pattern of NBT thin film on Pt-coated Sapphire.	75
4.2	A schematic of a cross-section of the capacitor structure [8]	76
4.3	FE-SEM image of fabricated IDC	77
4.4	The frequency-dependent (a) dielectric constant (b) dielectric loss tangent of NBT thin film deposited at various temperatures.	78
4.5	Cole –Cole plot of NBT thin films measured at (a) $100 \circ C$ (b) $150 \circ C$ (c) $200 \circ C$	81
4.6	Schematic representation of IDC structure	83
4.7	Process flow for fabrication and measurement of inter-digitated capacitor	84
4.8	Sputtering system	85
4.9	VNA based IDC measurement system.	86
4.10	SOLT Standards (Dotted Lines indicate Calibrated Reference Planes)	87
4.11	Dielectric constant and dielectric loss (tan 8) of NBT thin films at zero and 70V bias voltage measured from 0.5 GHz to 3 GHz using IDC.	87
4.12	Schematic of stored and recoverable energy density from P-E loop.	89
4.13	Room temperature ferroelectric hysteresis loops measured for NBT thin film at various voltages measured at 1KHz	90

Chapter –5

Figure No	Description	Page No.
5.1	XRD of NBT thin films annealed in microwave furnace at various temperatures	97
5.2	Variation of crystallite size in NBT thin films with annealing temperature.	98
5.3	Transmission spectra of NBT films annealed at different temperatures in a microwave furnace	98
5.4	(a) Envelop fit (b) Sellmeier fit for NBT film annealed at 525 °C.	99
5.5	Refractive index and band gap of NBT thin films annealed at various temperatures with microwaves.	100

5.6	Shows the FE-SEM image of NBT thin films ex-situ annealed in (left) conventional and (right) microwave furnaces.	101
5.7	XRD of NBT films deposited at different laser fluences	103
5.8	Variation of crystallite size in NBT thin films with laser fluence.	103
5.9	The FE-SEM image of NBT thin films deposited at various laser fluences starting from 1.4 J/cm2	104
5.10	EDX of NBT thin films deposited at various laser fluence (2J/cm2 to 1.6 J/cm2)	105
5.11	Variation in optical transmittance with laser fluence.	106
5.12	Optical band gap and refractive index with laser fluence during film deposition.	107
5.13	Variation of Oscillator peak energy and refractive index with laser fluence during film deposition.	108
5.14	Microwave frequency dielectric constant and loss with laser fluence during film deposition.	109

Chapter –6

Figure No	Description	Page No.
6.1	Time-temperature curve of showing dynamic nature of laser processing.	115
6.2	Snapshots of the solid-state lattice mending of the nanopore at different progression times by an annealing fluence of 0.89Fth melt (Fth melt- is the fluence required to melt the sample)	116
6.3	Optical images of laser-annealed films for various number of shots. The number of shots increases from top left to bottom right (100 to 20000)	119
6.4	XRD of laser crystallized samples irradiated with various numbers of laser shots	119
6.5	WR-90 cavity connected to the VNA	121
6.6	Raman spectra of NBT thin films laser annealed for 5 K shots (left) Spectra collected from amorphous region (right) Spectra of crystalline region.	123
6.7	XRD of laser crystallized samples irradiated with different laser fluence	124
6.8	Optical images of laser-annealed films for various laser energy densities	125
6.9	XRD pattern of NBT thin film deposited at various pressure and annealed at room temperature	126

6.10	Optical microscopic images of NBT thin film deposited at various pressure and annealed at room temperature.	128
6.11	XRD of NBT thin films deposited at various laser fluence and annealed 10K shots at room temperature	129
6.12	Optical microscopic image of NBT thin films deposited at various laser fluence and annealed with 10K shots at room temperature	130
6.13	Dielectric constant and dielectric loss (tan δ) of NBT thin films at zero and 70 V bias voltage ($E=70KV/cm$) measured from 0.5 GHz to 3 GHz using IDC.	

List of Tables

Chapter-1

Table No.	Table No. Description	
1.1	Electrical properties and processing temperatures of NBT thin films	11
1.2	Laser annealing of various thin films in literature	16

Chapter-2

Table No.	Table No. Description	
2.1	NBT Thin film deposition conditions	34

Chapter-3

Table No.	Description	Page No.
3.1	Lattice constants of NBT thin film deposited at various substrate temperatures	54
3.2	Single oscillator dispersion parameters of NBT thin films deposited at various substrate temperatures estimated by fitting experimental data with Sellmeier formula.	
3.3	The peak position and FWHM of Raman spectra of NBT thin films deposited at different temperatures.	62
3.4	Dielectric characteristics of NBT films determined at 10 GHz.	67

Chapter-4

Table No.	Description	Page No.
4.1	Comparison of various state of art varactor technologies.	74
4.2	Typical equivalent circuit models used for describing the impedance of dielectric materials and their corresponding Nyquist and Bode plots.	80
4.3	Estimated capacitance and resistance values corresponding to each semicircle in the Cole-Cole plot.	82

Chapter- 5

Table No.	Description	Page No.	
5.1	Deposition conditions of amorphous NBT thin films	96	

5.2	Cation atomic percentage of NBT thin films deposited at a different	106	
	laser fluence		

Chapter-6

Table No.	Description	Page No.
6.1	Microwave dielectric properties of NBT thin films annealed with different numbers of annealing shots.	
6.2	Microwave dielectric constant and loss of NBT thin film annealed at a different laser fluence	126
6.3	The Deposition pressure and number of annealing pulses.	127
6.4	Microwave dielectric constant and loss of NBT thin film deposited at various pressure and annealed at room temperature	128
6.5	Microwave dielectric constant and loss of NBT thin film deposited at various laser fluence.	131
6.6	High-frequency dielectric properties of laser-annealed and conventionally annealed NBT thin films	132

List of Symbols and Abbreviations

Units of measurement

m Metre
cm Centimetre
nm Nanometre
Å Angstrom

°C Centigrade (degree)

KHz Kilo Hertz
MHz Mega Hertz
GHz Giga Hertz
h Hour
F Farad

pC Pico Coulomb μC Micro Coulomb

N Newton V Volt

eVElectron-voltGPaGiga Pascal

g Gram W Watt

esu Electrostatic unit

A Ampere

Electrical measurement

Er Relative permittivity

 $tan \delta$ Loss tangent

 ϵ_0 Permittivity of vacuum

 σ_{ac} AC-conductivity χ_{e} Electric susceptibility J Leakage current density

 k_{ij} Electromechanical coupling coefficient $k_{\rm p}$ Planar electromechanical coupling coefficient

 k_{33} Thickness of electromechanical coupling coefficient

 d_{ij} Piezoelectric charge coefficient

 $\begin{array}{ccc} E & & Electric field \\ C & & Capacitance \\ d & & Thickness \\ \Sigma & & Stress \\ s & & Strain \end{array}$

S Electric compliance

g_{ij} Piezoelectric voltage coefficient

P Polarization Dipole moment p \overline{V} Unit cell volume ZImpedance Z'Resistance $Z^{\prime\prime}$ Reactance f_r Resonant frequency Quality factor Q

 P_s Saturation polarization P_r Remnant polarization

 E_c Coercive field ω Angular frequency

Optical measurement

lpha Absorption coefficient n Refractive index E_g Optical bandgap h Planck's constant λ Wavelength c Velocity of light hv Photon energy

Other parameters

 θ Angle

D Crystallite size

FWHM Full width at half maximum

a, b, c Lattice parameters

ρ Density

RT Room Temperature

FE Ferroelectric

Abstract

Ferroelectric thin films are becoming inevitable in all modern electronic devices. The superior piezoelectric properties of these materials are utilized in various sensors and actuators and their voltage-controlled dielectric characteristics were exploited in frequency agile devices. In addition to the prototype application including negative capacitance, recently trenched capacitors for DRAM and memristers became prominent where their ferroelectric behaviour is exploited. The full application potential of ferroelectric oxides is possible by integrating them into semiconductor chips and flexible polymer substrates. The significant challenge for unlocking this potential is the higher crystallization temperature of ferroelectric materials above which they exhibit the best functional properties.

In ferroelectric device applications, lead-based compositions are dominant because of their excellent dielectric, piezoelectric, and ferroelectric characteristics. Despite having outstanding ferroelectric properties, the lead should be replaced since it poses a major risk to both people and the environment. This necessitates the development of lead-free materials with enhanced dielectric and ferroelectric properties. Sodium bismuth titanate (NBT) is a suitable replacement for this purpose, especially in actuator and capacitor applications. Much work is being carried out to improve the characteristics of lead-free materials worldwide by making new composites and controlling the defects. However, the former problem of achieving low-temperature crystallization is not explored. This thesis explores the possibility of using microwave furnace annealing and laser-induced crystallization to achieve the low-temperature crystallization of NBT thin films.

The NBT target is prepared by the solid-state synthesis method in the lab and NBT thin films are deposited from this target using the pulsed laser deposition method. Initially, NBT thin film is deposited at various substrate temperatures and single-phase NBT thin films with R3c space

group are obtained for the films deposited at 600°C. The thin film deposited in substrate temperature in the range of 300°C -450°C shows an amorphous phase, and the film deposited at 500°C is partially crystallized. This is confirmed by optical microscopic images and Raman spectroscopy. The crystallite size and unit cell volume increase with deposition temperature showing improved crystallinity. UV- Vis NIR transmission spectra of all the deposited films are measured and used to calculate the refractive index, extinction coefficient, dielectric constant, and optical band gap. The observed optical dispersion behaviour has been described by a single electronic oscillator model with oscillator energies of 5.85 and 10.37eV for amorphous and crystalline NBT thin films, respectively. Optical properties of the amorphous and crystalline films show a significant difference in their properties, which may arise from the coordination defects and short-range order in amorphous material. The other important observation is the broad Raman overlapping band in the amorphous phase, which is separated by sharper distinct bands in the crystalline phase. This difference stems from the relaxation of conservation laws in the amorphous phase.

The high-frequency dielectric constants of these films were measured using the Split post-dielectric resonator (SPDR) method. The dielectric permittivity at microwave frequency increases with improvement in the crystalline quality of the deposited films. NBT thin films were reported to show good dielectric tunability at low frequencies, but their high-frequency tunability is not measured. Interdigitated capacitor (IDC) structure is fabricated on these NBT thin films, and their dielectric properties are determined using the on-wafer probing method. The tunability of NBT thin film for an applied bias voltage of 70V (E=70KV/cm) is found to be 9.8%. Temperature-dependent impedance properties and room temperature ferroelectric properties (P-E loop) of NBT thin films deposited on Pt-coated sapphire substrate are also investigated. The recoverable energy density determined from the P- E loop was 3.5J/cm³ with an efficiency of 39 %.

Another series of NBT thin films are deposited to investigate the effect of laser fluence on structural, microstructural, and optical properties. The grain size is reduced to 250nm from 400nm with an increase in laser fluence. This may be due to the Bismuth vacancies present in the film deposited at low laser fluence. The optical band gap does not substantially vary with laser fluence, but the refractive index and oscillator peak energy determined by fitting to a single oscillator model show a decrease with an increase in laser fluence.

In order to reduce the crystallization temperature, microwave furnace annealing is explored first. Unlike traditional furnace heating, microwave processing is a volumetric heating process from inside the materials resulting from its interaction with electromagnetic waves. This study shows that the onset of crystallization is reduced, and improved grain formation is obtained for microwave processing compared to the conventional annealing procedure. Even though the crystallization temperature of NBT thin film is reduced by this method, still the processing temperature is about 500°C to obtain a crystalline phase.

The other method employed to reduce the crystallization temperature is the laser-induced crystallization method. There are many models describing the laser annealing process depending on the material properties and type of laser. Dielectric thin films usually possess less thermal conductivity and diffusivity, causing confinement of laser thermal energy to narrow regions leading to localized crystallization. Another prevailing theory prominently used in femtosecond laser annealing is the shock wave-induced lattice mending process. According to this theory, lattice mending commences by surface nucleation followed by the shear stress applied on the defect region by the shock wave generated because of the laser irradiation and subsequent lattice repair.

The NBT thin film deposited at 300°C is transferred to a similar chamber with a concave lens. The sample is kept inside the chamber in ambient conditions, and the KrF excimer laser of

248nm wavelength is irradiated on the samples. Initially, an NBT thin film of thickness 200 nm is deposited at a working pressure of 3x10⁻² mbar and temperature of 300°C. The films show no evidence of crystalline nature until the number of laser annealing shots was in the range of 10,000. But the microwave dielectric constant monotonically increases with annealing laser pulses and film annealed for 5,000 shots showing a partially crystalline nature in optical images and Raman spectra. Then the effect of laser fluence on crystalline quality is also explored by varying the energy density of the annealing beam from 60mJ/cm² to 90mJ/cm². The higher laser energy density of 90mJ/cm² is deteriorating the crystallinity (reduced crystallite size and permittivity) by damaging the film as evident from the optical image. A substantial improvement in the grain size and fraction of crystallized area is observed for films deposited at low laser fluence containing bismuth deficiency and also for the films deposited at lower working pressure (9 x10⁻³mbar). This may be due to enhanced solid-state diffusion aided by the oxygen vacancies present in these films. There are many studies on the optimization of laser parameters to obtain laser-induced crystallization. But studies addressing the role of material parameters is rare, but such investigations are important to understand the mechanism of laser annealing and the extension of laser annealing to a wide class of materials.

Chapter 1 Introduction

1.1 Introduction

Ferroelectrics have drawn considerable research interest in the past few decades as functional oxide materials to supplant semiconductors in various applications. They have been studied for a diverse range of applications such as dielectric capacitors, piezoelectric sensors, actuators, high-frequency tunable devices like filters and phase shifters, optoelectronics, spintronics, field-effect transistors, IR detectors, non-volatile memories, and magneto-electric devices to name some. PbTiO₃-based materials were explored widely for the above application because of their higher piezoelectric characteristics. PbZrTiO₃, PbZnNbO₃ and related compositions are also being used in some key applications. The toxicity of lead has emerged as a serious environmental and health concern in the recent past, and the search for suitable alternatives is currently a major progressing effort. [1-9]

Even though ferroelectrics possess superior physical and chemical properties, their high processing temperature and the presence of lead in some prominent compositions hinder their application in industry. Rapid thermal annealing (RTA), Microwave annealing, suitable doping and UV irradiation etc are used to reduce the crystallization temperature and solve the former problem. Later problem is being addressed by exploring various promising lead-free alternatives like BaTiO₃, Na_{0.5}Bi_{0.5}TiO₃, (K,Na)NbO₃, etc.

1.2 Ferroelectrics

Ferroelectric (FE) materials are a class of insulators exhibiting reversible (by applying electric field) spontaneous electric polarization. The polarization vs E-field curve of ferroelectric materials is a nonlinear curve analogous to the M-H loop of Ferromagnets. A typical P-E loop of FE is depicted in Figure 1.1

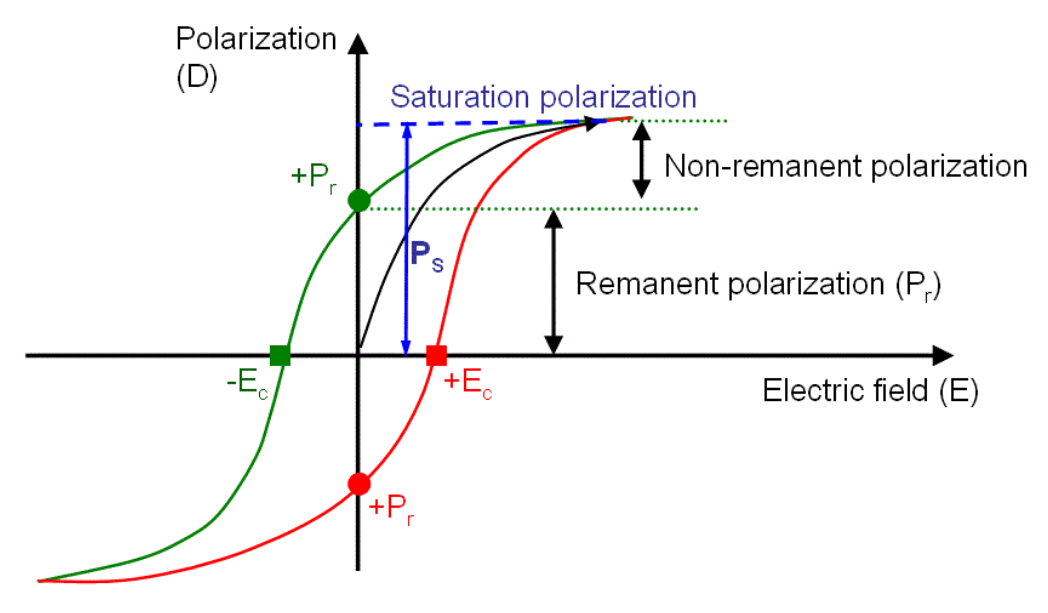


Fig 1. 1: Ferroelectric hysteresis loop

In the initial region (when E is less) of the curve, there is a linear growth of polarization with the applied field. Then the polarization saturates after all the favourable domains are oriented in the field direction. Once we reach saturation and reduce the field and reach zero fields, we get remnant polarization, and by reducing the field further in negative polarity, we obtain zero polarization at a particular field known as the coercive field. There are many potential measurement artifacts associated with the ferroelectric hysteresis loop. They are described in the classic book of Lines and Glass [1]. Hence to ensure the existence of ferroelectricity from hysteresis loops in a full proof manner, the hysteresis loop is expected to have saturation and a concave non linear region.

Of 32 crystal classes [10-12], 21 are non-centrosymmetric, of which 20 exhibit the piezoelectricity. In centrosymmetric crystals, first-order net deformation in an electric field is zero. They only exhibit a second-order electrostrictive effect. Among the piezoelectric classes, 10 of the crystal class show spontaneous polarization, and they are called Pyroelectric as their polarization is temperature dependent. In short, ferroelectrics are subgroups of pyroelectric

materials, which in turn is a subgroup of piezoelectric materials. Hence ferroelectrics are materials with both piezoelectric and pyroelectric characteristics (Fig 1.2).

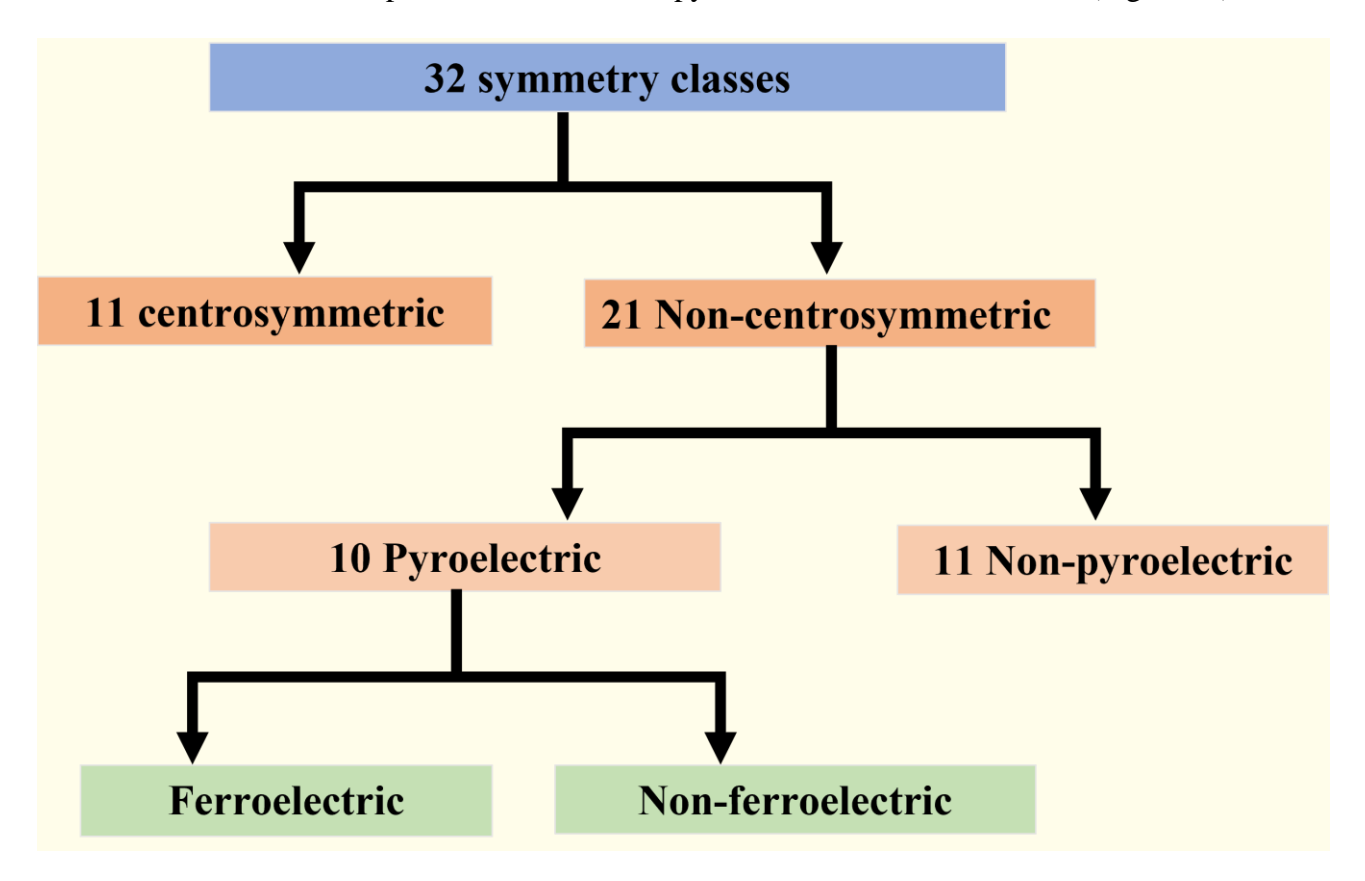


Fig 1. 2: Classification of dielectric materials.

Ferroelectrics are further classified into Tungsten bronze, Perovskite (ABO₃), Pyrochlore, and Bismuth layered structures. All the materials prepared as a part of this work have a Perovskite structure.

1.3 Perovskite Materials

Perovskite oxides are one of the versatile classes of materials having an ABO₃ structure and exhibiting a huge variety of properties, including ferroelectric, magneto-electric, ferromagnetic, antiferromagnetic, linear and nonlinear electro-optical as well as superconducting properties. This is possible because the cation sites in the perovskite can

accommodate lots of elements without breaking the structure [13-16]. Gustav Rose made the initial discovery of the perovskite, which bears the name of Russian Mineralogist L. A. Perovski. [17]. Perovskite materials encompass 15 possible space groups, among them the *pmma* group as their ground state. In the ABO₃ structure, the corners are occupied by the A cations and the Body centre by the B cation and the face centres are filled with oxygen anions, as shown in Fig1.3. The electrical neutrality of the structure is ensured by the condition that the sum of the ionic charge of the A and B cations is equal to +6 so that it balances with the charge of the three oxygen atoms.

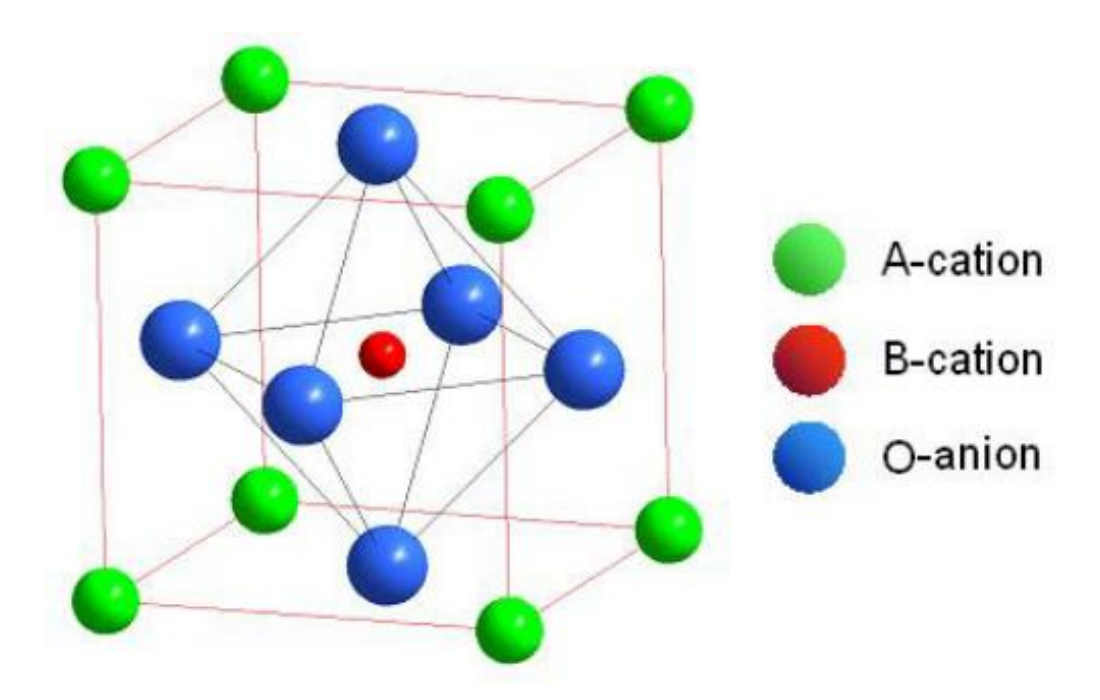


Fig 1. 3: Schematic diagram of ABO3 perovskite

Goldschmidt proposed a relation based on ionic radii of the cation and anions to discern the stable perovskites known as Goldschmidt's tolerance factor (*t*) [18].

$$t = \frac{A_R + O_R}{\sqrt{2(B_R + O_R)}} \tag{1.1}$$

A_R= ionic radii of the A site atoms, B_R= ionic radii of the B site atoms

 O_R = ionic radii of oxygen ions

The value of t ranges from 1 to 0.75 is considered a stable perovskite structure with t=1 for corresponds to cubic and t lesser than 1 for rhombohedral structure, and t greater than 1 for hexagonal structure. If the A site cation radius increases relative to the B site ion, the t value rises, and vice versa.

1.4 Lead-free piezoelectrics

Electronic devices based on lead have been restricted because of their environmental and health hazards. High piezoelectric and electromechanical characteristics of PZT in the vicinity of morphotropic phase boundary (MPB) made PZT and associated compositions the most used ferroelectric ceramics for transducers and various other applications. The strict environmental regulation on lead generates a resurgence in the field of lead-free ferroelectric material. There are three main types of lead-free materials which are sodium potassium niobate (KNN) based (known for high piezoelectricity), barium titanate (BTO) based (known for Room temperature Curie temperature), and sodium bismuth titanate based (known for high mechanical quality factor) ferroelectrics. Figure 1.4 shows the piezoelectric coefficient of these materials and compares them with PZT.

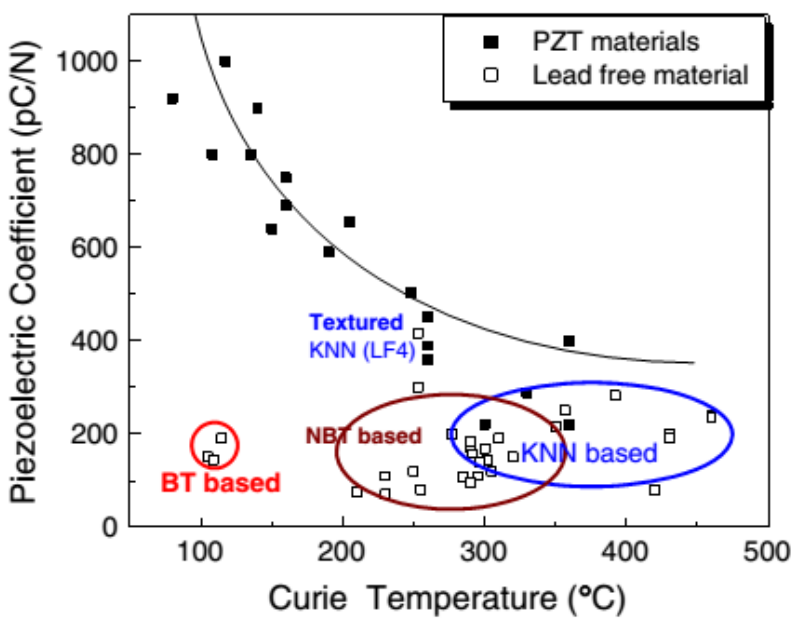


Fig 1. 4: Piezoelectric coefficient of prominent lead-free materials and PZT [19]

1.5 The requirement and advantages of Laser annealing

The advent of ion implantation as a space-saving approach of doping the wafers with regulated amounts of impurities to achieve the necessary size reduction in VLSI circuits has thrown in new challenges in semiconductor processing. The crystalline surface needed to be repaired due to damage caused by the high-energy ion beams. The major problem created by ion implantation is the conversion of silicon to an amorphous phase by this high-energy ion bombardment. Conventional furnace-based annealing was not a proper solution to recrystallize this silicon because of the smaller size of the device and the thermal distortions caused by this universal heating. Hence pulsed ruby lasers were began to be used for repairing the damage caused by ion implantation to the silicon crystal [20]. Laser annealing prevents thermal conduction into the bulk of the silicon by heating only a thin surface layer of the wafer. Hence laser annealing does not develop any flatness of the wafer.

IC dimension reduction is achieved by the direct integration of high k material with silicon. But the ever-increasing demand for improved performance requires high k and voltage tunable ferroelectrics to be integrated with silicon technology. The functional properties of ferroelectric materials are only exhibited in its crystalline phase, and the crystallization temperatures of these materials are very high. Hence laser annealing is a viable solution to crystallize these materials at low temperatures. This also comes with an additional advantage that the low processing temperature enables them to be utilized in upcoming flexible devices. These flexible devices are built on low melting point flexible substrates, which often cannot withstand over 350°C. This poses a great challenge to integrating these functional materials in next-generation flexible and wearable electronic devices. In addition to these, the requirement of huge energy for manufacturing them at high temperatures is

also a serious environmental concern for the sustainable development of these manufacturing industries.

Laser annealing methods are highly compatible with the on-chip integration of ferroelectric thin films. The possibility to control many laser process parameters, such as laser power, pulse duration, and scanning velocity, help to attain a variety of matter- radiation interaction conditions suitable for laser annealing of a wide set of materials. Laser annealing is fast and localized, permitting fine control over the material properties.

The rates of conventional annealing or even rapid thermal annealing are orders of magnitude slower than those attained with laser annealing method. [21].

1.6 Literature survey

1.6.1 Sodium Bismuth Titanate (Na_{0.5}Bi_{0.5}TiO₃)

The Sodium Bismuth Titanate (NBT) was first introduced by Smolenskii et al. [22] in the year of 1960. However, due to its weak piezoelectric response when compared to PZT ceramics, it did not garner much attention until the last 2 decades. In the last decades, the environmental hazards of lead have become a severe concern, and a replacement is widely sought. The superior piezoelectric properties of Pb-based materials originate from the presence of 6s² lone pair electrons on the Pb²+, which promote large structural deformation and a strong electromechanical coupling [23,24]. Bismuth-based materials also contain lone pair electrons associated with Bi³+, which serves as the basis for exceptional FE characteristics exhibited by them. Due to its high remnant polarization (38μC/cm²) and very high FE phase transition temperature along with superior dielectric characteristics, NBT is regarded as one of the suitable material systems to replace lead-based systems [25, 26]. However, there are certain limitations for the direct practical applications of NBT ceramics such as their inferior piezoelectric properties, large ionic conductivity and high

coercive field ($E_c \sim 80 \text{ kV/cm}$) and associated difficulty in poling. In addition to this, the volatile nature of Bi and Na increases the difficulty to obtain densified NBT ceramics.

1.6.2 Sodium Bismuth Titanate thin films

NBT ceramics were studied extensively because of its superior piezoelectric, ferroelectric and energy storage response, which led to investigating the properties of NBT in thin-film form for various applications such as sensors, actuators, optoelectronics, memories, microwave tunable and energy harvesting devices [27–30]. Apart from these, Crystalline NBT thin films with good quality were grown at relatively low temperatures compared with similar ferroic oxides [31]. NBT thin films in pure and modified phases have been fabricated by different methods. Several researchers have prepared NBT thin film by solgel process (SG) or spin coating [28, 32], RF magnetron sputtering [33], chemical solution deposition (CSD) [34], and pulsed laser deposition (PLD) [35-37], of these, the PLD is the most flexible technique used widely to deposit thin films. However, depositing the NBT films in a single phase is tricky because of the volatile nature of both Sodium and Bismuth. Therefore, NBT targets with an excess amount of Na and Bi were often used to synthesize these films [38].

The target stoichiometry and the PLD deposition parameters were found to have a significant impact on the NBT growth characteristics and the final properties [39-41]. Therefore, adopting optimum growth conditions is a need for producing high-quality films. Similarly, modifying the composition (by adding different oxides, such as BaTiO₃ or SrTiO₃ or acceptor doping) of the films slightly enhances or deteriorate various properties exhibited by NBT like conductivity, electro caloric effect, resistive switching and piezoelectric properties. For instance, (1–x) (NBT)-x (BTO) with x around 0.06–0.1 shows MPB with high permittivity. Consider another example from the ceramics solid solution with SrTiO₃ (STO). With an increment in STO content, the ferroelectric phase transition

temperature abruptly decreases, as investigated by Hiruma, Y. et al. [42, 43]. Zhen Fu et al. deposited the (1-x)NBT- xSTO thin film by solid solution and investigated the low-frequency tunability and found that tunability decreased and the figure of merit increased with Sr content in the films [44]. Recently, microwave dielectric properties of NBT-0.08BTO have been measured and its utility in integrated tunable components for RF applications in the Wi-Fi frequency band is demonstrated by L. Huitema et al. [45]. The energy storage capacity of NBT thin films synthesised by the SG method is investigated by Fang Wang et al., and they have obtained an energy storage density of 23.3J/cm³ and an energy efficiency of 61.6% [46].

The effect of acceptor and donor co-doping on the films prepred by chemical solution deposition method (CSD) is investigated by PP Lv et al. [47]. They found that mobile oxygen vacancies could be arrested by the synergistic behaviour of high-valence W⁶⁺ and low-valence Ni²⁺ ions. Chao Yun et al. fabriacted and demonstrated the memrister device with NBT thin film with large ON/ OFF resistive switching at low voltages [48].

In order to make these thin films compatible with semiconductor technologies, the processing temperature of NBT thin film should be reduced. Such an effort is very rare in literature. The only available study found is carried out by Fabien Remondiere et al. [49] They used a modified sol–gel route to crystalize NBT thin films by using a pyrolysis temperature of 460°C. Table 1 summarises the processing temperature and dielectric characteristics of NBT and related films published in the literature.

Sample	Preparation	Processing	Dielectric	Tano	Tunability	Reference
	Method	temperature(°C)	constant			
NBT-BTO0.08	sol-gel method	800	205 at	0.15	30% at	[45]
			2.5GHz		2.45GHz	
(1-x)NBT-x	sol-gel method	Above 500	347 at	0.05	65 %	[44]
STO			100kHz		1 kHz	
NBT	RF magnetron	650	540	-	-	[50]
	sputtering		10kHz			
NBT	sol-gel method	700	405 at	0.029	-	[46]
			1 kHz			
W and Ni co-	chemical solution	520	295 at	0.18	-	[47]
doped NBT	deposition method		100 kHz			
	(CSD)					
Na _{0.5} Bi _{0.5} (Ti _{0.99}	CSD	500	400	0.122	29.36%	[53]
Fe _{0.01})O _{3-δ}			100 KHz		100 KHz	
Na _{0.5} Bi _{0.5}	CSD	500	263	0.067	-	[51]
(Ti0.98Zr _{0.02})O ₃			100 KHz			
NBT	PLD	700	258	0.0038	-	[52]
			(5 GHz)			

Table 1. 1: Electrical properties and processing temperatures of NBT thin films

1.6.3 Laser-induced crystallization

The band structure of a material determines the method of photon absorption. The absorption in dielectrics and semiconductors is caused by resonant excitation, which primarily involves inter-band electronic transitions. The excitation and absorption are limited in the case of materials with band gaps (E_g) higher than the incident laser energy. However, successive multiphoton excitation processes via defect states and non-linear multiphoton absorption may cause inter-band transitions at higher laser intensity. Additionally, sub-bandgap excitation is frequently permitted by defect or impurity states. Strong inter-band excitation of electrons will take place if the laser wavelength is such that the laser beam is of higher energy than E_g . The phonons receive energy from the excited electrons, which amplifies the lattice vibrations.

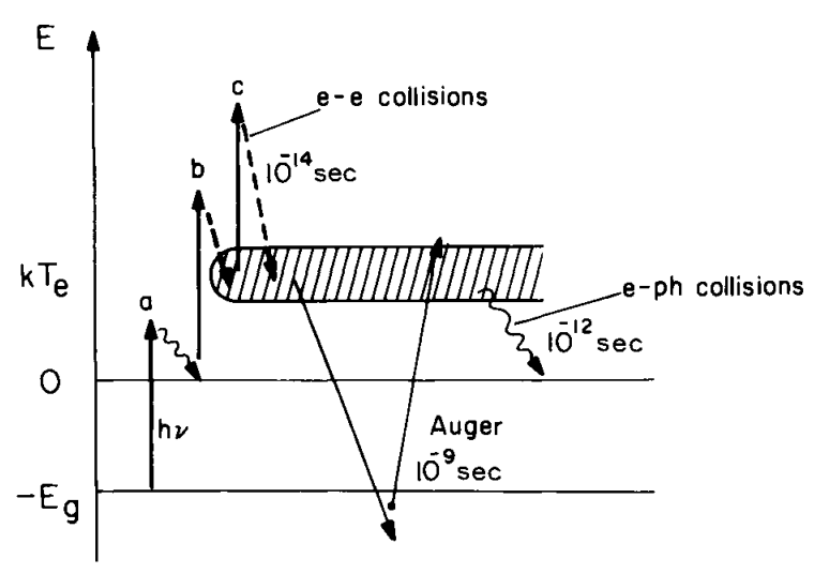


Fig 1. 5 Laser absorption and subsequent process. Shaded region represent free plasma [50]

In semiconductors or insulators, intra-band transitions may happen at high temperatures because of the availability of more charge carriers. The material is thermalized by electron-electron and electron-phonon interactions brought about by the laser-induced interband or intraband electronic transition. The process of electron-hole recombination restores the equilibrium state over a period of time that relies on the properties of the material. The total result is the transformation of electronic energy from the incident laser beam into heat.[54] Figure 1.5 depicts a schematic of a material absorbing laser light after being exposed to photons with energies greater than its characteristic bandgap. This produces free carriers, which can lead to more absorption, known as free carrier absorption. These excited electrons thermalize, creating a dense electron plasma (shaded region), before eventually losing energy. Unlike conventional annealing, the depth of crystallization and energy absorption is governed by the optical characteristics of the material. Laser intensity or energy reaching a depth (x) from the surface may be expressed as

$$I(x) = I_0 (1 - R)e^{-\alpha x}$$
 (1.2)

Where I is the laser energy at depth x from the top surface and I_0 is the laser energy at the surface and R represents the reflectivity, and α denotes the Absorption Coefficient of the

material. The 1- D heat diffusion equation may be used to describe the heat transport across the film's surface to its bulk and is given by eq (1.3) [54]

$$\frac{\partial T}{\partial t} = \frac{\alpha}{\rho C_p} I(z, t) + \frac{1}{\rho C_p} \frac{\partial}{\partial z} \left(\kappa \frac{\partial T}{\partial z} \right)$$
 (1.3)

Here T is the temperature α is the absorption coefficient C_p denotes heat capacity and I is the laser intensity and κ represent thermal conductivity.

1.6.4 Nucleation and growth

Thermodynamic and kinetic variables are involved in the conversion of the amorphous to crystalline phase. Thermodynamically the crystallization driving force is proportional to the difference in material free energies. Fig. 1.6 shows the Gibbs free energy for the film's initial (amorphous) and final (crystalline) states with temperature. This transformation's driving force (G) is always greater at low temperatures. Film crystallization requires crystal nucleation. This nucleation can occur inside the amorphous bulk (homogeneous nucleation) or at film boundaries (heterogeneous nucleation)

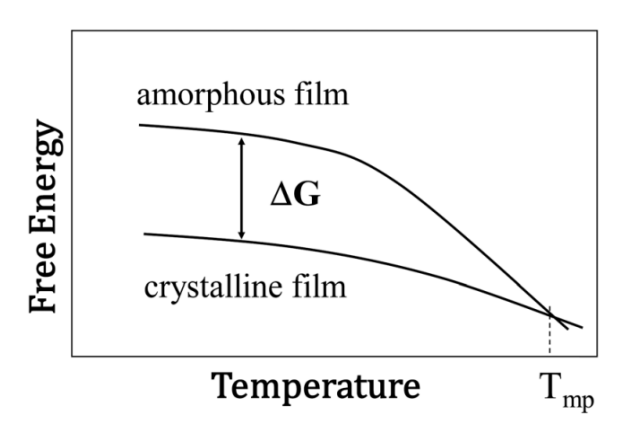


Fig 1. 6: Diagrammatic representation of free energy changes as a function of processing temperature for both amorphous and crystalline phase. Here ΔG denote the driving force for crystallization, Tmp is the melting point.[51]

 ΔG is related to entropy, enthalpy and the difference between the specific heats of the amorphous and crystalline phases in most cases. When estimating the crystallization driving

force for thin films, additional contributions from interfacial energy must be taken into account [55].

Fig. 1.6 shows that crystallization is simpler at low temperatures, where nucleation barriers are smaller. Kinetic variables influence the quantity of crystal nuclei generated and subsequent crystal development. Atoms must rearrange to form crystalline nuclei, and the energy required for this process is obtained from substrate temperature.

In the semiconductor industry, laser-induced crystallization is given a great deal of attention, and there are a substantial number of papers written on the topic of laser annealing of silicon by the use of an excimer laser. The identification of the mechanism responsible for the phase transformation, as well as the resulting microstructure of the Si films, is produced by laser-induced crystallization (LIC) on SiO₂. In the low energy density domain, it is proved that grain size grows larger as energy density grows higher. They made the discovery that the transition zone is an effective regime for the production of polycrystalline Si with broad grain sizes [56]. For the LIC of Sb₂S₃, Sb₂Se₃, and Sb₂Te₃ semiconductor films, a continuous wave from a laser that produces sufficient power is applied. The phase change that happens in all three of the compounds is found to be caused by the photothermal process. Also, it is understood that the amount of power necessary for optical transmission varies with the thickness of the coating.

The amount of power required for optical contrast at an irradiation spot can vary from case to case and film thickness to thickness. For the samples described above, the optimal power density was determined to be 100W/cm² [57]. On the other hand, it was discovered that this technology is applicable and helpful for ferroelectric thin films as well. The inherent electric field tunability of ferroelectric thin films is widely utilized in ferroelectric RAM (Fe-RAM) and microelectromechanical systems (MEMS) and many other high-frequency devices. Hence worldwide research groups are largely interested in investigating the laser annealing

possibilities of different ferroelectric thin films. Laser annealing can be performed on many different types of materials, including PZT, PLZT, BZN, LMO, ZnO, BST, and others [58-62]. In most cases, the finest practical features can be found in ferroelectric thin films that were crystallized at high temperatures (about 700°C) [63, 64]. Because of this, it is essential that the outcomes of this laser-assisted technique be comparable. Laser annealing conditions for obtaining phase-pure perovskite PLZT thin films have been published by Bharadwaj et al.[65]. The annealing conditions are 250°C and above substrate temperatures, 10Hz laser-shot frequency, 10-200 mTorr oxygen partial pressure and a 100mJ laser energy. Without any secondary phase development being seen, polycrystalline perovskite films were produced. PLZT films crystallized using a laser have got dielectric constant and loss tangents of 406 and 0.027 respectively at 10 kHz, which are nearly identical to those of PLZT thin films that had undergone quick thermal annealing. These findings show that amorphous ferroelectric PLZT films can be crystallized using an excimer laser at relatively low temperatures. On a silicon substrate coated with LaNiO₃, Bharadwaj et al. used RF-magnetron sputtering to deposit PLZT thin films.

The kinetics of laser-annealing in thin films were investigated in this particular work for substrate temperatures that were lower than 400°C. The crystallization procedure was carried out with the assistance of a KrF Excimer laser that having a pulse duration of 20ns and at a laser fluence of 40mJ/cm². They came to the conclusion that a temporal exposure of 0.1 to 1.1 milliseconds was adequate to completely crystallize films that had a thickness of 380-400nm [66].

The kinematics of laser annealing is extensively studied by E. Huber et al. [67] by in-situ timeresolved spectroscopy of GeTe films. They found that there exists a critical laser fluence above which the onset of crystallization of thin films occurs, and the extent of crystallization is determined by the cooling rate near nucleation and growth regime. No crystalline material forms if the cooling rate during this temperature range is too high. If it is too low, complete crystallization takes place, and they found that, in laser annealing, the cooling rate at a constant temperature heavily depends on the laser fluence used. Table 2 summarises the most important investigation on laser annealing in functional oxide thin films. Laser annealing is not limited to these systems and extends to a wide variety of other classes of materials as well.

Sample	Deposition	Laser annealing	Substrate	Remark
	method	Temperature		
Pb(Zr _{0.52} Ti _{0.48})O ₃	Spin coating	370°C	Pt/Ti/SiO ₂ /Si	[68]
Ba _{0.6} Sr _{0.4} TiO ₃	RF Sputtering	300°C	Pt coated silicon	[72]
Ba _{0.5} Sr _{0.5} TiO ₃	PLD	300°C	Pt/Ti/SiO ₂ /Si	Device
				Fabricated[70]
Pb(Zr _{0.52} Ti _{0.48})O ₃	PLD	375°C	Pt/Ti/SiO ₂ /Si	[71]
Ba _{0.7} Sr _{0.3} TiO ₃	CSD	450°C	Pt-coated Si substrate	[69]
Ba _{0.8} Sr _{0.2} TiO ₃	PLD	600°C	glass and platinized substrates	Annealing in RT [73]
In ₂ O ₃ (9.9wt. %SnO ₂)	Electron beam evaporation	165°C	Si and glass substrates	[74]
Al-ZnO	RF Sputtering	500°C	Glass	[75]
Bi _{1.5} Zn _{0.5} Nb _{1.5} O _{6.5}	CSD	400°C	Pt/Ti/SiO2/Si	[76]

Table 1. 2 Laser annealing of various thin films in literature

1.6.5 Tunable Microwave Devices

Ferroelectric materials in their paraelectric phase find application in frequency agile devices because of their relatively high and electric field-dependent permittivity. The electric field dependence of permittivity allows the designers to select the operating frequency by small controlling voltage. This enables the manufacturers to use the same circuits with minimal modification to operate in a wide range of frequencies. Hence electric field tunability of ferroelectrics substantially reduces the efforts for device design, size and complexity and cost of a multiband device like a mobile phone. The electric field (applied DC electric field E) variation of permittivity (E) in the dielectric thin film is quantified by a parameter called tunability (n).

Tunability (n) =
$$\frac{\varepsilon(0)}{\varepsilon(E)}$$
 (1.4)

Where $\mathcal{E}(0)$ represents the permittivity at zero DC bias field and $\mathcal{E}(E)$ is the measured permittivity at bias field E. In general, the permittivity at zero bias field is higher and the value of tunability is always greater than one. In order to make the comparison easier, another parameter often used is the relative dielectric tunability (n_F)

$$n_r = \frac{\mathcal{E}(0) - \mathcal{E}(\mathcal{E})}{\mathcal{E}(0)} \times 100 \tag{1.5}$$

Among all the ferroelectric materials, $Ba_xSr_{1-x}TiO_3$ (BST) is the most widely investigated for tunable devices and BST-based circuits and devices are already demonstrated. Currently, this study has been extended to other ferroelectric and non-ferroelectric materials systems also [77-79].

1.7 Motivation

Ferroelectric thin films are utilized for the development of sensors, transducers, filters, MEMS, and various microwave devices. Currently, lead-based perovskite materials are extensively used for these applications because of their superior dielectric, piezoelectric and ferroelectric properties. Despite its superior ferroelectric characteristics, the toxic nature of Pb is a serious threat to both humans and the environment and it should be replaced. This necessitates the development of lead-free materials with superior dielectric and ferroelectric properties. Sodium bismuth titanate (NBT) is a suitable replacement for this purpose. Other major issues in the futuristic application of these films are their high crystallization temperature which is incompatible with present-day semiconductor processing and futuristic technologies being developed with polymers. The physics of laser crystallization is extensively studied in semiconductors, but their mechanism in ferroelectric materials is not comprehensively investigated. This thesis investigates various methods for lowering the crystallization temperature of NBT thin films, especially with laser annealing. This thesis is a small effort to understand the influence of various laser and material parameters in the low-temperature crystallization of NBT films.

1.8 Objective of Thesis

The major challenges to utilizing ferroelectric materials for next-generation flexible electronic devices are high crystallization temperature and the presence of lead (Pb) in those films. This thesis investigates the low-temperature crystallization of NBT thin films and explores their potential in high-frequency tunable devices.

The objectives of this thesis work are:

- ✓ Synthesis of single phase NBT ceramic target for thin film deposition by solid state reaction method. Calcination and sintering temperatures and excess bismuth amount to compensate the loss during the synthesis process need to be optimised.
- ✓ Investigate the role of substrate temperature on optical and electrical characteristics of NBT thin films synthesised by PLD method.
- ✓ Optimize the material deposition parameters and laser parameters to obtain goodquality NBT thin films.
- ✓ Examine the effectiveness of microwave annealing in reducing the crystallization temperature.
- ✓ The laser annealing of NBT thin films and the investigation of the effect of laser parameters on the laser annealing process.
- ✓ Investigate the role of deposition parameters and other material processing parameters on crystallization in the laser-annealing process for thin films.

1.9 Thesis outline

The present thesis is organized as follows

Chapter 1: Introduction

An introduction to the phenomenon of ferroelectricity and perovskite materials is presented. The necessity of high-temperature lead-free piezoelectrics is discussed. The rationale for selecting the lead-free NBT, a quick summary, and a literature review about NBT are presented. The next section gives an overview of the laser annealing process and a concise review of the laser annealing carried out in various ferroelectric materials. Finally, the motivation for the work and outline of the thesis is presented.

Chapter 2: Materials and Measurement Methods

This chapter introduces the material synthesis methods used for the preparation of bulk and thin films. In addition, the equipment used for synthesizing and characterizing the deposited films is briefly discussed. The synthesis procedure used to prepare NBT ceramics targets for thin film deposition by conventional solid-state reaction method is discussed in detail. The measurement methods employed for determining low and high-frequency dielectric properties for thin films and their data extraction methods are also presented.

Chapter 3: Effect of Substrate Temperature on In-Situ Crystallized Na_{0.5}Bi_{0.5}TiO₃ Thin Films

In this chapter, we looked at the role of substrate temperature in determining the structural, optical, and microwave dielectric properties of NBT thin films deposited by the pulsed laser deposition method on fused silica substrates. The NBT thin films deposited at low substrate temperatures are found to be amorphous. Amorphous and crystalline films' optical characteristics clearly differ from one another, which arises from the coordination defects and

short-range order in the amorphous material. The merging of the B and C bands in Raman spectra of amorphous NBT make it remarkably look different from the crystalline phase.

Chapter 4: Dielectric, Ferroelectric and Tunable Microwave Dielectric Properties of Na_{0.5}Bi_{0.5}TiO₃ Thin Films

Chapter 4 discusses the low and high-frequency dielectric characteristics of NBT thin films deposited on fused silica substrates. Inter Digitated Capacitor (IDC) test structures are fabricated on these films by photolithography. The dielectric tunability of these films at high frequency is measured using an on-wafer probing technique and vector network analyzer. The last part of this chapter discusses the ferroelectric properties of the NBT thin films deposited on identical conditions on a Pt-coated sapphire substrate.

Chapter 5: Effect of Microwave Annealing and Laser Fluence on Na_{0.5}Bi_{0.5}TiO₃ Thin Films

Chapter 5 discusses the role of annealing temperature during the microwave annealing of amorphous NBT thin films deposited by pulsed laser deposition. The morphological and microwave dielectric properties of the conventional and microwave-annealed films were compared. In the subsequent section of this chapter, an effort was made to decipher the role of laser fluence on the structural, microstructural and optical characteristics of NBT thin films.

Chapter 6: Laser-Induced Crystallization of Na_{0.5}Bi_{0.5}TiO₃ Thin Films

This chapter discusses the laser-induced crystallization of amorphous NBT thin films deposited at 300°C and laser annealed at room temperature. The effect of both laser and material/deposition parameters are varied to obtain room temperature crystallization of NBT thin films. The number of laser pulses and their energy density is the varied laser parameters. The deposition pressure during the amorphous phase formation substantially influences the extent of crystallization of NBT thin films during the annealing phase. The dependence of laser annealing on laser fluence during the deposition of the film is also discussed. The broadband

microwave frequency dielectric characteristics of optimized laser-annealed NBT thin films are measured and compared with conventional in situ crystallized films.

Chapter 7: Conclusions and future work

The major conclusions from the thesis work carried out are presented here. The potential future expansion of this work and possibilities are also discussed. Deposition of NBT thin films on polymer substrates and fabrication of devices is also a challenging task to tackle to realize flexible and tunable microwave devices.

1.10 Reference

- [1] M.E. Lines, A.M. Glass, *Principles and Applications of Ferroelectrics and Related Material*, Oxford University Press (1977).
- [2] B. Jaffe, H. Jaffe and W.R Cook, *piezoelectric ceramics*, Academic Press, London (1971).
- [3] Y. Xu, Ferroelectric Materials and Their Applications. Elsevier Science Publishers, Amsterdam, Netherlands (1991).
- [4] J.F. Scott, Ferroelectric Memories, Springer-Verlag, Berlin (2000).
- [5] S. Takagi, A. Subedi, V. R. Cooper, and D. J. Singh, Phys. Rev. B Condens. Matter Mater. Phys. **82**, 19 (2010).
- [6] A. Julio, Gonzalo and Basilio Jimknez (Ed.) Ferroelectricity: The Fundamentals Collection, WILEY-VCH Verlag CmbH & Co. KCaA (2005).
- [7] S. G. Kim, S. Priya, and I. Kanno, MRS Bull. 37, 1039 (2012).
- [8] Ashim Kumar Bain, Prem Chand, Ferroelectrics: Principles and Applications, WileyVCH Verlag GmbH& Co (2017).
- [9] L. Luo, B. Wang, X. Jiang, and W. Li, J. Mater. Sci. 49, 1659 (2014).
- [10] W. R. C. and J. M. H. B. Jafe, *Piezoelectric Ceramics* (Academic Press London and New York, 1971).
- [11] G. H. Haertling, J. Am. Ceram. Soc. **82**, 797 (1999).
- [12] A. J. Moulson and J. M. Herbert, *Electroceramics: Materials, Properties, Applications* (Wiley, 2003).
- [13] Y. Moritomo, A. Asamitsu, H. Kuwahara, and Y. Tokura, Nature 380, 141 (1996).
- [14] H. Fu and R. E. Cohen, Nature 403, 281 (2000).
- [15] S. Kanno, Y. Imamura, and M. Hada, Phys. Rev. Mater. 3, 75403 (2019).
- [16] G. Sághi-Szabó, R. E. Cohen, and H. Krakauer, Phys. Rev. Lett. **80**, 4321 (1998).

- [17] J. P. Attfield, P. Lightfoot, and R. E. Morris, Dalt. Trans. 44, 10541 (2015).
- [18] V. M. Goldschmidt, Naturwissenschaften 14, 477 (1926).
- [19] Shrout, T.R., Zhang, S.J. Lead-free piezoelectric ceramics: Alternatives for PZT J Electroceram **19**, 113–126 (2007).
- [20] David J. Elliott, Chapter 7 Annealing and Planarizing, Editor(s): David J. Elliott, Ultraviolet Laser Technology and Applications, Academic Press, Pages 209-250 (1995)
- [21] Palneedi, H., Park, J. H., Maurya, D., Peddigari, M., Hwang, G.-T., Annapureddy, V., Kim, J.-W., Choi, J.-J., Hahn, B.-D., Priya, S., Lee, K. J., Ryu, J., Adv. Mater, **30**, 1705148 (2018).
- [22] G. A. Smolenskii, V. A. Isupov, A. I. Agranovskaya, and N. N. Krainik, Fiz. Tverd. Tela Sanktpeterbg. **2**, 2982 (1960).
- [23] P. Baettig, C. F. Schelle, R. LeSar, U. V. Waghmare, and N. A. Spaldin, Chem. Mater. **17**, 1376 (2005).
- [24] N. A. Hill and K. M. Rabe, Phys. Rev. B **59**, 8759 (1999).
- [25] J. Rödel, K. G. Webber, R. Dittmer, W. Jo, M. Kimura, and D. Damjanovic, J. Eur. Ceram. Soc. **35**, 1659 (2015).
- [26] K. N. N. Smolenskii G.A., Isupov V.A., Agranovskaya A.I., Sov. Phys. Solid State2, 2651 (1961).
- [27] E. Aksel, J. S. Forrester, J. C. Nino, K. Page, D. P. Shoemaker, and J. L. Jones, Phys. Rev. B Condens. Matter Mater. Phys. 87, 1 (2013).
- [28] T. Yu, K. W. Kwok, and H. L. W. Chan, Thin Solid Films **515**, 3563 (2007).
- [29] Y. Kitanaka, H. Matsuo, Y. Noguchi, and M. Miyayama, J. Asian Ceram. Soc. 3, 160 (2015).
- [30] M. Peddigari, H. Palneedi, G. T. Hwang, and J. Ryu, J. Korean Ceram. Soc. **56**, 1 (2019).

- [31] J. Song, J. Gao, S. Zhang, L. Luo, X. Dai, L. Zhao and B. Liu, Crystals 9,558 (2019).
- [32] X.-G. Tang, J. Wang, X.-X. Wang, and H. L.-W. Chan, Chem. Mater. **16**, 5293 (2004).
- [33] Z. H. Zhou, J. M. Xue, W. Z. Li, J. Wang, H. Zhu, and J. M. Miao, Appl. Phys. Lett. 85, 804 (2004).
- [34] Z. Cao, A. L. Ding, X. He, W. Cheng, and P. Qiu, J. Cryst. Growth **270**, 168 (2004).
- [35] A. S. Daryapurkar, J. T. Kolte, and P. Gopalan, Thin Solid Films 579, 44 (2015).
- [36] J.-R. Duclère, C. Cibert, A. Boulle, V. Dorcet, P. Marchet, C. Champeaux, A.

Catherinot, S. Députier, and M. Guilloux-Viry, Thin Solid Films 517, 592 (2008).

- [37] S. Pattipaka, A. Joseph, G. P. Bharti, K. C. J. Raju, A. Khare, and D. Pamu, Appl. Surf. Sci. 488, 391 (2019).
- [38] Hiroshi Maiwa, Tomonori Kogure, Wataru Sakamoto & Takashi Hayashi, Ferroelectrics, 405:1, 204-210 (2010).
- [39] K. Miriyala, R. Ramadurai, Ceram. Int. 44, 14556–14562 (2018).
- [40] Daryapurkar, A. S., J. T. Kolte, P. R. Apte, and P. Gopalan. Ceram. Int., **40**, 2441–2450 (2014).
- [41] Daryapurkar, A.S, J.T Kolte, P. Gopalan, Thin Solid Films, **579**, 44–49 (2015).
- [42] Y. Hiruma, Y. Imai, Y. Watanabe, H. Nagata, T. Takenaka, Appl. Phys. Lett. **92**, 262904 (2008).
- [43] Y. Hiruma, H. Nagata, T. Takenaka, J. Appl. Phys., **104**, 124106 (2008).
- [44] Zhen Fu, Ranqing Zhu, Di Wu, Aidong Li, J Sol-Gel Sci Technol 49:29–34 (2009).
- [45] L. Huitema, M. Cernea, A. Crunteanu, L. Trupina, L. Nedelcu, M.G. Banciu, A.
- Ghalem, M. Rammal, V. Madrangeas, Passerieux, D., *J. Appl. Phys.*, *119*, 144103 (2016).

- [46] Fang Wang, Cong Zhu, Shifeng Zhao, Journal of Alloys and Compounds, 869, 159366 (2021).
- [47] P. Lv, S.F. Huang, X. Cheng, C.H. Yang, Q. Yao, Ceramics International, 44,13, 15236-15242 (2018).
- [48] Yun C, Webb M, Li W, Wu R, Xiao M, Hellenbrand M, et al. *J Mater Chem C.* **9**(13): 4522–31 (2021).
- [49] Fabien Rémondière, Barbara Malič, Marija Kosec, Jean-Pierre Mercurio, Journal of the European Ceramic Society, **27**,13–15 (2007).
- [50] Stephania Kossman, Arthur Hamieh, Freddy Ponchel, Denis Rémiens, Maxence Bigerelle, Thin Solid Films, 759, 139459 (2022).
- [51] Changhong Yang, Huiting Sui, Haitao Wu, Guangda Hu, Journal of Alloys and Compounds, **637**, 315-320 (2015).
- [52] Pattipaka, S., Dobbidi, P., Pundareekam Goud, J. et al. J Mater Sci: Mater Electron 33, 8893–8905 (2022).
- [53] C. Feng, C.H. Yang, H.T. Sui, F.J. Geng, Y.J. Han, Ceramics International, 41, 3, Part A (2015).
- [54] J. M. Poate and J. W. Mayer, Laser Annealing of Semiconductors. Academic Press, (1982).
- [55] I. Bretos, R. Jiménez, J. Ricote and M. L. Calzada, *Chem. Soc. Rev.* 47, 291 (2018).[56] James S. Im, H. J. Kim, and Michael O. Thompson, Appl. Phys. Lett. 63, 1969 (1993).
- [57] P Arun, A G Vedeshwar and N C Mehra, J. Phys. D: Appl. Phys. **32**, 183 (1999).
- [58] S. Halder, U. Boettger, T. Schneller, R. Waser, O. Baldus, P. Jacobs, M. Wehner, Mater. Sci. Eng. B, 133, 235–240 (2006).

- [59] A. Queralto, A. Perez Del Pino, M. De La Mata, J. Arbil, M. Tristany, A. Gomez, X. Obradors and T. Puig, Appl. Phys. Lett., **106**, 262903 (2015).
- [60] M.G. Kang, K.H. Cho, Y.H. Do, Y.J. Lee, S. Nahm, S.J. Yoon and C.Y.Kang, Appl.Phys. Lett., 101, 242910 (2012).
- [61] J. G. Cheng, J. Wang, T. Dechakupt and S.T. McKinstry, Appl. Phys. Lett., 87, 232905 (2005).
- [62] T. Nakajima, T. Tsuchiya, M. Ichihara, H. Nagai and T. Kumagai, Appl. Phys. Express, 2,023001 (2009).
- [63] K. Kim and S. Lee, J. App. Phys. **100**, 051604 (2006).
- [64] P. Muralt, Integr. Ferroelctr. 17, 297-307 (1997).
- [65] S. Bharadwaja, J. Kulik, R. Akarapu, H. Beratan and S.T. McKinstry, IEEE Trans. Ultrason. Ferrolelect. Freq. Control, **57**, 2182-2191 (2010).
- [66] SSN Bharadwaj, T. Dechakupt and S.T. McKinstry, H. Beratan, *J. Am. Ceram.Soc.*91, 1580–1585 (2008).
- [67] Huber, E., Marinero, E.E. MRS Online Proceedings Library 74, 257 (1986).
- [68] A. Rajashekhar, S. S. N. Bharadwaja, and Susan Trolier-McKinstry, Applied Physics Letters **103**, 032908 (2013).
- [69] S. S. N. Bharadwaja, F. Griggio, J. Kulik, and S. Trolier-McKinstry, Appl. Phys. Lett. **99**, 042903 (2011).
- [70] J.P. Goud, A. Kumar, K. Sandeep, S. Ramakanth, P. Ghoshal, K.C.J. Raju, Adv. Electron. Mater, **7**, 3 (2021).
- [71] M.G. Kang, K.H. Cho, Y.H. Do, Y.J. Lee, S. Nahm, S.J. Yoon and C.Y.Kang, Appl.Phys. Lett., 101, 242910 (2012).
- [72] M.G. Kang, K.H. Cho, Y.H. Do, Y.J. Lee, S. Nahm, S.J. Yoon and C.Y.Kang, Appl.Phys. Lett., 101, 242910 (2012).

- [73] J. P. B. Silva, A. Khodorov, A. Almeida, J. Agostinho Moreira, M. Pereira, M. J. M. Gomes, Appl. Phys. A 116, 1271–1280 (2014).
- [74] D.C. Paine, T. Whitson, D. Janiac, et al., J. Appl. Phys., **85** (12), 8445-8450 (1999).
- [75] iang Xu, R.D Hong, H.L Huang, Z.F Zhang, M.K Zhang, X.P Chen, Zh.Y Wu, Optics & Laser Technology, **45**, 513-517 (2013).
- [76] Jian-Gong Cheng, Junling Wang, Tanawadee Dechakupt, and Susan Trolier-McKinstry, Appl. Phys. Lett. **87**, 232905 (2005).
- [77] Lee, Y.C. & Hong, Y.P. & Kim, D.M. & Ko, K.H., Electronics Letters. **42**. 851 853 (2006).
- [78] S.S. Gevorgian, E.L. Kollberg, IEEE Transactions on microwave theory and techniques, **49**, 11 (2001).
- [79] L. Huitema, M. Cernea, A. Crunteanu, L. Trupina, L. Nedelcu, M. G. Banciu, A. Ghalem, M. Rammal, V. Madrangeas, D. Passerieux, P. Dutheil, F. Dumas-Bouchiat, P. Marchet, and C. Champeaux, Journal of Applied Physics **119**, 144103 (2016).

Chapter 2 Experimental methods and characterizations tools

2.1 Introduction

This chapter describes the preparation of Na_{0.5}Bi_{0.5}TiO₃ (NBT) material in bulk and thin films. In addition, the equipment used for synthesizing and characterizing the deposited film are briefly discussed. The NBT ceramics are synthesized by the solid-state reaction method. Ceramic pellets made with these powders are used as the target for thin film depositions. Varactors were lithography made on these film surfaces to investigate low and high-frequency dielectric characteristics. Microwave dielectric characteristics of thin films were measured by various available techniques.

2.2 Target preparation Procedure

The solid-state reaction method (popularly known as shake 'n bake) is employed to synthesize the target materials for depositions of the thin films [1-5]. In this method, first Na_{0.5} Bi_{0.5}TiO₃ (NBT) powder is prepared from high-purity reactants such as NaCO₃, Bi₂O₃, and TiO₂.

$$Na_2CO_3 + 4TiO_2 + Bi_2O_3 \longrightarrow 4Na_{0.5}Bi_{0.5} TiO_3 + CO_2 (\uparrow)$$

The reagents are taken in appropriate proportion to obtain 20 gm of NBT in an electronic balance having 0.01mg resolution. These powders are mixed, and ball milled (Retsch PM 100) for 2 hours to bring the particles of reactants into contact. The mill Retsch PM 100 is shown in Fig. 2.1. Considering the volatile nature: an excess amount of Bi₂O₃ (2%) is added, and sealed containers are used in the heating cycles. The ball-milled powders are calcined at 900°C in an Enerzi microwave furnace with a dwell time of 20 minutes. The heating and cooling ramp rate are maintained at around 25°C/min. Then this powder is removed from the furnace and mixed with 1% PVA (binder) to prepare the PLD target. The target is prepared in a circular disc of radius 12 mm having a thickness more than 3 mm in a hydraulic press by excreting a pressure of 2 MPa. Then the pellet is sintered in a high-temperature furnace. Initially, the binder of the pellet is evaporated at 550°C with a moderate heating rate. The samples were sintered at 1150°C in the furnace for 180 minutes of dwell time. The sintered pellets have a crystalline phase with a rhombohedral structure which is confirmed by XRD. This well-sintered pellet of radius 12 mm and a density of more than 98% was utilized for the thin film deposition.

The various steps involved in target preparation are summarised in the block diagram (Fig 2.2)



Fig 2. 1: Ball Mill with Zirconia Jar loaded

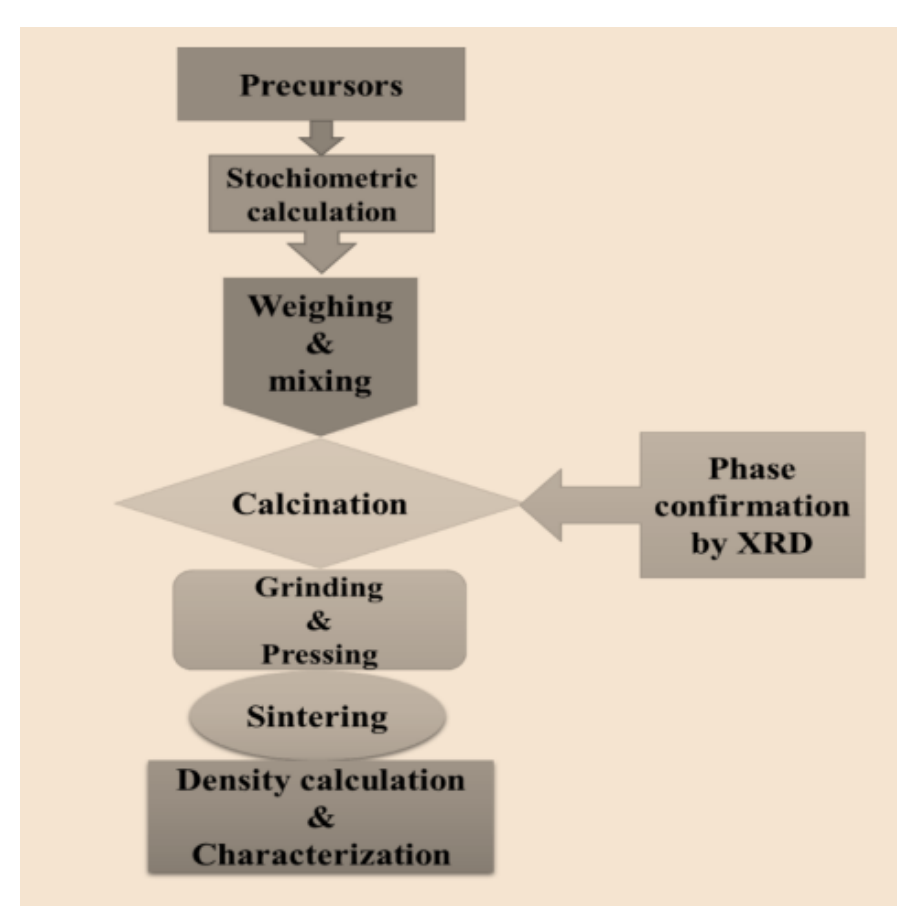


Fig 2. 2: Flow chart representation NBT Target preparation process

2.3 Pulsed Laser Deposition

Laser became an inevitable source of energy immediately after its invention and one of the application for it became ablation of solids in making thin films. The ease of variation and availability of numerous process control parameters such as laser wavelength, energy, pulse width etc., and localised process control provided supremacy for laser ablation of solids over other conventional tools/methods. Hence in a very short period of time laser based thin film deposition technology developed and was widely used for multi-component solid film deposition. Even though the physical process is simple, the theoretical description of the process is very complex. Pulsed laser deposition is a physical vapour deposition method in which a focused laser beam is incident on the surface of the dense target material, producing a plasma which is eventually condensed on to the surface of a substrate. The pulsed laser deposition process is generally classified into four stages:

- 1. Absorption of pulsed energy and electronic excitation and plasma generation
- 2. Plasma dynamics
- 3. Collection of ablated species at the substrate.
- 4. Nucleation and growth of target material.

The initial ablation may be photo-chemical as chemical bond dissociates, or photo-thermal leading to evaporation, determined by the wavelength of laser and electrical properties of the target. The laser is absorbed within a small volume of the target surface and the electron in this region is excited to higher energy, the excited electron colliding with the atoms in lattice and transferring energy, thereby vaporising the materials on the surface. In the later stage, the particles in the plasma also absorb energy from the laser beam producing an expansion in the forward direction. The plasma's shape and dynamics depend heavily on the background gas pressure.

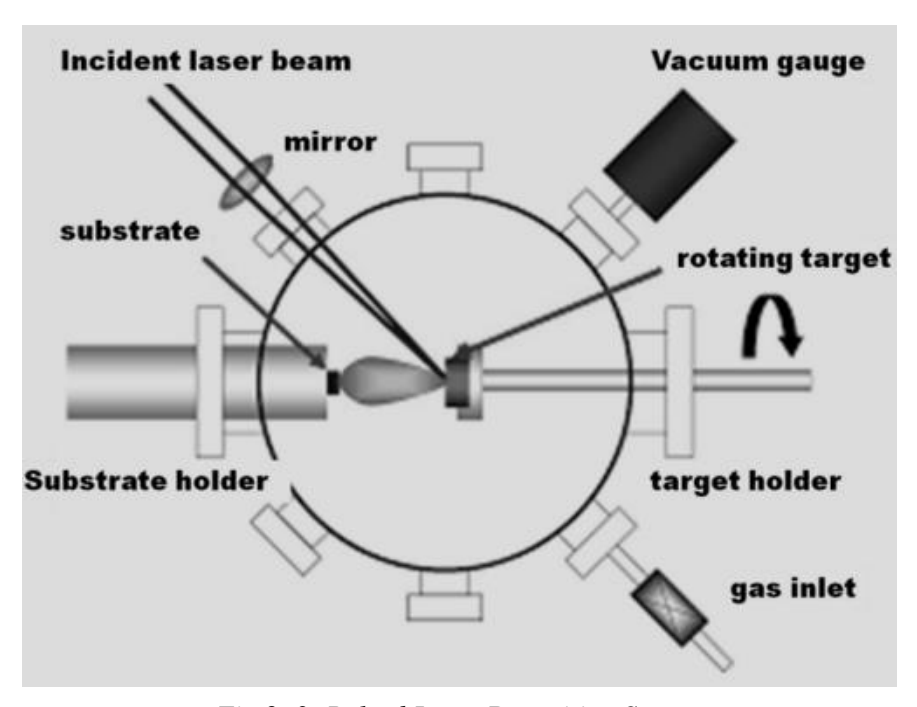


Fig 2. 3: Pulsed Laser Deposition System

The high kinetic energy (KE) of species and higher deposition rate owing to the short laser pulse width in PLD may damage the substrate during the collection of ablated material. The background gas reduces the KE of these species. The collision between the substrate and plasma reaches an equilibrium, and a thin layer of the target material is coated on the substrate in the later stage.

2.3.1 NBT deposition by PLD

NBT thin films utilized for this thesis work are mostly deposited on a fused silica substrate. The Coherent-Compex Pro 102 F with KrF Excimer laser producing 20 ns pulse of wavelength 248 nm is used as the laser source. The film is deposited at 2J/cm² fluence and 5 Hz repetition rate. The target and substrate for deposition are kept in a spherical chamber having a substrate heater facility supplied by Excel Instruments. The substrates are placed a fixed distance of 5 cm away from the target. The substrate is loaded into the chamber, and then the chamber is evacuated to the base vacuum using Turbo and backing pumps. Once the base vacuum is reached, the gate valve is closed and the substrate is brought to the required temperature using the heater. The working pressure is obtained by supplying high-purity oxygen gas. The ATCC program chooses the desired NBT target and the target is rotating at a fixed speed of 10 rpm. Post-deposition, the deposited films are post-annealed for 30 min in the oxygen atmosphere. The schematic of the PLD system is shown in Fig 2.3 and the details of deposition parameters are tabulated for easy reference in Table 2.1.

S.No	Parameter	Values	
1	Laser	Excimer laser (KrF)	
2	Wavelength	248 nm	
3	Base vacuum	5 x 10 ⁻⁶ mbar	
4	Target and substrate distance	5 cm	
5	Target rotation	10 rpm	
6	Repetition rate	5Hz	
7	Laser fluence	2 J/cm ²	
8	Temperature	300°C to 700°C	
9	Working pressure	0.2 mbar to 2x10 ⁻³ mbar	
10	Substrates	Fused silica, platinized silicon (111), sapphire, and platinum-coated sapphire	

Table 2. 1: NBT Thin film deposition conditions

2.3.2 Laser Annealing Setup

The Schematic diagram of the laser annealing setup that was used for the annealing of amorphous NBT thin films is depicted in Fig. 2.4. An excimer laser, mirrors, and an annealing chamber are the major components of the laser annealing setup.

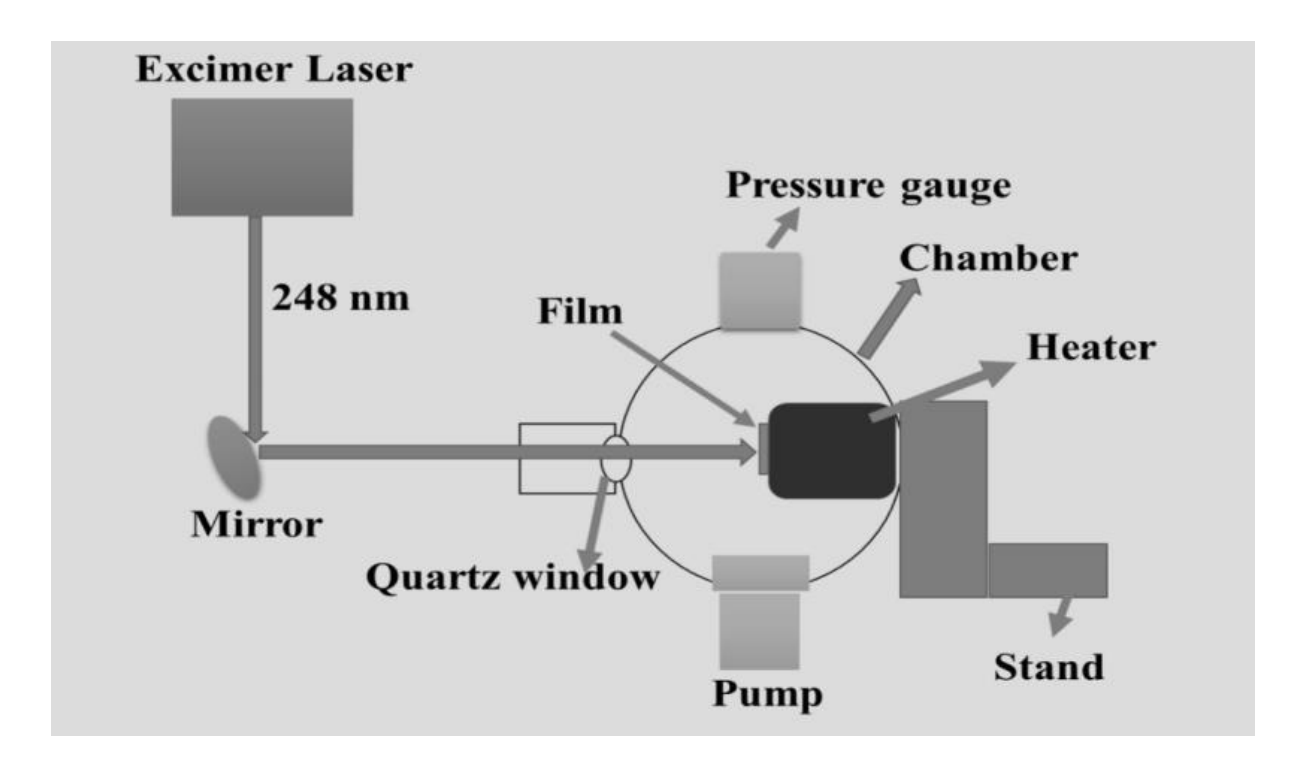


Fig 2. 4: Laser annealing instrumentation

2.4 Characterization Technique

2.4.1. X-ray Diffraction (XRD)

XRD is a non-destructive versatile tool used in many areas of science. The diffraction pattern provides information about the phase composition, phase purity, crystallographic texture, crystallite size, crystallite strain, etc. According to the well-known Bragg's law, X-ray diffraction may be treated similar to their reflection from a stack of atomic planes (Fig 2.5). In X-rays scattering spectra of a crystal lattice, peaks intensity is obtained when Bragg's law is satisfied [6-8]

$$n \lambda = 2d_{hkl}\sin\theta$$
 (2.1)

where d_{hkl} is the inter-planar spacing, θ represents the angle of the incidence, n is the order diffraction, and λ is the wavelength of the X-rays.

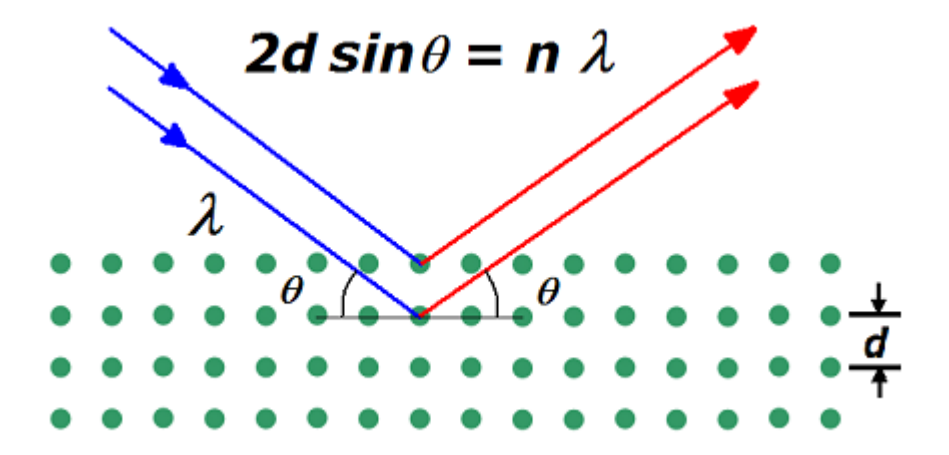


Fig 2. 5: Principles of X-ray Diffraction

The majority of the X-ray diffractometers utilize copper $K\alpha$ with a 1.5406Å wavelength. A metal target, often Copper, is allowed to be struck by a beam of accelerated electrons. These high-energy electrons knock off the electrons from the inner shell of the target atoms. X-ray photons are emitted when electrons from the outer shell move to the vacant inner shell and the difference in energy is released as photon.

Grazing angle Incidence-XRD

The X-ray diffraction geometry used for powder samples is inefficient for thin films. In normal XRD measurement, we get only feeble signals from film and most of the signal is from the substrate if it is crystalline because of the longer penetration depth of X-rays. This problem is surmounted in Grazing Incidence X-ray diffraction (GI-XRD) mode by directing the X-ray beam from a lower incident angle which allows the X-ray to travel more through the film than through the substrate. The incident angle used varies from 0.5-1°. GI-XRD-Bruker D8 (Fig 2.6) with a Cu-K alpha line of wavelength 1.5406 Å is used as part of this work to obtain the required thin film XRD Data.

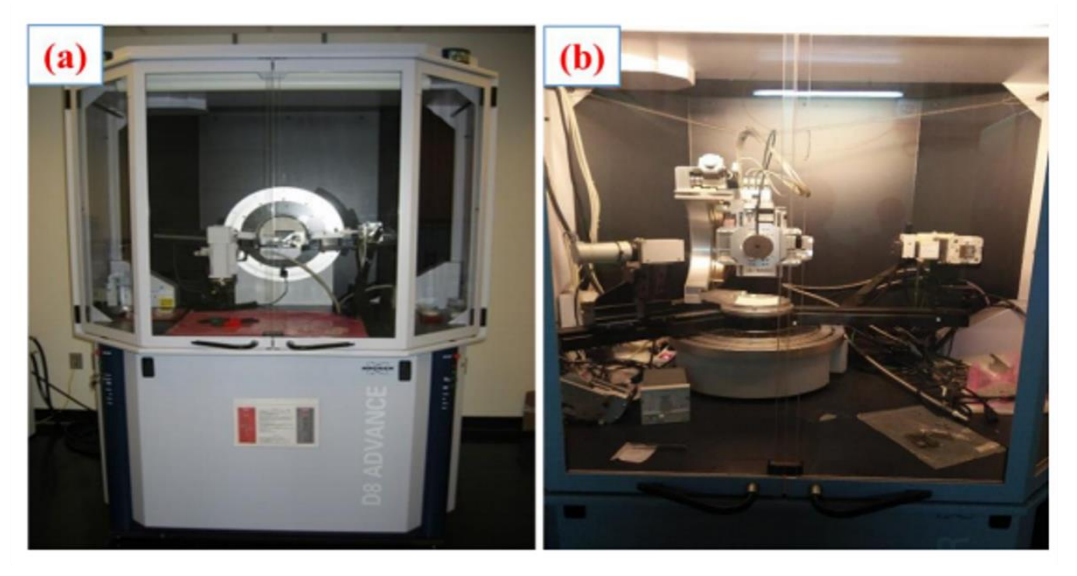


Fig 2. 6:a) Bruker D8 advanced diffractometer for bulk (b) Bruker D8 discovered for thin films (GIXRD).

2.4.2 Field Emission Scanning Electron Microscopy (FESEM)

FESEM is used to investigate the surface morphology, grain size and other morphological features of submicron materials. The electrons emitted from the electron gun with shorter wavelength are focused to a small spot, 50-500 Å in diameter, on the sample. The resolution of FESEM is superior to optical microscopes, because of the short de-Broglie wavelength of accelerated electrons $\lambda = \frac{h}{\sqrt{2m_0eV}}$, where h is Planck's constant, m_0 is the rest mass of

electrons, and e is the charge of an electron. For example, when the potential varies from 1keV to 30keV, the corresponding de-Broglie wavelength changes from 38pm to 7pm. [9,10]

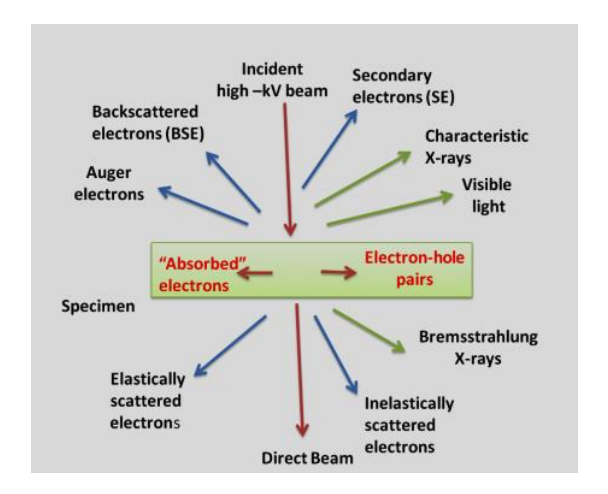


Fig 2.7:Electron matter interaction [11]

Electron matter interaction is depicted in Fig. 2.7. Unlike TEM, Secondary Electrons, Back Scattered Electrons, and characteristic X-rays are used for SEM images and elemental analysis.

Carl Zeiss Ultra 55 FE-SEM is used to collect the morphological images of both the bulk as well as the thin films deposited as part of this work. A diagrammatic representation of FE-SEM is portrayed in Fig 2.8.

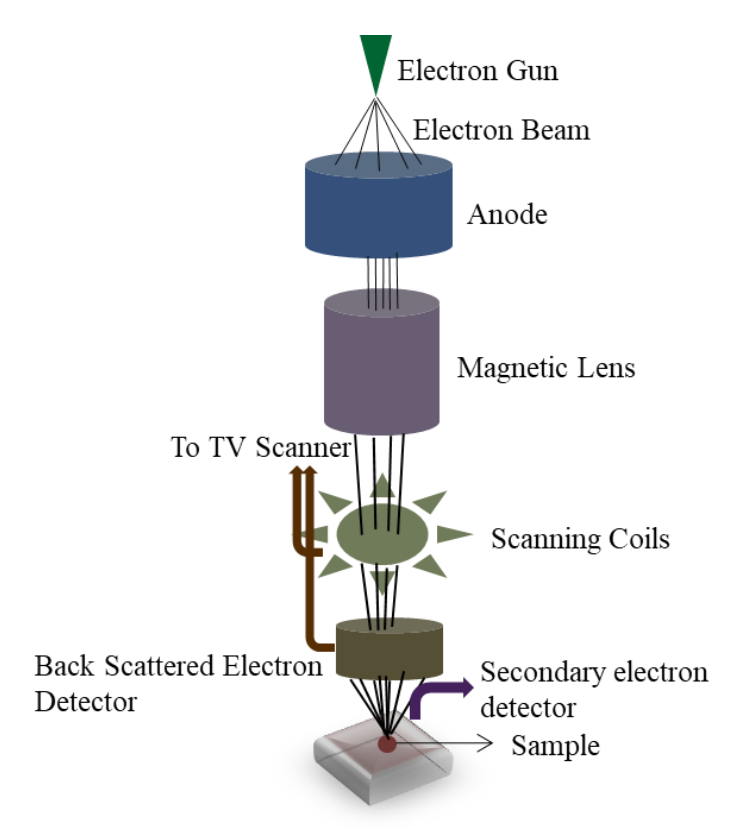


Fig 2. 8: Block Diagram of FESEM instrumentation [12]

Energy dispersive spectroscopy (EDS) helps us identify the sample's elemental composition. Compared to the counterpart wavelength dispersion spectroscopy (WDS), the EDS is faster and instrumentation is simpler and hence economical. In EDS, the characteristic X-rays emitted from the target sample when it is irradiated by an electron beam, the energy of the emitted X-ray is electronically resolved (Fig 2.9). The characteristic X-ray energy, according to Moseley's law

$$F = A (Z-B)^2$$
 (2.2)

where Z is the atomic number, and A and B are constants.

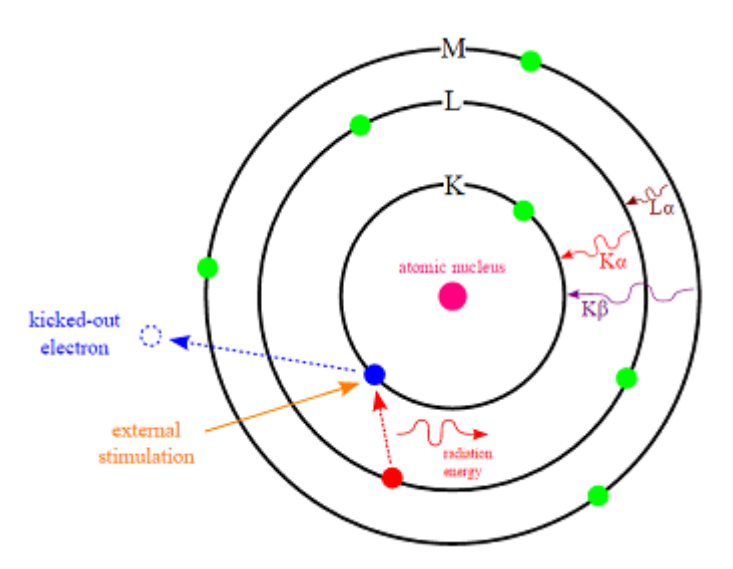


Fig 2.9: Principle of Energy Dispersion Spectroscopy [13]

2.4.3 UV- visible NIR spectroscopy

Optical spectroscopy is employed in the diverse field of science and technology for characterizing the bulk and thin film samples. The transmission, Reflectance and Absorption modes are available in a JASCO V-570 UV-VIS-NIR spectrophotometer. In the present study, we mostly measured the transmittance of NBT and other films and calculated all other optical parameters from the transmission spectra. Our measurement instrument (JASCO V-570) (Fig 2.10) has dual sources, namely, a deuterium (D₂) lamp and a Tungsten halogen lamp (W Lamp). The UV range is covered by the D₂ lamp, whereas the halogen lamp covers visible and NIR ranges. It operates in a frequency range of 190nm UV and reaches up to 2700 nm NIR range. The monochromator has two gratings, one for the UV/Visible region with 1200 grooves/mm and the other for Near-IR with 300 grooves/mm. It has dual detectors, a PMT detector for the UV/Visible range and a PbS detector for the Near-IR range.

Many oscillations in transmittance are observed in optical spectra as a result of interference at the film-substrate and air-film interfaces. A quartz substrate is preferred due to its capability to withstand very high temperatures along with very high optical transmittance (non-metallic nature) and large band gap (>6 eV). We observed sharp absorption edges and the presence of well-defined loops in synthesized films. In case films have a high degree of non-uniformity in the thickness, all the interference loops will disappear, and we will get a smooth transmission curve [13-16]. The optical band gap is determined by Tauc's relation.

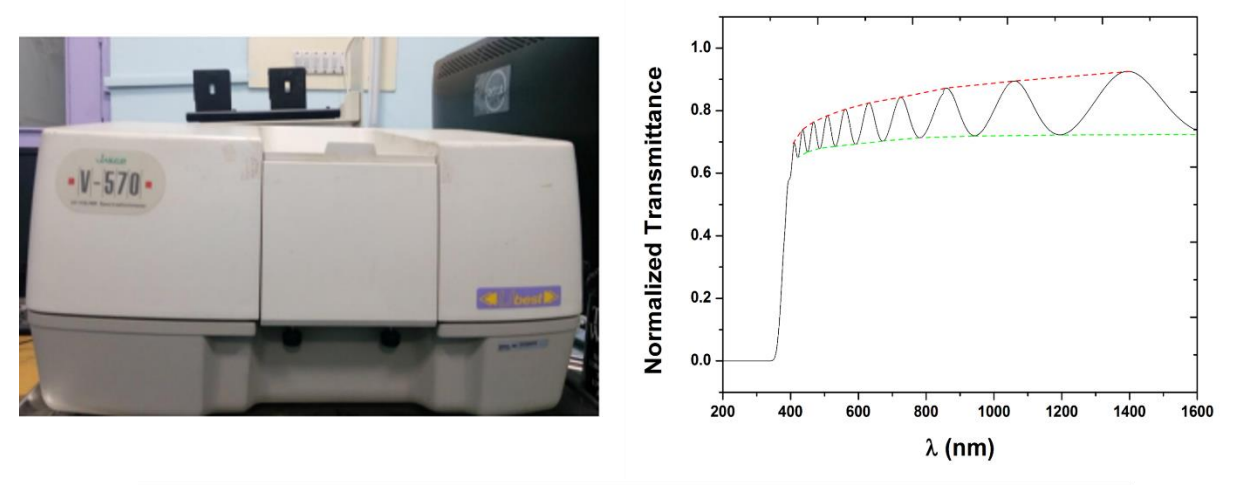


Fig 2. 10:(a) UV-VIS-NIR spectrophotometer (b) Transmission spectra of NBT thin film deposited on fused silica

2.4.4 Profilometer

The thickness of the NBT thin film is measured using a stylus profilometer. It is a simple and quick, non-destructive technique used to measure film thickness. The profilometer works in contact mode. When the tip of the profilometer reaches the step or groove on the film surface between the substrate and the thin film, the upward or downward displacement of stylus move across the step provide the film's thickness. A proper step can be obtained by masking the substrate during deposition. XP-200, Ambios Technology is employed in the current study to measure the thickness of all the deposited films (Fig 2.11).

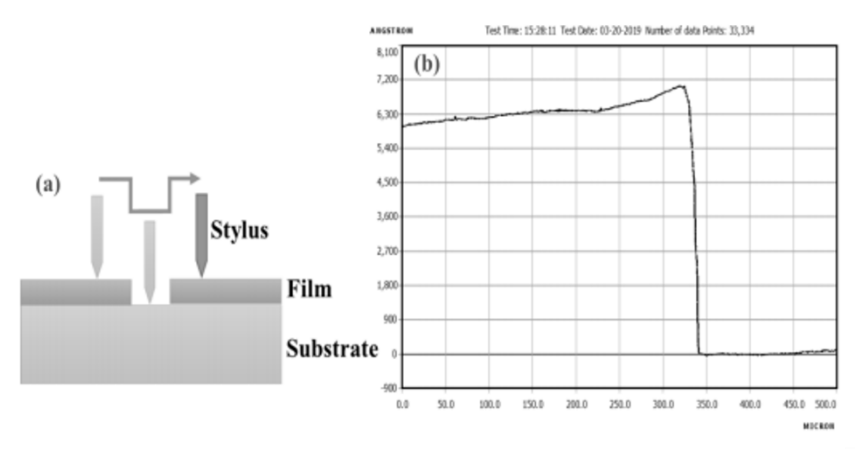


Fig 2. 11:(a)Illustration of stylus profilometer-based film thickness measurement (b)Thickness measurement result for NBT thin films

2.4.5 Raman Spectroscopy

This technique is based on the inelastic scattering of a photon by phonon and is hence useful to investigate the dispersion curves of solids. Here we used Raman spectroscopy to characterize our sample because of its ability to distinguish the amorphous and crystalline phases of NBT. The basic theory of Raman spectroscopy can be found in any standard molecular spectroscopy

textbook [17-19]. Only very few essential points are reviewed here.

When the sample is irradiated with monochromatic light (often laser), both elastic and inelastic scattering occurs. In elastic scattering, the frequency of scattered radiation does not change (Rayleigh scattering), but in inelastic scattering energy of the scattered photon either increases (anti-stoke lines) or decrease (stoke lines) energy which is known as Raman scattering. The change in frequency from the excitation frequency is measured and is called the Raman shift.

The Raman spectra of all samples were measured in backscattering geometry with an Nd-YAG laser at an excitation wavelength of 532 nm using an Alpha 300 Witec spectrometer. Raman spectra are recorded at 200 to 1200 cm⁻¹ with a spectral resolution of 3 cm⁻¹ (Fig 2.12).

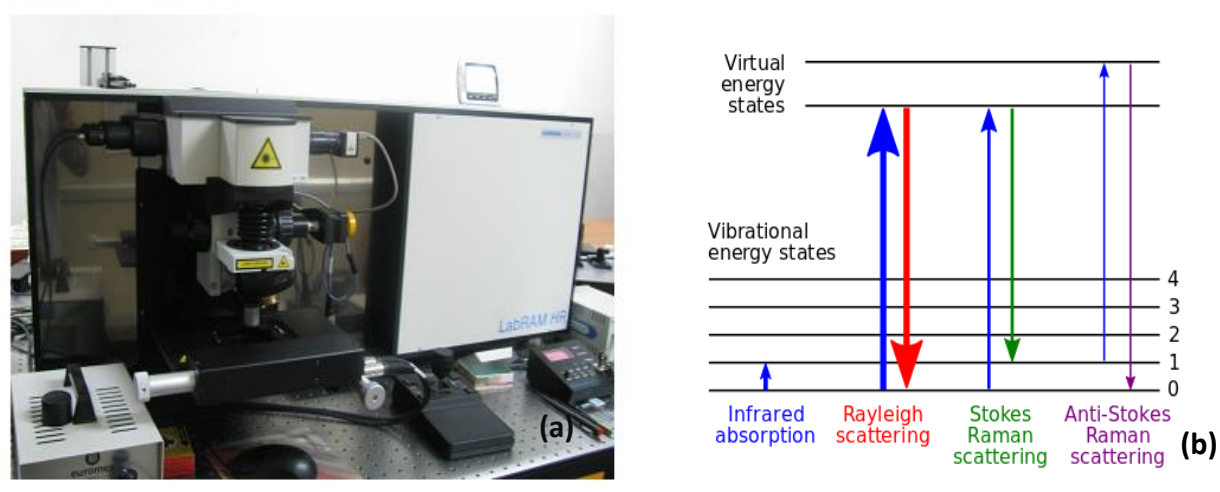


Fig 2.12(a):HR 800 Horiba Jobin Yvon confocal micro-Raman spectrometer. (b) diagrammatic representation of the Raman process

2.4.6 Dielectric spectroscopy

2.4.6.1 Low-frequency dielectric constant of bulk materials

The low-frequency dielectric measurement is evolved as crucial material characterization method. The ability of polarizability of material in an electric field is represented by its dielectric permittivity (ϵ '), and the dielectric loss measures the dissipation of energy. The complex dielectric permittivity of the material is represented by a complex quantity as

$$\varepsilon^* = \varepsilon' + i \varepsilon''$$

The temperature and frequency dependence of dielectric properties such as capacitance and dielectric loss are measured with Novocontrol Alpha –A measurement system. The experimental setup is shown in Fig. 2.13. The system measures dielectric, conductivity, and impedance spectroscopy. For the measurement, additional test interfaces are required. The

system works for frequencies ranging from 3 μ Hz to 40 MHz in the temperature range from ambient to 1200°C. For measurement purposes, two types of sample holders are used in the present study. Room temperature measurement is conducted by BDS 1200; for high-temperature measurement, Novotherm-HT 1200 is used. The images of sample holders are shown in Fig. 2.14. The complete description of the holders and working principles can be found in ref. [20].



Fig 2. 13: Dielectric measurement set up with furnace

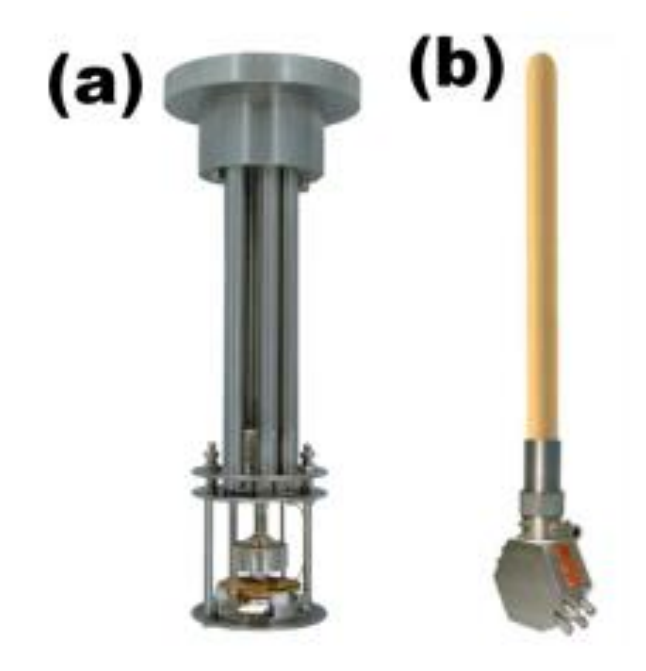


Fig 2. 14: Images of (a) BDS 1200 and (b) Novotherm-HT 1200.

2.4.6.2 Dielectric spectroscopy of Thin films: Interdigitated capacitor

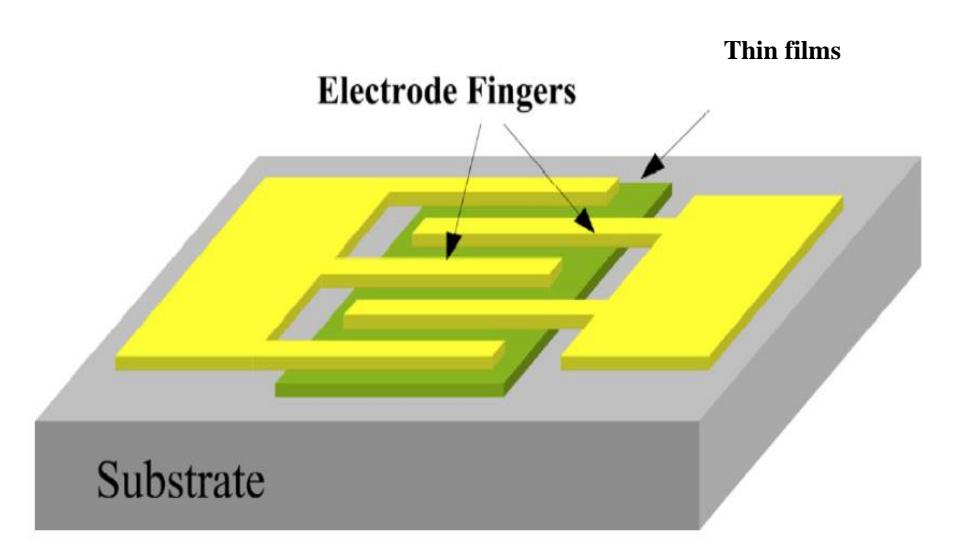


Fig 2.15: Block diagram of interdigitated capacitor

The NBT thin films grown on fused silica and sapphire substrates did not have a metallic bottom layer. In those cases, their dielectric response were measured using an interdigitated capacitor (IDC) method. A schematic of IDC is shown in Fig 2.15. The IDC capacitors with following dimensions are used to determine their dielectric characteristics. Finger length $90\mu m$, finger width and finger gap of $10\mu m$, number of fingers 8 and an overlap length of $80\mu m$. These capacitors were fabricated on the films surface using the gold as the electrode material,

using photolithography. The setups involved in photolithography are depicted in the following Figure 2.16.

• Clean the Substrate Substrate • Deposit ~400 nm of NBT thinfilm using PLD **NBT** deposition • Spin coat the surface with Photo Resist (PR) • Pattern the layout on the surface **Patterning** • Develop the PR using tetra methyl ammonium hydroxide • Using RF sputtering deposit Cr(20 nm) and then Au(200 nm) on it Metal Deposition • Use acetone to lift off the metal deposited on PR Lift Off • Use VNA, dc bias and coplanar probes to obtain the sparameters Testing

Fig 2.16: Block diagrams of stages in photolithography

2.4.7 Vector Network Analyser(VNA): High-frequency Measurement

VNA is utilized to measure the S parameters of components, devices or circuits. They display ratios of power amplitudes and phases. In order to measure them accurately, a VNA uses four major components.

- 1. Source for stimulus (Integrated synthesised sources)
- 2. Signal separation device (Directional coupler and bridge)
- 3. Signal detector block (tuned Receiver down-convert and detect signal)
- 4. Processor and display for calculating and displaying the result.

Many VNA-based measurements are performed as a part of this thesis, and they are individually described in the relevant sections. Only a general overview is presented here [21,22]. Network analyzer measurements have three major sources of errors: systematic, random, and drift. Systematic errors can be corrected using vector error correction, also known as the calibration of VNA. Different calibration methods are available depending on the types of measurement, frequency interval, and type of DUT. SOLT (Short, Open, Load, Thru) and TRL (Thru, Reflect, Line) are commonly used calibration standards for on-wafer measurements. The short standard completely reflects the incident signal ($|\Gamma|=1$) and causes a 180° phase shift in the incident signal. The open standard also has $|\Gamma|=1$ but with a 0° phase shift. The load consists of a 50 Ohm termination and, ideally, produces no reflections ($\Gamma=0$). The Thru is a 50 Ohm line that connects the two ports. The length of thru should be as small as possible to minimize the parasitic shunt capacitance. Also, De-embedding should be done since the reference plane (where S parameters are measured) will be shifted to the centre of thru due to calibration. The on-wafer calibration standards and photograph of the VNA used high frequency measurement is shown in Fig 2.17.

.

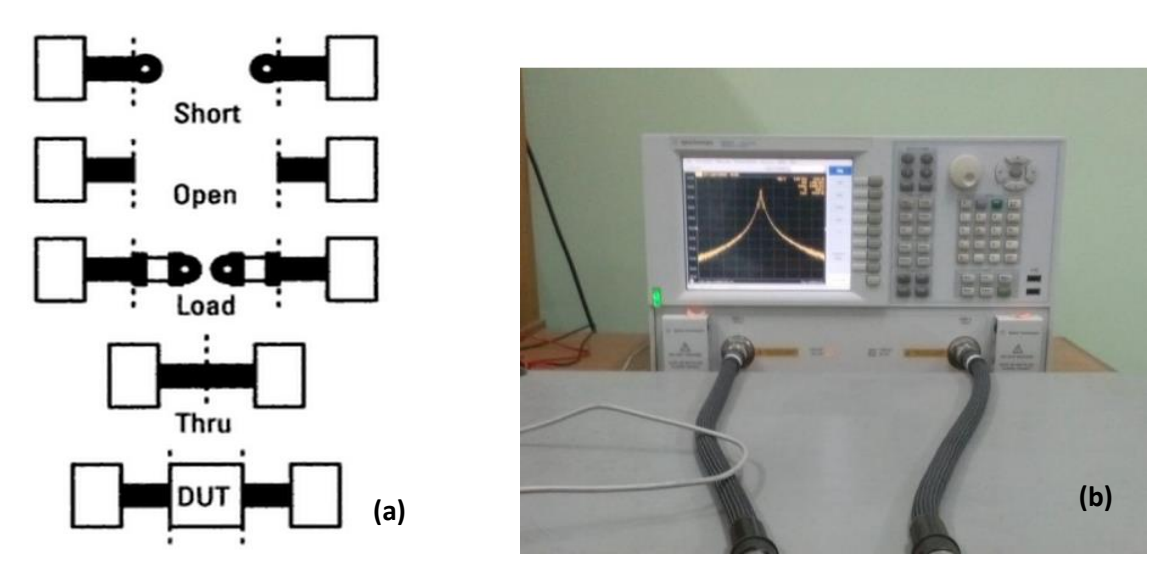


Fig 2. 17: (a) Microstrip SOLT Standards (Dotted Lines indicate Calibrated Reference Planes) (b) Agilent VNA.

2.4.8 P-E Loop Measurement

The ferroelectric characteristics of the material are studied by measuring the P-E hysteresis loop. Precision LC II manufactured by Radiant technologies based on a Sawyer-Tower circuit is utilised for all the measurements reported in this work.

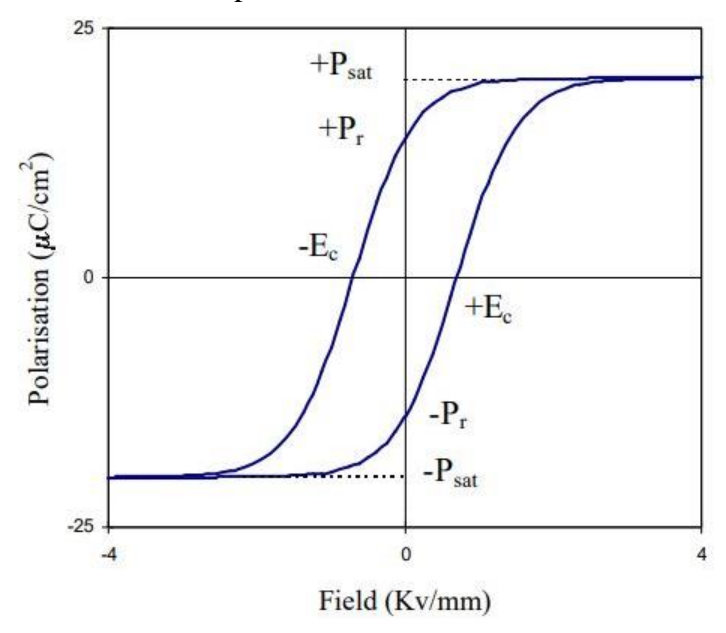


Fig 2.18: Schematic diagram of the P-E hysteresis loop of Ferroelectric materials [23]

Ferroelectric thin films were deposited on to an electrode coated substrate. Then, top electrodes for electrical measurements were deposited by RF sputtering technique and shadow mask. The plot consists of applied voltage/field, and the resulting polarisation at a given frequency is displayed through a P-E loop. The P-E loop of an linear dielectric capacitor is a straight line and a circle for an ideal resistor [24,25]. The important physical parameters of the hysteresis curve are marked in depicted in Fig 2.18.

2.5 Reference

- [1] C. Suryanarayana, Progress in Mater. Sci., 46, 1 (2001).
- [2] Milton Ohring, *Materials Science of Thin Films: Deposition and Structure* (2/e), Academic Press, USA, 2002.
- [3] S-J. Kang, Sintering, densification, grain growth and microstructure, Elsevier, Amsterdam, 2002.
- [4] D. Agrawal, Journal of Materials Education, 19, 49 (1999).
- [5] C. E. Holcombe and N. L. Dydes, J. Mater. Sci. Lett. 9, 425 (1990).
- [6] Peter E. J. Flewitt and Robert K. Wild, *Chapter 4- Physical Methods for Materials Characterisation*, CRC press, 2017.
- [7] Yang Leng (ed.), *Materials Characterisation*, 2/e, Wiley-VCH Verlag GmbH & Co, Germany, 2013.
- [8] B. D. Cullity, *Elements of X-RAY Diffraction* (2/e), Addison-Wesley Publishing Company, Inc., 1978.
- [9] Peter E. J. Flewitt and Robert K. Wild, Chapter 6-*Physical Methods for Materials Characterisation*, CRC press, 2017.
- [10] David B. Williams and C. Barry Carter, *Transmission Electron Microscopy: A Textbook for Materials Science*, Springer Science Business Media, LLC, 2009.
- [11] https://www.globalsino.com/EM/page3768.html
- [12] https://www.nanoimages.com/sem-technology-overview/
- [13] https://chem.libretexts.org/@go/page/148440
- [14] R. Swanepoel, J. Phys.E: Sci.Instrum, 16, 1214 (1983).
- [15] J.C. Tauc, F. Abeles., Optical properties of solids, North-Holland, Amsterdam, 1972.
- [16] H. Y. Tian, W.G. Luo, A.L. Ding, J. Choi, C. Lee, K. No, Thin Solid Films. **408**, 200 205 (2002).
- [17] Mark Fox, Optical Properties of Solids 2/e, Oxford University Press, 2010.
- [18] John R Ferraro, K Nakamoto and Chris W Brown, Introductory Raman Spectroscopy,

- Elsevier, (2003).
- [19] E Smith, G Dent, *Modern Raman Spectroscopy—A Practical Approach*, John Wiley & Sons Ltd (2005).
- [20] Shu-Lin Zhang, "Raman Spectroscopy and its Application in Nanostructures 1st edition", John Wiley & Sons, Ltd. (2012).
- [21] Alpha and Beta Dielectric, Conductivity, Impedance and Gain Phase Analyzers, User Manual, (Issue:4/2014 Rev.3.40) Novocontrol Technologies GmbH & Co.KG, Germany.
- [22] Ananjan Basu, An Introduction To Microwave Measurements, CRC press, 2015
- [23] S. Govergian, A. Tangantsev and A. Vorobiev, *Tuneable Film Bulk Acoustic Wave Resonators*, Springer, 2013.
- [24] Y. Xu, Ferroelectric Materials and Their Applications, North-Holland Elsevier Sci. Publ., Amsterdam 1991.
- [25] M. Stewart, M. G. Cain and D. A. Hall, Ferroelectric Hysteresis Measurement and Analysis, NPL Report CMMT(A) 152 (1999).
- [26] C. B. Sawyer and C. H. Tower, Phys Rev. 35, 269 (1930)

Chapter -3

In-situ crystallization behaviour of $Na_{0.5}Bi_{0.5}TiO_3$

3.1 Introduction

Ferroelectric thin films are explored for their integration in mainstream semiconductor industries, optoelectronic devices, sensors, memories, microwave devices and actuator applications [1-6]. Among perovskites, NBT is a potential material system for dielectric and ferroelectric applications [7–10]. NBT thin films have been deposited during the past few decades using a variety of deposition processes, such as pulsed laser deposition, the Sol-gel process, and RF sputtering. However, obtaining the pure phase remains challenging due to the presence of two volatile elements, Bismuth and Sodium. Among all described thin film deposition methods, PLD has more easily controllable parameters to optimize the thin film deposition process. PLD has laser-based parameters like pulse width, energy, repetition rate, frequency number of laser pulses or duration to control film quality and another set of independent chamber parameters like target-substrate separation or gap, substrate temperature, pressure and ambient gas or atmosphere and type of substrates. The individual control of these parameters provides additional freedom to vary and facilely obtain the required phase.

The substrate temperature greatly determines the crystal structure, orientation, stoichiometric composition, and morphology of as-grown films [11]. The in-situ substrate temperature provides thermal energy for the condensing species and enhances mobility. The crystalline phase development of the films depends on the nucleation of films, which is again controlled by substrate temperature.

3.2 Experimental Details: Deposition of NBT thin film

The pulsed laser deposition method is used to deposit NBT thin films from lab-made targets. At first, the required base pressure (4×10^{-6} mbar) is attained by evacuating the chamber using turbo pump. Then oxygen is allowed in a controlled manner to arrive at the working pressure of 3×10^{-2} mbar. The substrate is loaded in a substrate holder with heater facility at a fixed

distance (5 cm) from the target. The substrate temperatures varied from 300°C- 650°C and post oxygen for another 30 min to avoid oxygen vacancies. Fused silica substrates of dimension one inch by one inch are used for this study.

3.3 Results and Discussions

3.3.1 Structural properties

The XRD of the NBT films coated at various temperatures ranging from 300°C to 650°C on fused silica substrates is illustrated in Fig.3.1 The films prepared above 500°C are polycrystalline and films synthesized below 500°C are amorphous. The XRD pattern of films deposited in the range of 500°C to 650°C exhibit pure single-phase with rhombohedral structure and the films deposited at 650°C show a secondary phase peak at 30° corresponding to Bi₄Ti₃O₁₂ (JCPDF NO.03-065-2527). All the peaks in XRD spectra were identified and indexed. The occurrence of secondary phases is very common in NBT, because of the presence of highly volatile A site cations (Bi and Na) [12,13]. Crystallite size and strain were calculated by computing the FWHM of all the peaks by nonlinear curve fitting of individual peaks to the pseudo-Voigt function. The Debye-Scherer formula is used to compute the crystallite size.

$$crystalite \, size = \frac{0.9\lambda}{\beta \cos(\theta)} \tag{3.1}$$

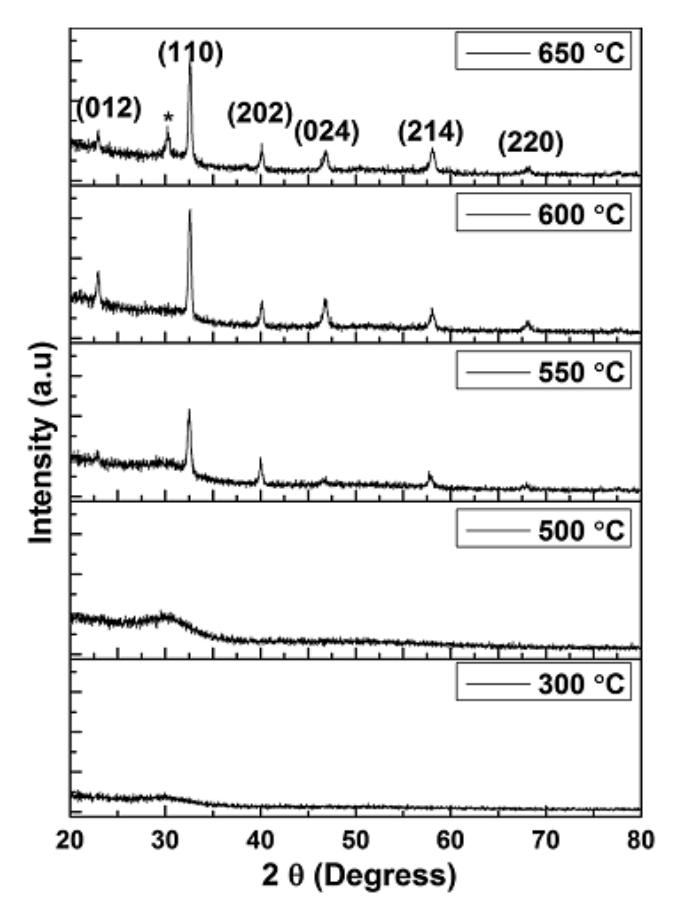


Fig 3. 1: XRD of NBT thin films deposited at various temperatures.

Where λ represent the characteristic wavelength of the XRD source and β is the FWHM of the peak corresponding to angle θ . The computed crystallite size increases with deposition temperature and has least residual strain. The software work based on nonlinear least-squares fit (with unit cell software [14]) is utilized to estimate the lattice constant and strain. Lattice strain is estimated from Eq (3.2),

$$strain = \frac{\beta \cos(\theta)}{4} \tag{3.2}$$

The results of the calculation are displayed in table (3.1)

Deposition temperature (°C)	Lattice par	ameters	Unit cell volume (Å3)	Crystallite size (nm)	Lattice strain
	a (Å)	c (Å)			
550	5.52	13.44	354.08	21.02	0.00165
600	5.50	13.43	351.99	24.57	0.00141
650	5.49	13.42	351.36	24.88	0.00139

Table 3. 1 Lattice constants of NBT thin film deposited at various substrate temperatures.

3.3.2 Microstructure properties

The microstructure features of NBT films prepared at various temperatures are observed by FE-SEM. The microstructure obtained for NBT films is presented in Fig. 3.2. The emergence of grain is visible with a rise in substrate temperature.

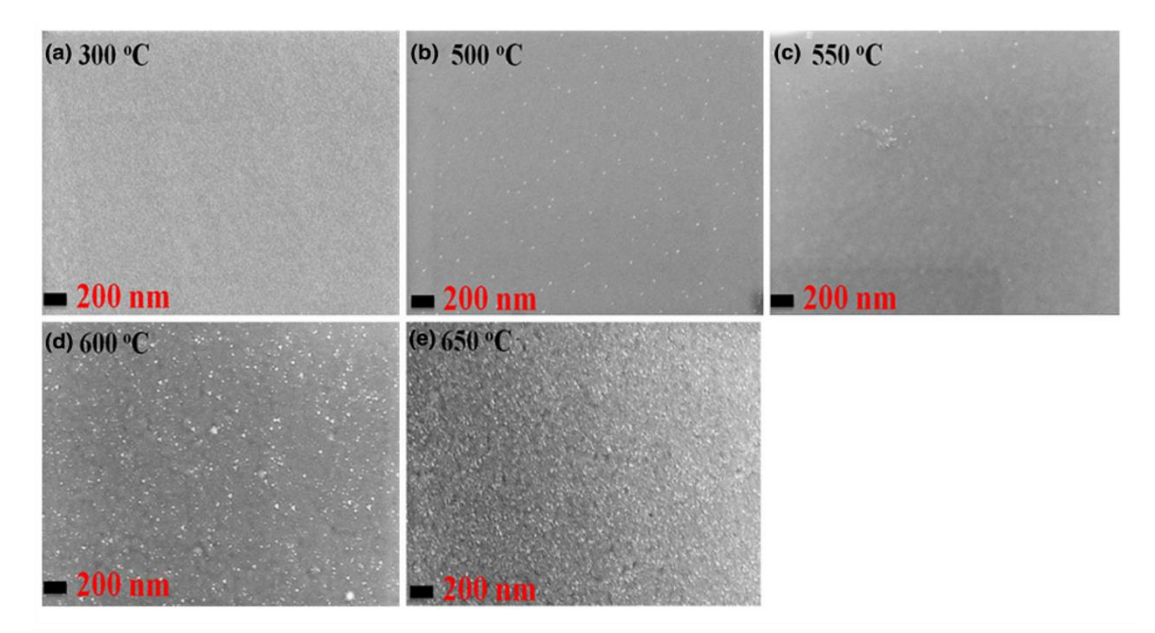


Fig 3.2 FESEM images of NBT thin films deposited at different substrate temperatures

Thin films coated below 550°C being amorphous, exhibits flat and smooth surface microstructure whereas, the film deposited above 550°C show rough and uneven surface structure. The rough surface in the FE-SEM images for the films deposited above 500°C denotes the initial phase of grain formation. It is difficult to differentiate the individual grains from these FE-SEM pictures since the grain boundaries are not yet distinct enough.

3.3.3 UV -VIS-NIR spectroscopy

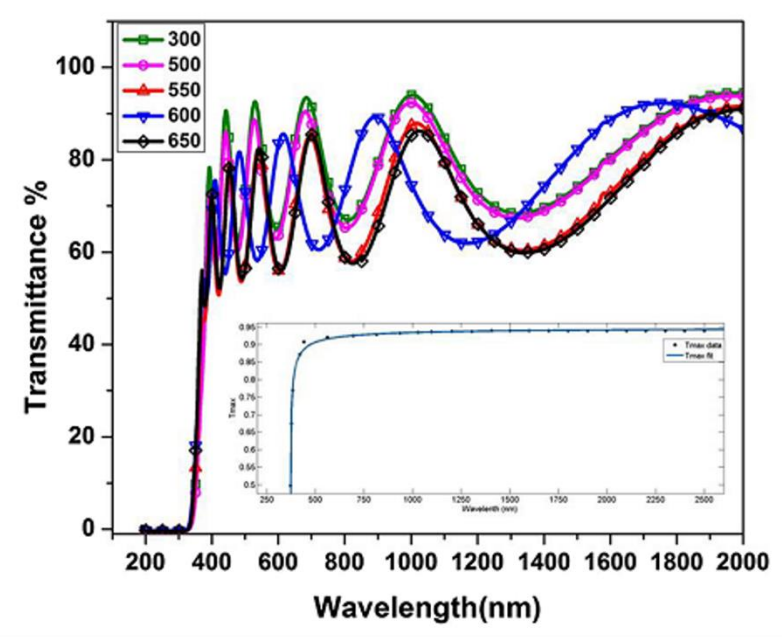


Fig 3. 3: Transmission spectra of NBT films deposited at various substrate temperatures and inset show fitted asymptote for T_{max} obtained for films deposited at $550^{\circ}C$.

Ferroelectric materials may be treated as molecules having a heavier positive core and lighter bound electrons in which their centre of positive and negative charges do not coincide. The optical characteristics of FE materials largely depend on the movement of bound charges. When light interacts with materials, the electric field excites the core and bound charges. Since the cores are much heavier, the Eigen frequencies of vibration of the core are much smaller than that of the bound electrons. Hence for high-frequency treatment, we can neglect the motion of the core. The general classical oscillator model may be derived by considering a bound charge q interacting with the electric field and stretches to position y, and vibrates about its equilibrium position (y=0). The equation of motion of such a charge is similar to forced oscillatory motion with damping having an Eigen frequency ω_0 . Corresponding dipole moment of a single dipole is

$$p = \frac{q^2 E}{m} \frac{1}{\omega_0^2 - \omega^2 - 2i\gamma\omega}$$
(3.3)

Hence the frequency-dependent polarizability may be written as

$$\beta = \frac{q^2}{m\varepsilon_0} \frac{1}{\omega_0^2 - \omega^2 - 2i\gamma\omega} \tag{3.4}$$

This-dispersion model is often referred as the Lorentzian oscillator model.

The optical spectra of NBT films coated at different temperatures is presented in Fig 3.3. The presence of well-defined oscillations in all of the transmission spectra originating from the multiple reflections from film and substrate interfaces confirms the uniformity in thickness of deposited films.

Dielectric characteristics of NBT thin films at optical frequency ranges are computed following the Swanepoel envelope [15] procedure. In this method, one asymptote through the maxima's and the other through the minimum of interference fringes is drawn over the normalized transmittance spectra. These asymptotes connecting extremes of interference fringes T_{max} and T_{min} are then fitted to the equation (3.5)

$$T = a - \frac{1}{((\lambda - b))^p} \tag{3.5}$$

Where **a** represents the limiting value of transmittance at a short frequency limit and b is the value for λ when the T is close to zero, and p parameter represents the changes in value of function T.

In the strong absorption region (T<0.4), scattering losses dominate for all measured optical spectra and show a strong absorption around 340nm. The absorption coefficient α is expressed by Eq (3.6)

$$\alpha = -\ln\left(\frac{T}{d}\right) \tag{3.6}$$

Here d represents film thickness and T is the optical transmittance. Tauc relation is used to calculate the optical band gap and its type.

$$(\alpha h\vartheta)^r = A(h\vartheta - E_g)$$
(3.7)

Where E_g represent the band gap, 'A' is the empirical constant and 'r' characterizes the type of electronic transition in material. The value of 'r' is equal to 2 for allowed direct transition and 'r' takes the value of 1/2 for allowed indirect transition. 'r' is equal to 2/3 and 1/3 for direct and indirect forbidden transitions.

The refractive index of thin films was determined using Swanepoel [16-18]

$$\mathbf{n}_1 = [N_1 + [N_1^2 - \mathbf{s}^2]^{1/2}]^{1/2}$$
(3.8)

Where,

$$N_1 = 2s \left[\frac{(T_M - T_m)}{(T_M + T_m)} \right] + \frac{(s^2 + 1)^2}{2}$$

All the required fitting is performed using python software using NumPy, SciPy Pandas and Matplotlib library in python. In bulk materials, the refractive index mainly depends on intrinsic parameters. However, in thin films, extrinsic parameters like the film thickness, phase quality, synthesis condition, microstructure, dislocation and vacancies also impact the value of the refractive index. Thin films in the amorphous phase (prepared at 300°C and 500°C) show a slightly smaller value refractive index compared to crystalline films (Fig 3.4a) due to their inherent reduced packing density. The extinction coefficient of all the films increases with wavelength as shown in Fig 3.4(b). The dielectric characteristics also exhibit a similar trend in their values for amorphous and crystalline films. The literature explains it by treating the amorphous phase as a highly collapsed lattice of very low packing density and a substantial number of defects [19].

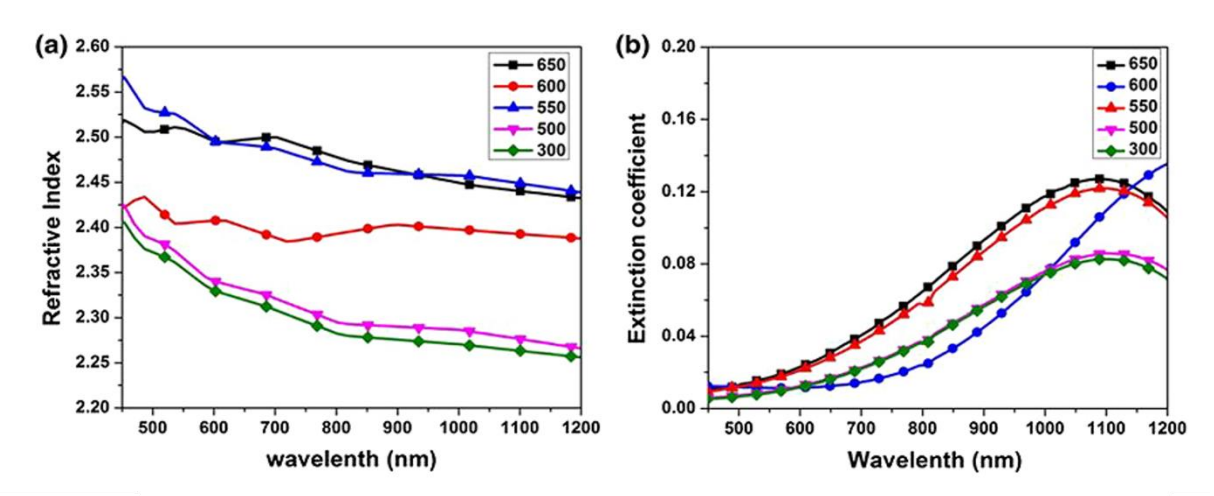


Fig 3. 4: (a) The refractive index of NBT thin films deposited at various substrate temperatures (b) The Extinction coefficient (k) of deposited NBT thin films.

Extending the classical oscillator model presented earlier to multi oscillator model yield Eq (3.9),

$$\beta = \frac{q^2}{\varepsilon_0 m} \sum_{i=1}^{M} \frac{f_j}{\omega_{0j}^2 - \omega^2 - 2i\omega\Gamma_j} = \frac{3}{N} \frac{\hat{n}^2 - 1}{\hat{n}^2 + 2} = \frac{3}{N} \frac{\varepsilon - 1}{\varepsilon + 2}$$
(3.9)

Here f j represents the relative strength of absorption lines. In the transparent region of the spectrum far from resonance we may write

$$n^{2} - 1 = \sum_{i} \frac{s_{i} \lambda_{i}^{2}}{1 - (\frac{\lambda_{i}}{\lambda})^{2}}$$
(3.10)

The above eq (3.10) is known as the Sellmeier dispersion formula, and S_i denotes the strength factor. If we assume that a single oscillator dominate and combine the contribution of all other oscillators to a constant, we obtain single term Sellmeier equation (3.11)

$$\frac{1}{n^2 - 1} = \frac{1}{S_0 \lambda_0^2} - \frac{1}{S_0 \lambda^2} \tag{3.11}$$

where S_0 represent oscillator strength and λ_0 is inter- band transition wavelength of the assumed single oscillator. We fitted our measured refractive index with the above equation in python software and extracted the parameters. Among calculated parameters, the dispersion energy and Oscillator peak energy corresponding to films deposited above and below 500°C shows a noticeable difference. This may be a result of the lower structural density and presence of dislocations in the amorphous phase compared to the crystalline phase. Calculated paters are tabulated in the table (3.2)

Deposition temperature (°C)	S0*10 ¹⁴ m ⁻²	λ_0 (nm)	E ₀ (eV)	E _d (eV)	Band gap (eV)	nα
300	0.875	212.13	5.85	23.11	3.72	2.23
500	1.099	194.42	6.38	26.59	3.61	2.27
550	2.396	146.28	8.48	43.61	3.64	2.47
600	3.336	119.58	10.37	49.63	3.68	2.40
650	3.238	125.29	9.90	50.49	3.65	2.46

Table 3. 2: Single oscillator dispersion parameters of NBT thin films deposited at various substrate temperatures estimated by fitting experimental data with Sellmeier formula

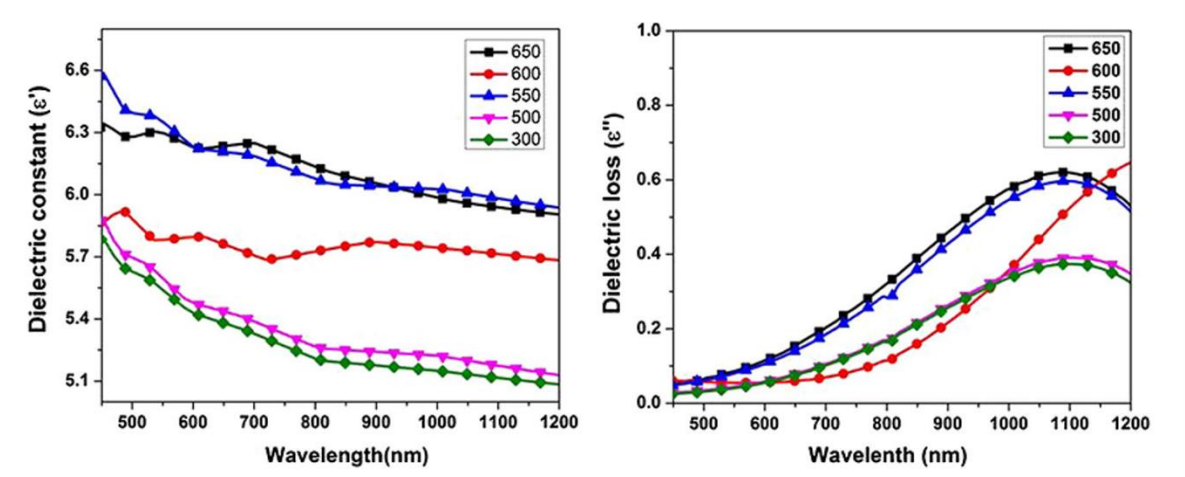


Fig 3. 5: Variation of dielectric constant and dielectric loss of NBT thin films with wavelength

The propagation of electromagnetic waves through a material is controlled by the dielectric characteristics of the material. The real and imaginary part of the dielectric constant is obtained from the complex refractive index determined from the optical spectra and is presented in Fig 3.5. The dielectric constant of NBT thin films shows a variation of 6.6 to 5 and the dielectric loss from 0.01–0.6 for the measured frequency range. All the films show normal dispersion behaviour in the dielectric spectrum. The value permittivity drops with an increase in the wavelength. In addition, the amorphous NBT thin films show lower dielectric constant and loss compared to their crystalline counterparts.

3.3.4 Raman spectroscopy

Raman spectroscopy is a resourceful tool fulfilling the technological needs for locally and quantitatively investigating the composition, crystal symmetry and orientation, residual stress and strain and amount of different phases in the ferroelectric material. Since the position of Raman lines is determined by the amount of energy exchange between the photon and quantized vibrational levels in a material system, the mere presence of particular Raman lines or bands can confirm the existence of a particular crystallographic phase or species. Similarly, the height of the Raman peak provides a fraction amount of the specific crystal structure. The subsequent straightforward task is identifying the Raman-allowed modes and their symmetries satisfying the selection rule. Figure 3.6 depicts the Raman spectra of NBT films measured from 100 to 1200 cm⁻¹. The irreducible representation from the group theory analysis for the R3c space group with A site disorder may be represented as [20,21]:

$$\Gamma = 4A_1 + 9E \tag{3.12}$$

The Raman spectra of NBT material are often categorized into different bands represented as A, B, C, and D. But in our spectrometer, a notch filter is used to avoid stray light elastic scattering. As a result, it cuts down the A band which is close to Rayleigh the line. Hence we divide our observed spectra into B, C and D bands. These bands are then de-convoluted into multiple peaks as shown in fig 3.6. The Centre of the peak and FWHM are obtained from the fit for individual peaks and are tabulated in Table 3.3.

Deposition temperature (°C)	P1	P2	P3	P4	P5	P6	P7	P8
300	251.41	292.72	352.33	436.66	538.46	727.14	784.65	
Amorphous	(40.22)	(53.89)	(78.03)	(114.75)	(163.11)	(349.65)	(112.09)	
500	252.85	302.67	366.25	456.03	566.06	742.43	809.80	
Amorphous	(60.94)	(74.97)	(106.28)	(150.45)	(181.32)	(113.82)	(74.52)	
500	251.71	288.12	338.88	483.56	591.65	732.88	787.89	845.54
Crystalline	(47.24)	(59.74)	(97.03)	(170.41)	(145.97)	(67.633)	(107.63)	(64.01)
550	251.72	295.02	346.84	494.71	585.71	744.02	801.93	856.27
Crystalline	(67.69)	(70.81)	(103.2)	(162.08)	(129.93)	(65.23)	(144.98)	(50.13)
600	253.36	293.18	340.48	500.45	592.10	726.34	769.69	837.40
Crystalline	(46.87)	(61.04)	(92.71)	(167.92)	(126.47)	(45.92)	(79.59)	(110.16)
650	248.25	283.38	332.16	506.88	593.28	729.82	765.61	831.68
Crystalline	(40.86)	(57.54)	(94.56)	(169.30)	(107.13)	(46.88)	(66.76)	(136.65)

Table 3.3: The deconvoluted peaks and their FWHM of NBT thin films deposited at various The masses of the atoms and their bond strength decide the vibrational frequencies of a molecule. The bond strength is inversely correlated with the Raman shift, which is directly proportional to atomic masses. Therefore, displacement of the heavier Bi ions dominates the Raman modes in 109–134cm⁻¹ range. The modes in the frequency range of 155–187 associated with Na–O and 246–401cm⁻¹ is related TiO₆ vibrations. The modes of vibration in the 413–826cm⁻¹ region are the results of oxygen atom vibrations [20, 22].

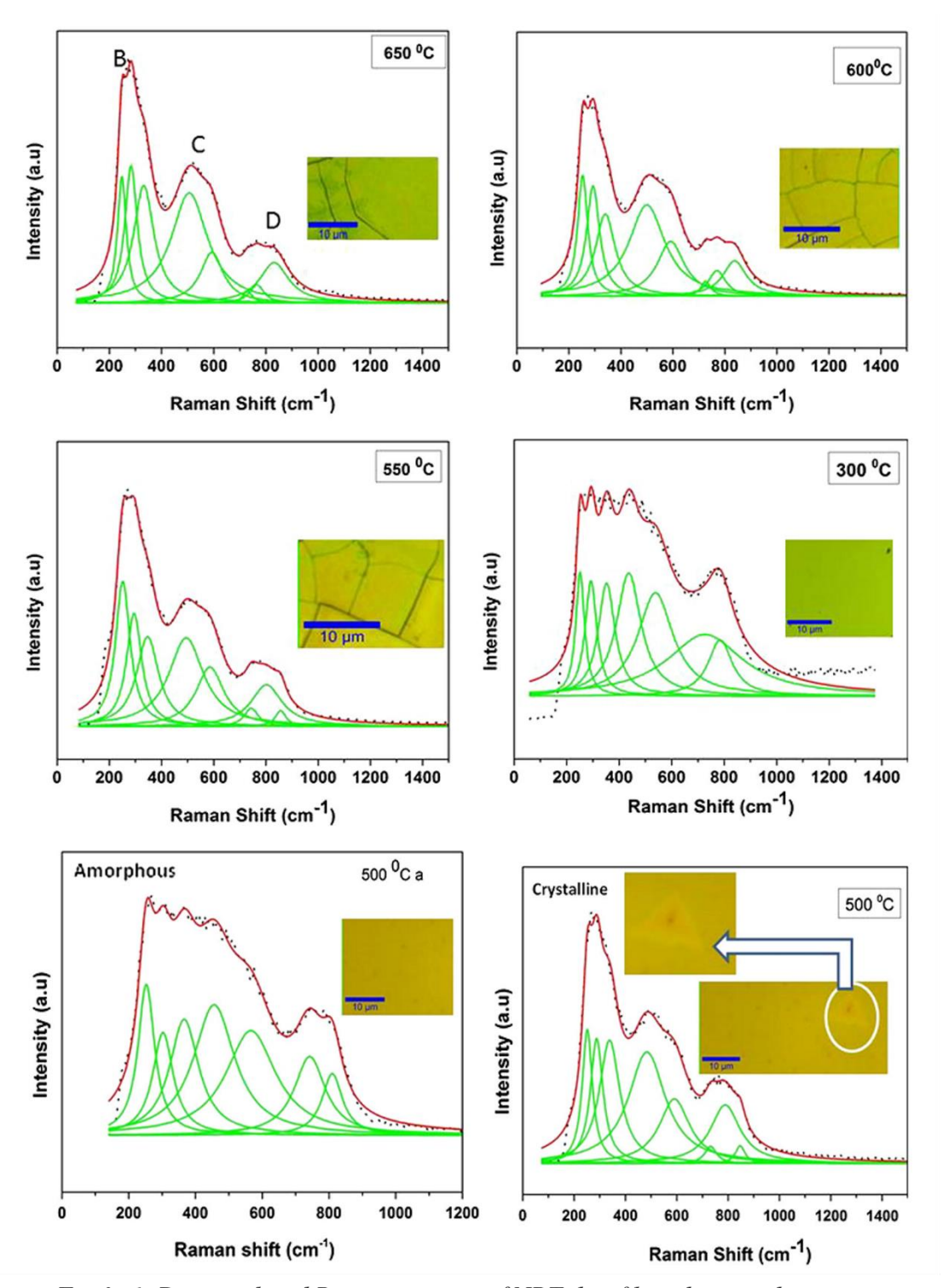


Fig 3. 6: Deconvoluted Raman spectra of NBT thin films deposited at various temperatures (Here Green lines are individual peak, red lines are cumulative fit and black dots are experimental data). The inset shows the portion where Raman spectra are measured.

The Raman spectra of thin films deposited at 500°C give two kinds of spectra when measured from different locations. The reason for the same is understood from the optical microscope images of the investigated area. A few discernible white patches (nucleation sites) are scattered throughout the film, and the Raman spectra obtained from these areas resemble those of the crystalline films. At the same time, the spectra obtained from other location is similar to the Raman spectra of amorphous NBT obtained for film deposited at 300°C. This demonstrates the capability of Raman spectroscopy to spatially identify the crystalline and amorphous phases.

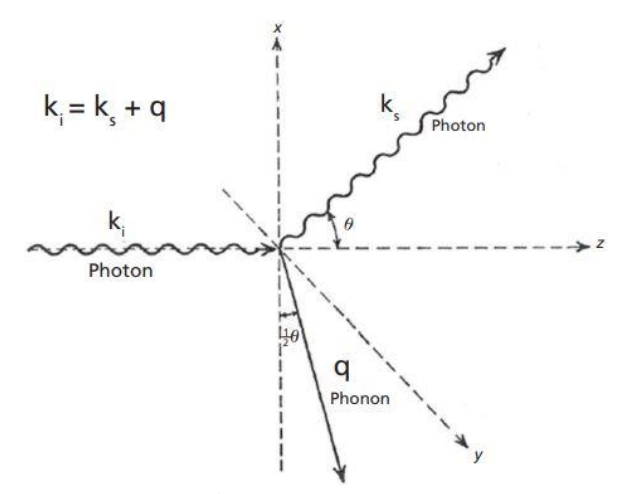


Fig 3.7: Raman scattering and conservation of wave vector in a crystal [24].

The Raman spectra of amorphous and crystalline solids often show remarkable differences which stems from the long-range order that persists in crystalline solids. In crystalline material, Raman spectroscopy can probe only regions near the Brillouin zone centre because of the requirement for the conservation of crystal momentum. A complementary technique like X-ray or neutron scattering is required to probe the remaining regions of the Brillouin zone. In contrast, the selection rules for Raman scattering from amorphous solid is more flexible, and the spectrum looks similar to the density of phonon for the first Brillouin zone. The difference in Raman spectra for crystalline and amorphous solids may be understood in the wave vector diagram shown in fig (3.7). The wave vector equation corresponds to the vector diagram solved for q gives eq (3.13),

$$q^{2}=k_{i}^{2}+k_{s}^{2}-2k_{i}k_{s}Cos\theta \tag{3.13}$$

Here the wave vector of the incident photon denoted by k_i , and k_s represent the scattered photon. In our experiment, we used a 532 nm Nd: YAG laser as a source and used a backscattering configuration. Assuming $k_i \simeq k_s$, we get $q \simeq 2k_i$, hence a rough comparison of magnitude of the wave vector of phonons with the k value of the Brillouin zone edge shows up a difference of three orders of magnitude. This essentially means that, in crystalline solids, the Raman spectra only probes longer wavelength phonons having smaller k value that exists near the Brillouin zone centre. But in the amorphous phase, the vibrational modes are not plane waves, and hence the conservation of the wave vector is relaxed. Thus all local vibrational modes contribute to the collected Raman spectra, equivalent to sampling the entire Brillouin zone [23-26].

To illustrate this point, consider NBT, the lattice constants are a =5.5 Å and c = 13.4 Å. If we use laser of 532 nm wavelength for recording the spectrum. Since the Raman shift are negligible we can assume that k_1 = k_2 and we have q= k_1 - k_2 and phonon with maximum q could be collected in backscattering geometry in that case is q=2 k_1 . Therefore, the maximum accessible region of q is equal to 4 π * n / λ =5.6 X 10⁷ m⁻¹ whereas the edge of Brillouin zone π /a = 5.7 X 10⁹ m⁻¹ thus Raman scattering only probe the region close to the BZ centre.

3.4 Microwave dielectric properties of NBTfilms

Dielectric characteristics of NBT thin films at 10 GHz and 20 GHz are determined by the SPDR method. It is a general method used to precisely determine the dielectric characteristics of dielectric sheets or flat slabs and thin films [27, 28].

The sample is required to be inserted into the gap between the split resonators to perform this measurement and hence the maximum permissible thickness is less than the gap of the SPDR set up. For 20 GHz, the air gap is approximately 0.6 mm, which limits the measurement to films coated on thin substrates. The computation of dielectric properties using SPDR is based

on TE_{01d} mode, having electric field only in azimuthal direction hence field is continuous on the resonators. Before performing the measurement, VNA was calibrated (two port SLOT calibrations).

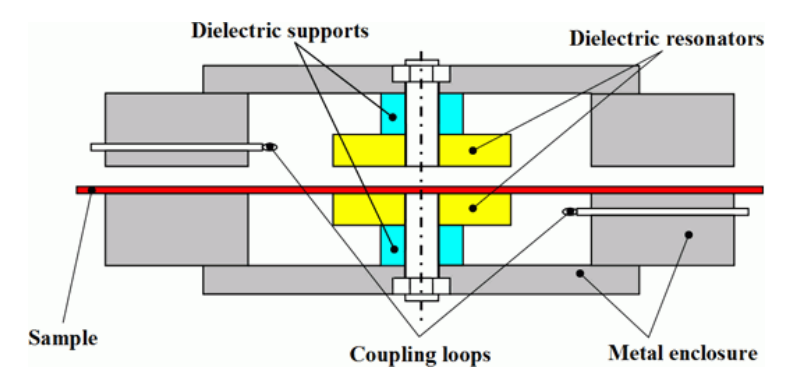


Fig 3. 8: The SPDR fixture used for dielectric measurement [30]

The complex permittivity of thin films is estimated by measuring shift in the resonant frequency and quality factor. At first the quality factor and resonant peak of the fixture containing bare substrate is measured then film coated substrate is inserted carefully in the same locations covering the entire dielectric resonators in the SPDR fixture and the resultant change in the resonant peak position and quality factor is noted. The iterative solutions to Eq 3.14 estimate permittivity from the measured parameters [29].

$$\varepsilon' = \frac{1 + (f_o - f_s)}{h f_o K_s(\varepsilon'_s h)} \tag{3.14}$$

Here f_0 and f_s are the measured resonance frequency of bare and film-coated substrate respectively and h denote the thickness of the films. Where Ks is a function of permittivity and thickness of the sample whose values are measured for different pairs and interpolated for unknown pairs of permittivity and thickness.

The loss tangent of the sample is estimated from the Eq 3.15.

$$\tan \delta = \frac{Q^{-1} - Q_{DR}^{-1} - Q_c^{-1}}{p_{es}}$$
 (3.15)

Where Q- unloaded Q-factor of the resonant cavity with the sample,

pes - electric energy filling factor

Q_c - the Q-factor associated with metallic losses of the fixture with the sample.

Q_{DR}- Q-factor related to the losses in the resonators.

Dielectric characteristics of NBT thin films determined by the SPDR technique at microwave frequency (10 GHz) for the films deposited at different temperatures are tabulated in Table.

3.4. The measured values show a slight frequency dispersion in the microwave range.

Deposition Temperature	300 °C	550°C	600°C	650 °C
Dielectric constant	165	181	186	183
Dielectric loss	0.341	0.381	0.361	0.374

Table 3.4: Dielectric characteristics of NBT films determined at 10 GHz.

3.5 Conclusion

In this chapter, we analysed the role of deposition temperature on determining the structural, optical and microwave dielectric characteristics of NBT thin films deposited on fused silica substrates by PLD method. Thin films coated below 550°C were in the amorphous phase, and thin films coated at 650°C showed a secondary phase. The crystallite size and unit cell volume increase with deposition temperature. UV- Vis NIR transmission spectra of all the deposited films are measured and used to derive optical parameters like refractive index, extinction coefficient, complex permittivity, and band gap. Among the single-phase films, the films deposited at 600°C has a larger crystallite size and lower dielectric loss than films deposited at 550°C. Increasing the deposition temperature above 600°C is not a suitable choice since it may lead to Na and Bi loss and the formation of secondary phases. Optical spectra of the deposited

films exhibit normal dispersion near shorter wavelength region point to interband electronic transition. The dispersion behaviour has been described by a single electronic oscillator model with oscillator energies of 5.85eV and 10.37eV for amorphous and crystalline NBT thin films, respectively. Optical characteristics of the crystalline and amorphous films show a significant difference in their properties, which may be arising from the coordination defects and short-range order in amorphous material. The other important observation is the remarkable difference in the Raman spectra of amorphous and crystalline NBT thin films. This difference is explained on the basis of conservation laws in crystalline solids. The films deposited at 500°C show both amorphous and crystalline region, which is identified by optical microscopy and confirmed by Raman spectroscopy. The microwave frequency dielectric characteristics are measured using the SPDR technique, and the permittivity of amorphous films is slightly lesser than the crystalline thin films.

3.5 Reference

- [1] S. Kasap, P. Capper, *Springer Handbook of Electronic and Photonic Materials*, vol. 10. (Springer, New York, 2006), pp. 47–76.
- [2] M. E. Lines and A. M. Glass, *Principles and Applications of Ferroelectrics and Related Materials*, Oxford University Press, 1977.
- [3] Ashim Kumar Bain, Prem Chand, Ferroelectrics: Principles and Applications, WileyVCH Verlag GmbH &Co, 2017.
- [4] T.Y. Chang, R.W. Hellwarth, Opt. Lett. 10, 408–410 (1985).
- [5] J. Tian, H. Gao, W. Deng, H. Zheng, F. Tan, W. Zhang, J. Alloys Compd. 687, 529–533 (2016).
- [6] Lane W. Martin and Andrew M. Rappe, Nature Reviews Materials, 2, 16087 (2016).
- [7]C. Anil Kumar, D. Pamu, Appl. Surf. Sci. **340**, 56–63 (2015)
- [8] S.A. Sheets, A.N. Soukhojak, N. Ohashi, Y.M. Chiang, J. Appl. Phys. 90, 5287–5295 (2001).
- [9] D. Carbone, A.I. Pateras et al., Appl. Phys. Lett. 105, 242901 (2014).
- [10] Y.M. Chiang, G.W. Farrey, A.N. Soukhojak, Appl. Phys. Lett. **73**, 3683–3685 (1998).
- [11] Ohring M, The Materials science of thin films, Academic press Inc, 1991.
- [12] J.-R. Ducle `re, C. Cibertand et al., Thin Solid Films **517**, 592–597 (2008)
- [13] B.N. Rao, A.N. Fitch, R. Ranjan, Phys. Rev. B, 87, 060102 (2013).
- [14] T.J.B. Holland, S.A.T. Redfern, D. Street, Mineral. Mag. **61**, 65–77 (1997).

- [15] R. Swanepoel, J. Phys. E, **16**, 1214–1222 (2000).
- [17] K. Venkata Saravanan, K. Sudheendran, M. Ghanashyam Krishna, K.C. James Raju, J. Phys. D Appl. Phys. 42, 45401 (2009).
- [18] Andrews Joseph, J.P. Goud, E. Sivanagi Reddy, K.C. James Raju, AIP Conf. Proc. **1731**, 080039 (2016).
- [19] R. Thomas, D.C. Dube, Jpn. J. Appl. Phys. **39**, 1771–1775 (2000).
- [20] J. Petzelt, S. Kamba, J. Fabry et al., J. Phys.: Condens. Matter, 16, 2719–2731 (2004).
- [21] G. Pezzotti, J. Appl. Phys. 113, 211301 (2013).
- [22] M.K. Niranjan, T. Karthik, S. Asthana, J. Pan, U.V. Waghmare, J.Appl. Phys. **113**, 194106 (2013).
- [23] R. Zallen, The Physics of Amorphous Solids, Wiley, New York (1983).
- [24] Tuschel D, Spectroscopy 32(3), 26–33 (2017).
- [25] R. Tilley, *Crystals and Crystal Structures*, Wiley, Chichester (2007)
- [26] P.M.A. Sherwood, *Vibrational Spectroscopy of Solids*, Cambridge University Press, London (1972)
- [27] J. Krupka, W. T. Huang, and M. J. Tung, Ferroelectrics, **335**, 89–94 (2006).
- [28] A. Joseph, J. P Goud, E. S. Reddy, and K. C. J. Raju AIP Conference Proceedings, 1731, 080039 (2016).
- [29] J. Krupka, A.P. Gregory, O.C. Rochard, R.N. Clarke, B. Riddle, J. Baker-Jarvis, J. Eur. Ceram. Soc. 21, 2673 (2001).

[30] J. Krupka, R. G. Geyer, J. Baker-Jarvis, and J. Ceremurga, Seventh Intl. Conference on Dielectric Materials, Measurements and Applications Conf. Publ. No. 430, Bath, UK (37–40 SPDR) 21–24(1996).

Chapter 4

Dielectric, Ferroelectric and Tunable Microwave Properties of Na $_{0.5}Bi_{0.5}TiO_3$ Thin Films

4.1 Introduction

Ferroelectric materials like Ba_{1-x}Sr_xTiO₃ are most widely investigated for tunable microwave devices in their paraelectric state. Ferroelectrics below Curie temperature are in a polar state and are often not considered for tunable microwave devices. Among BST composition, the compositions for x=0.5 is only usually considered for tunable device applications. Domain wall movements, charged defects, polar nano regions, piezoelectric transformations (acoustic wave generation), and many other intrinsic and extrinsic losses are present in FE thin films. But few recently investigated FE materials systems show a low loss at relatively high frequency [1], which triggered the broadband characterization of ferroelectric materials in the high-frequency domain.

Although several reports are available on measuring the dielectric tunability of paraelectric thin films at various frequency regimes, few reports are available for the tunability of ferroelectric materials in microwave frequencies [2, 3]. This electric field tunable dielectric constant is incredibly useful for designing a variety of high-frequency devices, such as voltage controlled filters, phase shifters, second harmonic generators, delay lines, and for beam steering [4-6]. The most common application among them is tunable varactors, where the current state of art competing technologies are semiconductor diodes and RF MEMS capacitors and Table 5.1 compares the performance of FE varactors against these technologies [7]. Here we have investigated NBT, a member belongs to the BTO family and a promising composition for lead-free piezoelectric and ferroelectric applications.

This chapter discusses the electrical characteristics of NBT films grown on fused silica and Pt-coated sapphire substrates by a pulsed laser deposition technique. The crystalline phase of the films is confirmed by XRD. The room temperature complex permittivity of NBT films at low and microwave frequencies and dielectric tunability at high frequencies are measured using

interdigitated capacitance test structure. The dielectric permittivity of the measured film decreases with an increase in bias voltage. Showing a value of around 144 (at 1 GHz). The deposited films of thickness 200nm show a tunability of 9 % for a bias voltage of 70V at 1 GHz.

Device characteristic	Semiconductor diode	RF MEMS	Ferroelectric Varactor
Tuning DC voltage	LOW(<10V reverse bias)	High (40-50 V bipolar)	Low (<10V bipolar bias).
Quality factor	Q degrades drastically above 10 GHz(~200 at 1GHz)	High Q in microwave and millimeter region (>500 at 1 GHz)	Constant Q in millimeter frequencies(~200 at 1GHz)
Capacitance tuning ratio	>3:1 in linear range	>5:1 in linear range	~3:1 in linear range
Tuning speed	High (∼10ns)	Low (~10μs)	High (∼10ns)
Power handling	Poor (~1W)	Good (<5W)	Good (up to 5W)
Packing cost	Low	High	Low

Table 4. 1: Comparison of various state of art varactor technologies.

4.2 Deposition of NBT thin films

NBT thin films were deposited on Pt-coated sapphire substrates by PLD technique. Stoichiometric quantities of Na₂CO₃, Bi₂O₃ and TiO₂ powders of Sigma Aldrich (99.99%) is used to prepare the NBT targets. NBT thin films were prepared by irradiating the NBT target with a KrF excimer laser. Initially, the chamber is evacuated to reach the pressure of 5 x 10⁻⁶ mbar. Then oxygen is introduced to the chamber to reach the working pressure of 5×10⁻² mbar before starting the deposition. The deposition is carried out at 600°C with focussed laser beam of fluence of 2 J/cm² at target surface. These films deposited on Pt-coated sapphire are used for high-temperature dielectric properties and ferroelectric characterization. This chapter also

investigates the room temperature dielectric properties of NBT thin film deposited at various temperatures on fused silica.

4.3 Structural and microstructure properties

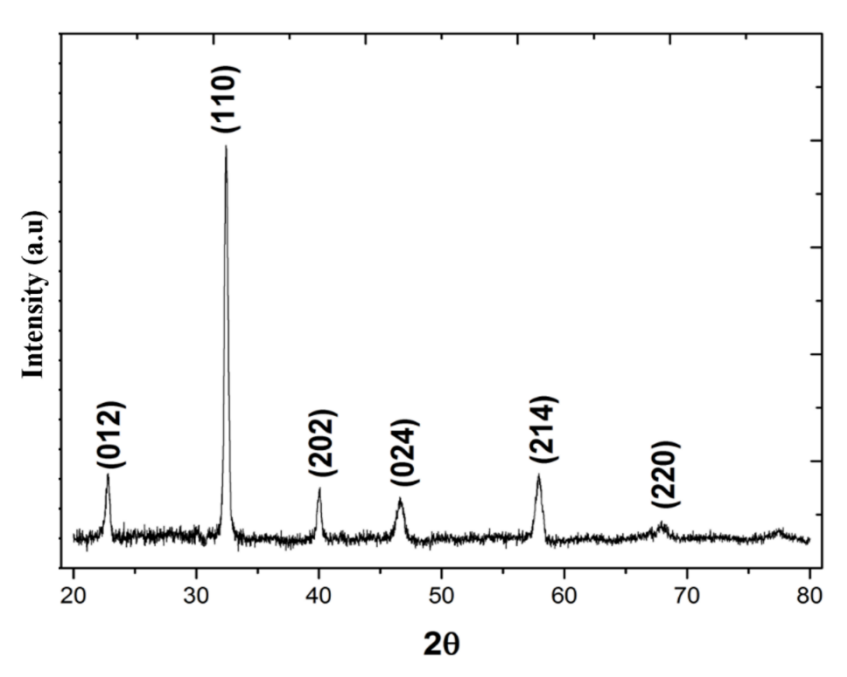


Fig 4. 1: X-Ray Diffraction pattern of NBT thin film on Pt-coated Sapphire.

Fig 4.1 shows the XRD of NBT film deposited on Pt-coated sapphire. The major (110) peak is observed at 32.5° confirming the perovskite structure. The crystallite size is calculated using the Scherer formula after fitting with the major peak with pseudo-Voigt function and found to be 24.37nm. The lattice parameters of the corresponding crystal is determined from the (h k l) values and peak positions from the XRD spectrum using unit cell software and found to be a=5.52Å and c=13.44Å.

4.4 Low-Frequency dielectric properties

4.4.1 Room temperature dielectric characteristics of NBT Thin films

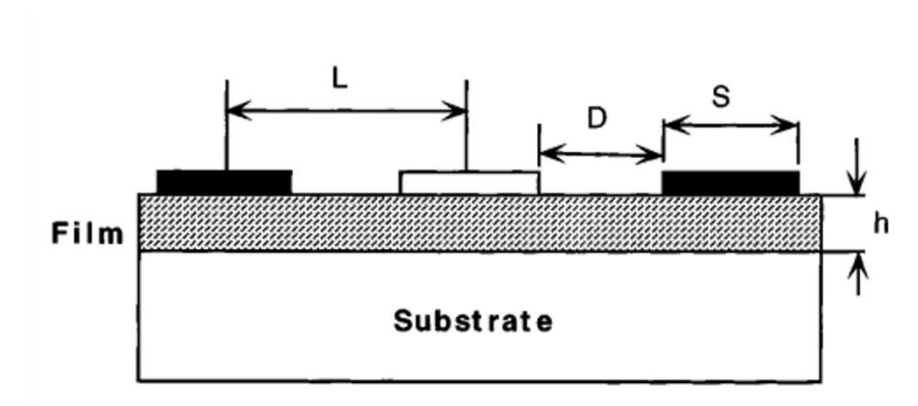


Fig 4. 2: A schematic of a cross-section of the capacitor structure [8]

The dielectric characteristics of the deposited NBT thin films are measured using Agilent 4294A impedance analyser. An interdigitated capacitor (IDC) based method proposed by D. Dimos et al [8] is followed to estimate the dielectric permittivity and loss. The IDC capacitors having 8 fingers of individual finger length equals 90µm is used for this purpose. The width and gap of the IDC fingers were chosen to be 10 µm. These IDC pattern were photo-lithographically transferred to the surface of the film and gold is used as the top electrode. An extensive description of the process is given in section 4.5. The cross-sectional view of electrode film and substrate is portrayed in Fig 4.2 and corresponding top view (SEM image) is depicted in Fig 4.3.

The analytical model developed by Farnel is used to compute the dielectric constant of thin film from interdigitated capacitor structure. According to this model, the permittivity for an IDC shown in Fig. 4.4 is given by eq (4.1):

$$\varepsilon_f = \varepsilon_s + \left(\frac{C - \left[A \left(1 + \varepsilon_s \right) \right]}{A \left[1 - \exp \left(\frac{-4.6h}{L} \right) \right]} \right)$$
(4.1)

Where ε_f and ε_s denote the NBT thin film's permittivity and the substrate's permittivity, respectively, the symbol h represents the thickness of the film, 'A' represents a numerical constant with a unit of capacitance, and C is the measured capacitance. The value of 'A' depends on the ratio of finger width and spacing of the IDC pattern; here, both are equal (L = 2D); hence the value of 'A' is 4.535pF. The measured capacitance (C_m) is related to C used in eq 4.1 by

$$C = \frac{C_m}{LF * N} \tag{4.2}$$

Where N is the number of sections of width L and LF denotes the finger length measured in meters. The count of segments with width L in an IDC having P pairs of fingers is given by Eq (4.3) [9,10]

$$N = 2P - 1 \tag{4.3}$$

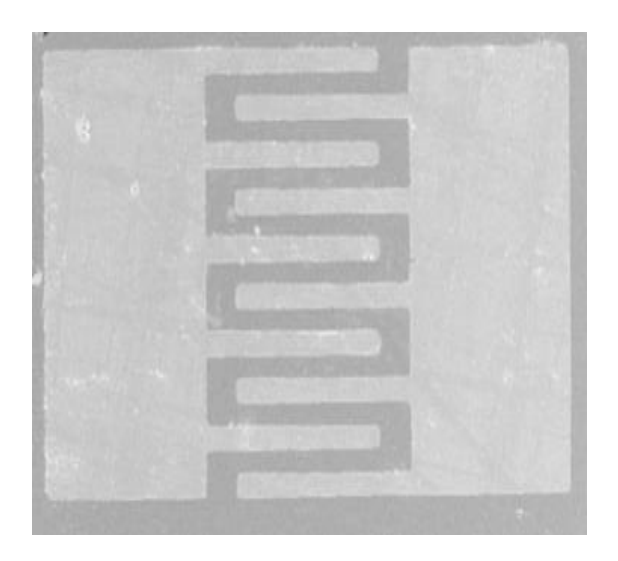


Fig 4.3 :FE-SEM image of fabricated IDC

The change in permittivity and loss tangent of NBT thin films with frequency measured from 50Hz to 1MHz at room temperature is given in Fig4.4. Initially, the dielectric constant of all the films decreases smoothly and exhibits normal frequency dispersion. Dielectric loss also shows a similar trend. The deposited films show a high dielectric constant with low loss, which is an indication of good quality for the deposited films. The dielectric constant varies in the range of 360 to 320 with highest dielectric constant for films deposited at 600°C. The obtained dielectric constant and loss values are comparable to previous studies on NBT thin films by various groups [11-13]

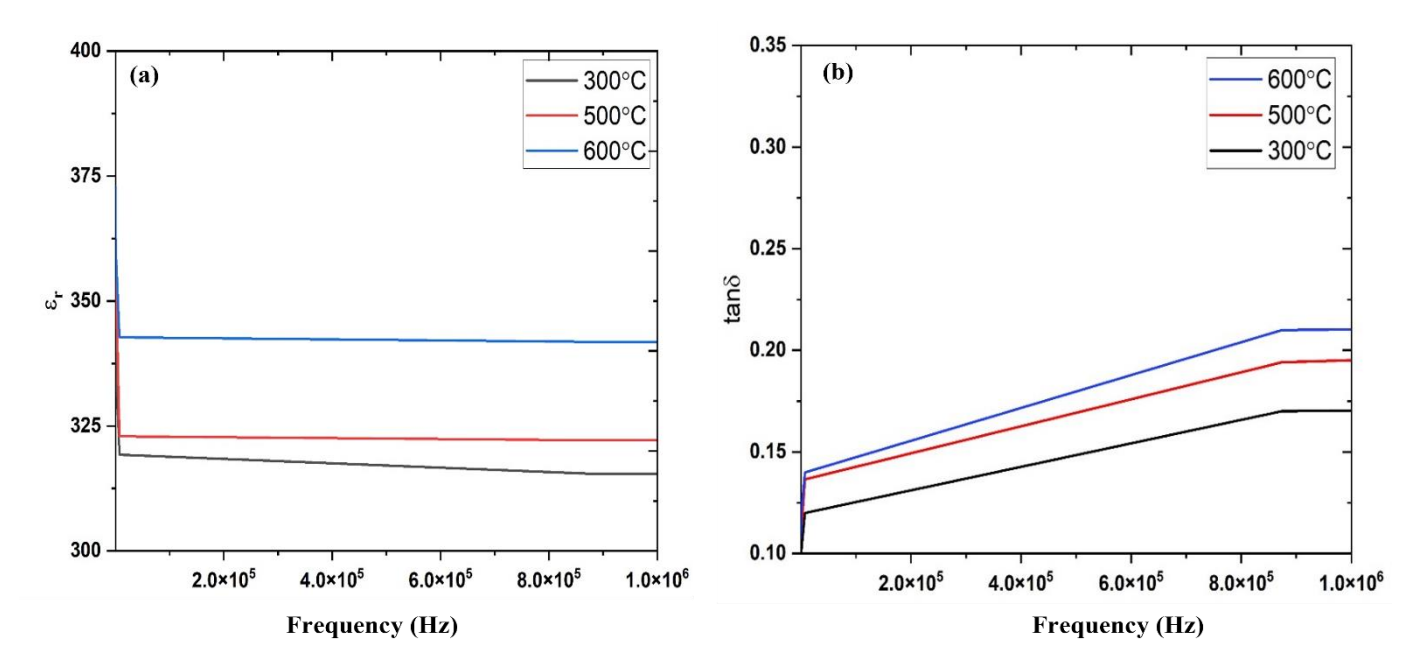


Fig 4.4:. The frequency-dependent (a) dielectric constant (b) dielectric loss tangent of NBT thin film deposited at various temperatures.

The dielectric properties of NBT thin films are strongly influenced by the deposition temperature. NBT thin films deposited on fused silica substrates at 300°C, 500°C and 600°C were used to investigate the role of substrate temperature on dielectric characteristics. As we increase the deposition temperature, dielectric constant also increases as depicted in Fig 4.4. This may be due to improvements in density, grain size and the crystallinity of films deposited at elevated temperatures. Compared to crystalline thin films, it has been found that amorphous

thin films have a reduced dielectric loss. This is because the amorphous phase is devoid of lattice modes, hence reduced intrinsic loss.

4.4.2 Temperature dependent Impedance spectroscopy

Temperature dependent variations in the complex impedance of the NBT thin films deposited on Pt-coated sapphire were investigated by Agilent 4294A impedance analyser. The impedance measurement is carried out to investigate the conductivity behaviour and to understand the mechanism of electrical conduction. The obtained impedance spectrum contains resistive and reactive components. Hence an equivalent circuit (or reaction) modelling is used to interpret the measured impedance data. Microstructure significantly impacts the transport properties of polycrystalline thin films, and impedance spectra typically show characteristics that are directly connected to microstructure. Here we used the brick-layer model proposed by Beekmans and Heyne. This model treats polycrystalline materials as a collection of grain separated by flat grain boundaries [14,15]. The real and imaginary part of complex impedance Z, whose magnitude decreases with frequency, is measured in the range of 100 Hz to 5 MHz at different temperatures. Nyquist (Cole-Cole) plot is drawn by plotting-Im(Z(freq)) over Re(Z(freq)) and shown in fig 4.5. The simplest or idealized spectrum and their corresponding equivalent circuit elements are presented in table 4.2 [16]. In order to analyse the experimental data, we

smoothed and fitted the data to a semi-circle in Z-plane using commercially available Matlab software.

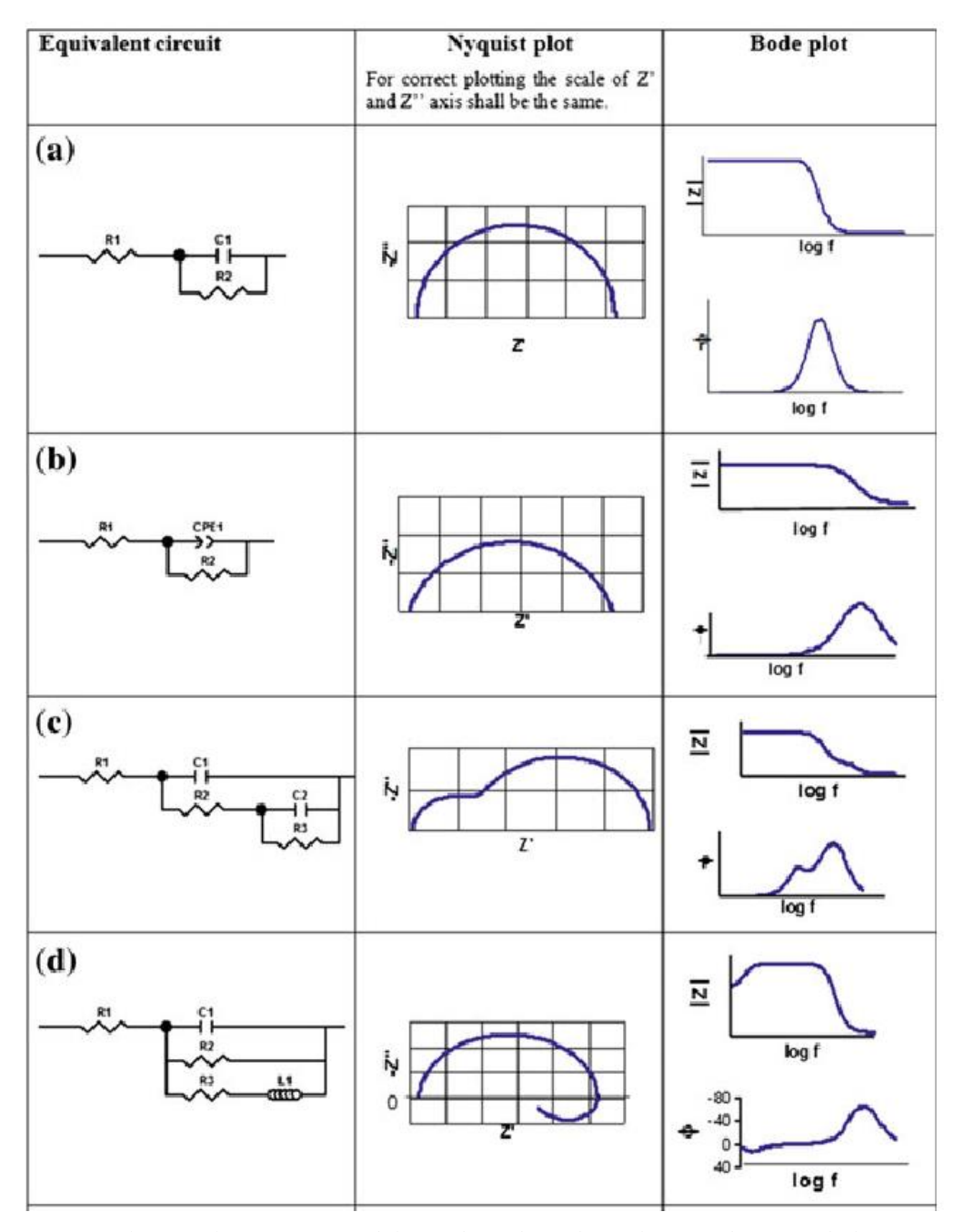


Table 4.2 Typical equivalent circuit models used for describing the impedance of dielectric materials and their corresponding Nyquist and Bode plots[16].

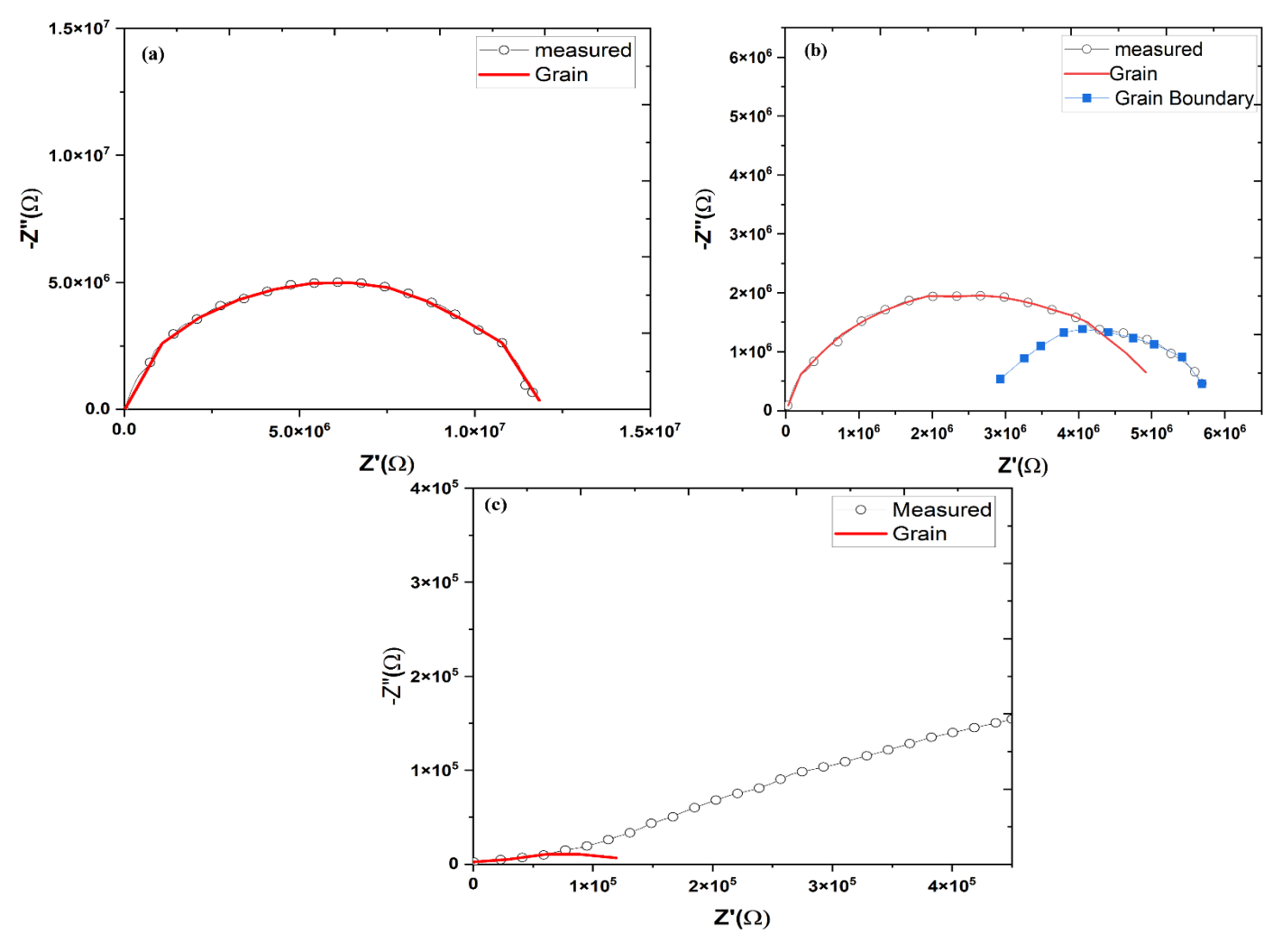


Fig 4.5: Cole –Cole plot of NBT thin films measured at (a) 100°C (b)150°C (c) 200°C

The centres of fitted semicircles did not lie on the real x-axis and is a depressed semicircle similar to row (b) in Table 4.2. This depressed circular arc behaviour originates because of the distribution of relaxation times around a mean relaxation time in the material system. Fig 4.5(a), corresponding to measurement at 100°C, is well fit to a depressed single semicircle indicating that the dominant contribution is from the grain interior. At 150°C (fig 4.5(c)) onwards, another semicircle emerges near the low-frequency regime, related to the grain boundary, differentiated by higher resistance compared to the grain interior. The radius of the low-frequency circle is predominately grow with the rise in temperature. A typical data set

measured at 200°C is shown in fig 4.5(c). Table 4.3 lists the values of the grain resistance (Rb) and related bulk capacitance (Cb) of the NBT thin films at various temperatures.

Temperature	$R_b(\Omega)$	C _b (F)	$R_{gb}(\Omega)$	C _{gb} (F)
100°C	1.18x10 ⁷	2.68x10 ⁻¹⁴	-	-
150∘C	2.55x10 ⁶	1.05x10 ⁻¹¹	5.8x10 ⁶	3.85x10 ⁻¹²
200°C	1.4x10 ⁵	2.39x10 ⁻¹⁰	-	-

Table 4.3 Estimated capacitance and resistance values corresponding to each semicircle in the Cole-Cole plot.

4.5 Broadband high-frequency dielectric measurement

Interdigitated capacitors (IDC) are fabricated on PLD deposited films using photolithography and RF sputtering system. The S parameter is measured from 0.6 GHz to 3 GHz using an Agilent Vector Network Analyser. Before the measurement, a one-port SLOT calibration is performed. The average thicknesses of the NBT thin films were determined using a surface profilometer and optical method it was found to be 200 ± 10 nm.

4.5.1 Conformal mapping of IDC structure

Interdigitated capacitors (IDC) structure-based method is employed to determine the microwave frequency dielectric characteristic of NBT films. The IDC having fingers =10 and finger width = $10 \mu m$, and finger length = $180 \mu m$ is used for this purpose. S_{11} of structures was measured from 1 to 3 GHz using a vector network analyser. The S parameter of the thin films was measured as a function of frequency and DC voltage. A schematic of IDC is shown in fig 4.5.

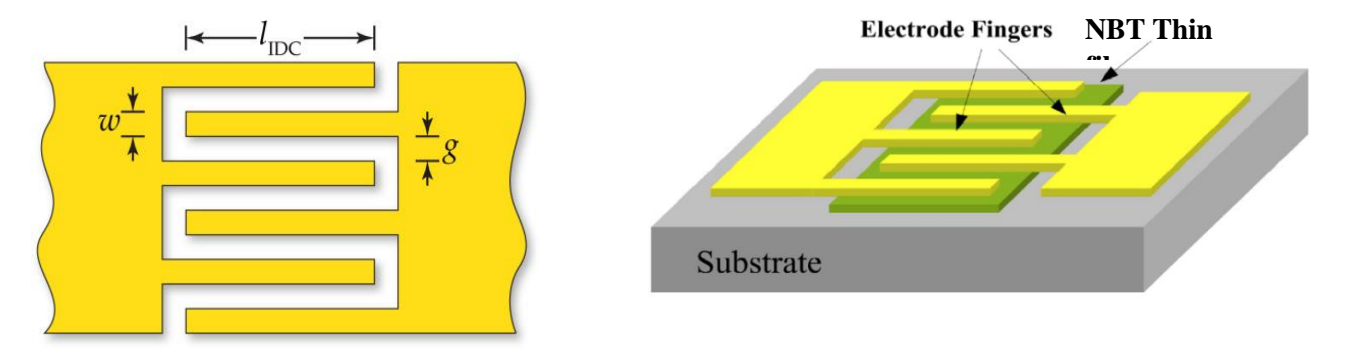


Fig 4.6: Schematic representation of IDC structure

The major capacitance of an IDC has a contribution from individual finger capacitance and that between the fingers and the effective capacitance of finger ends. Hence total capacitance of the IDC may be written as the sum of three capacitances [17]

$$C = C_3 + C_n + C_{end} \tag{4.4}$$

Where C_3 denote capacitance formed by the two outer one-and-a-half fingers IDC, and C_n represents the capacitance of a periodical (N -3) structure. The capacitance caused by each finger's open ends is represented by C_{end} .

Analytical expressions for each term in Eq(4.4) are obtained using a conformal mapping technique transforming an IDC on a single layer into a parallel plate capacitor. The three capacitances are given as [17,18]

$$C_3 = 4e_0 e_3 \frac{K(k_{03})}{K(k_{03})} l \tag{4.5}$$

$$C_n = (n-3)e_3 e_n \frac{K(k_0)}{K(k_{0n})} l$$
(4.6)

$$C_{end} = 4ns(2+\pi)e_0e_{end}\frac{K(k_{0end})}{K(k_{0end})}$$
(4.7)

Python code is written to obtain the permittivity from these equations. Initially, S_{11} is measured by on-wafer probing and capacitance is derived from this measurement.

4.5.2 Fabrication of IDC

The process steps followed to fabricate ferroelectric varactor can be summarized as cleaning substrate, coating a thin film, photoresist coating, exposure, development, etching, and lift-off process. These processes are carried out in a clean room facility available in the Nano-centre of University of Hyderabad. The fabrication process flow is depicted in Fig. 4.7.

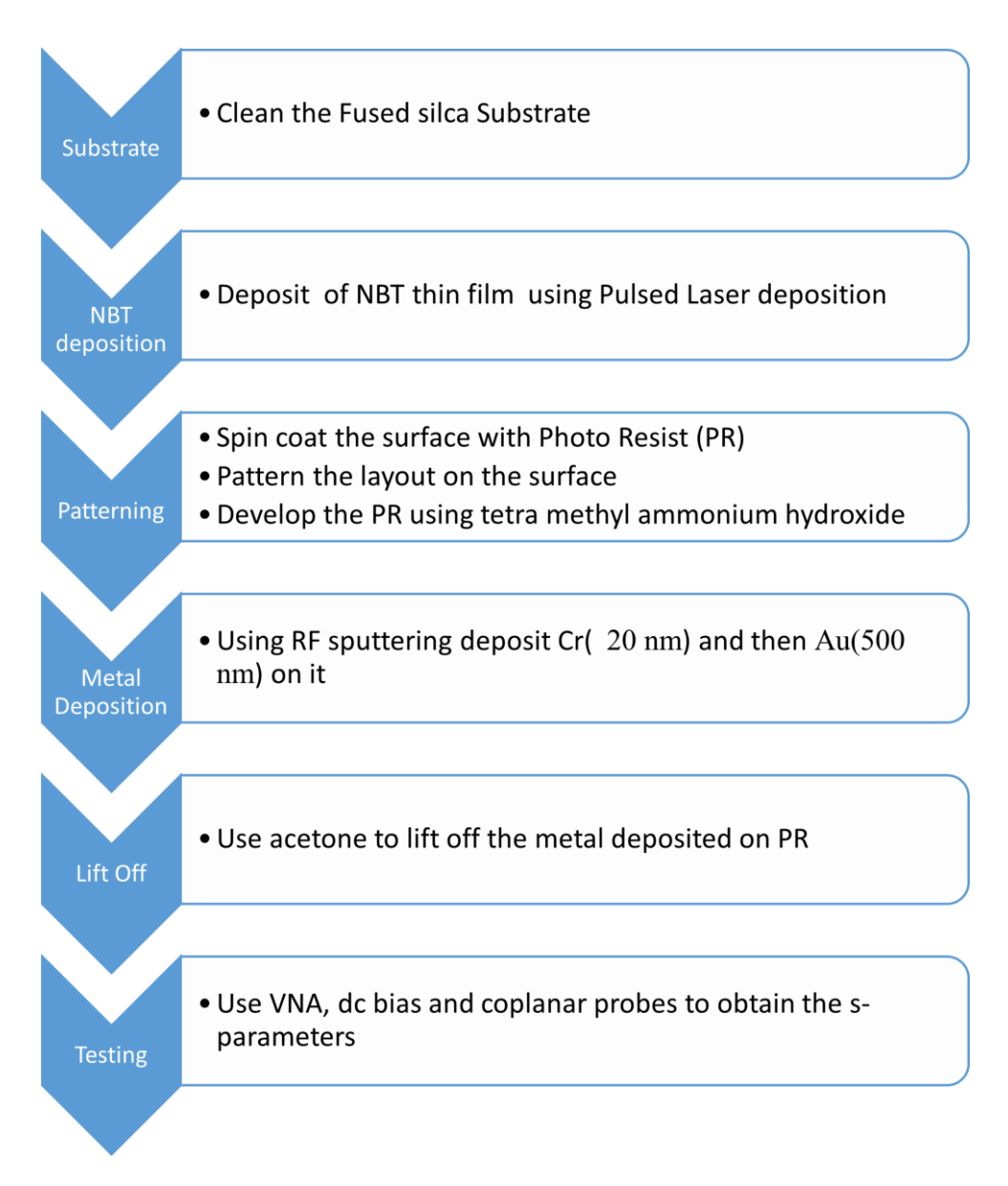


Fig 4.7:Process flow for fabrication and measurement of inter-digitated capacitor

Fujifilm OIR 620-10M (photoresist) is spin coated to the NBT thin film deposited by the PLD method. The spin coater is initially set to a rotational speed of 2000 rpm for 30 seconds followed by 500 rpm for 5 seconds. Then it is baked in hot plate for 20 min at 85°C. UV radiation of 365 nm is exposed through the Mask aligner (model MJB4 of Karl Suss) on the photoresist coated NBT thin film for 5s at a power density of 280 W/m². After exposure, postbaking is done for two minutes at 85°C and developed by Tetramethylammonium hydroxide (TMAH).

Deposition of top electrode and lift-off process

In optimized conditions, electrode deposition is then carried out in RF sputtering system. Initially, a thin layer of chromium (20 nm) is deposited, followed by deposition of Gold (Au) o(150 nm) electrode. The schematic of the RF sputtering system is shown in Figure 4.8.

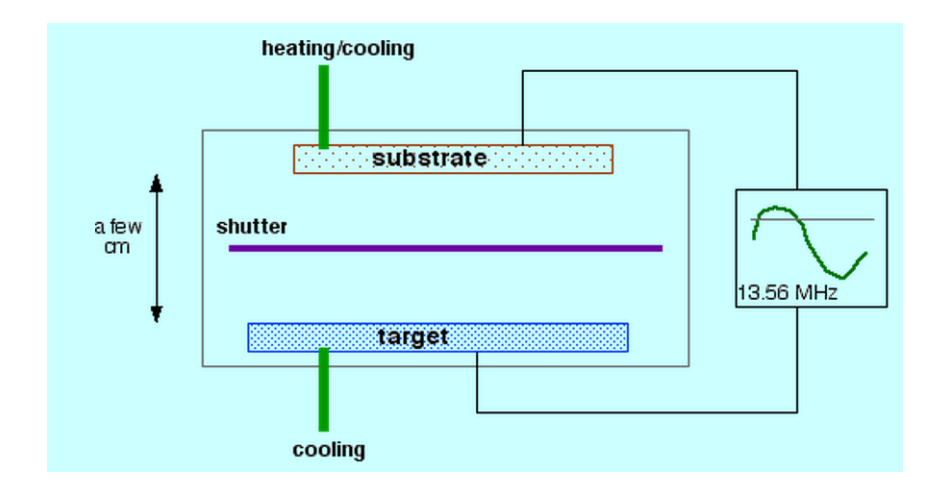


Fig 4.8: Sputtering system

The lift-off process is carried out using acetone, which removes the excess metal on top of the photoresist film. This is followed by a thorough cleaning of the sample under running water and subsequent drying before measurement.

4.5.3 Measurement of permittivity and tunability

Microwave measurements are performed using an on-wafer probe station from J micro technology, a coplanar wave guide probes of pitch 250µm and an Agilent E8361C network

analyzer. DC bias voltage of 0V-70 V at a current of 0.03 mA is used to measure the tunability. The bias tee is a 3 port device with two inputs namely DC supply, RF signal and an output which combines the DC and RF signals and will be applied to the DUT (Device Under Test) at Port 1. The bias tee has a DC Block which protects the VNA by blocking DC voltage from entering VNA. S₁₁ is measured for frequency range of 0.5GHz to 3GHz for different DC voltages. A schematic representation of the measurement set up is shown in Fig 4.9.

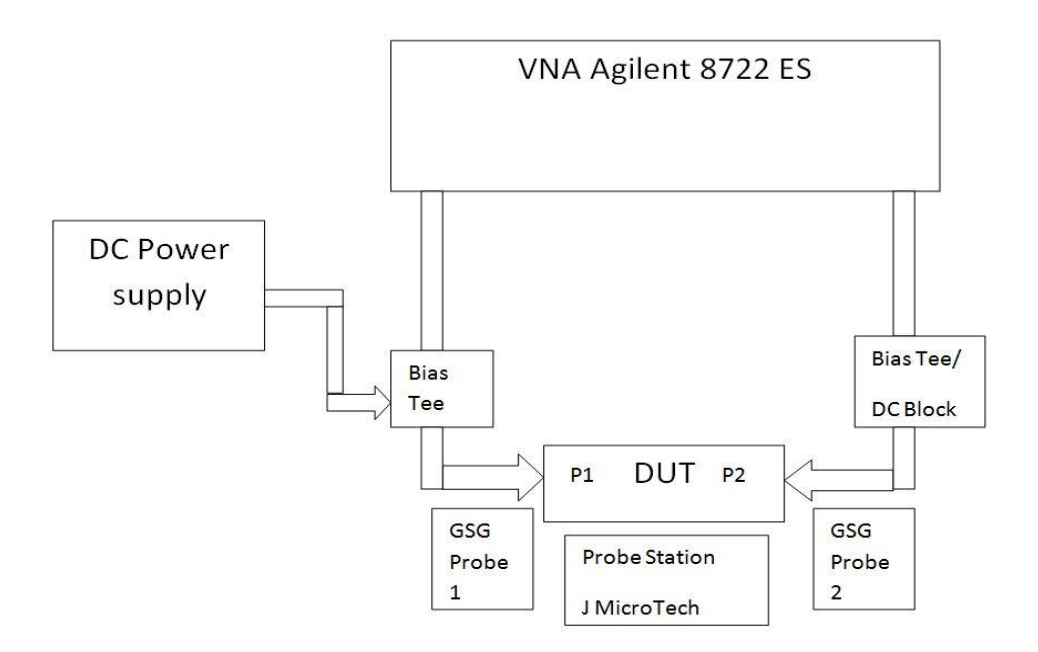


Fig 4.9: VNA based IDC measurement system.

Calibration of VNA

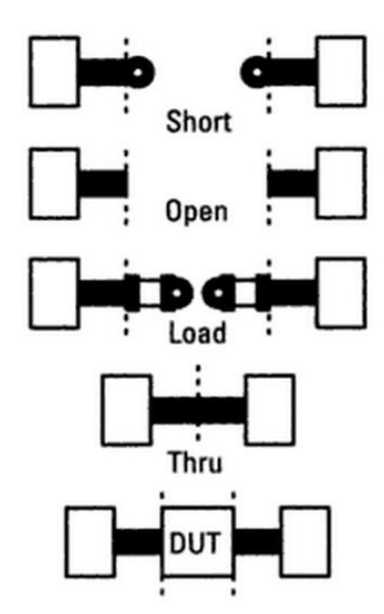


Fig 4.10: SOLT Standards (Dotted Lines indicate Calibrated Reference Planes)

The VNA has to be calibrated before measurement to avoid systematic errors stemming from match, directivity and frequency response. Isolation gives a measure of energy leaking between test and reference channels while directivity depicts how well the forward and reflected signals are separated by VNA couplers. Source match and load match give the quality of termination in source and load paths. Calibration corrects those using error model computation followed by vector correction. SOLT (Short, Open, Load, Thru) and TRL (Thru, Reflect, Line) are two

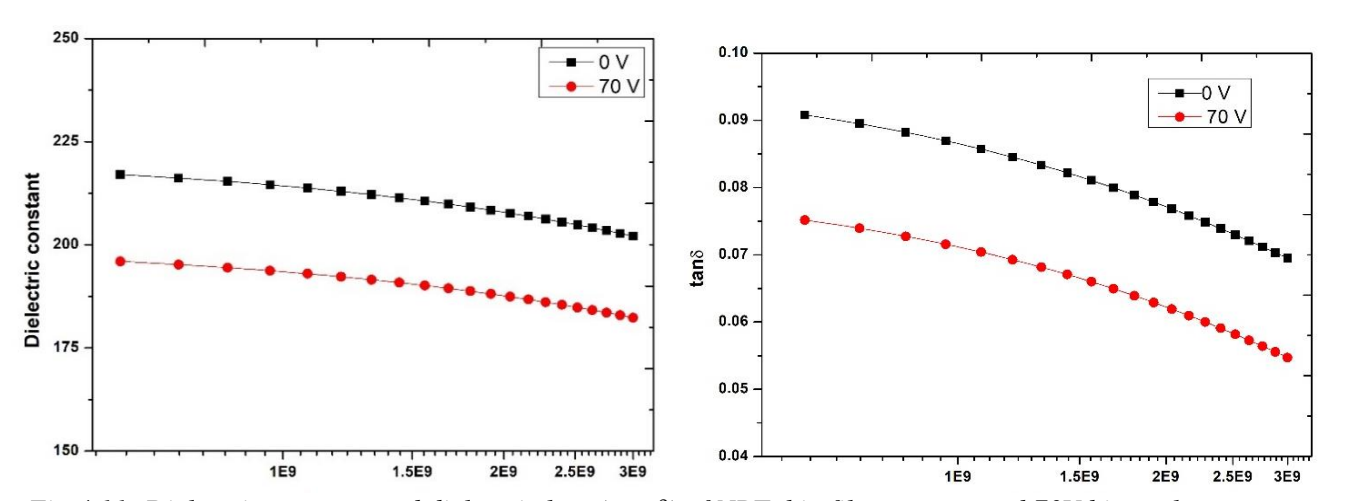


Fig 4.11: Dielectric constant and dielectric loss (tan §) of NBT thin films at zero and 70V bias voltage measured from 0.5 GHz to 3 GHz using IDC.

commonly used calibration standards. Here we used one port SOL calibration. The on-wafer probing standards are portrayed in Fig 4.10. The measurement results are presented in Fig 4.11.

The dielectric constant of films at 1 GHz is around 220 and dielectric loss around 0.8 which are slightly higher than the SPDR measured values at 10 GHz. The higher loss may be attributed to the metallic loss of the electrode because of smaller electrode thickness, the loss tangent is also higher. The change in permittivity/capacitance with on external DC bias is characterized by a parameter called dielectric tunability, defined as the ratio of the dielectric constant value at zero applied electric field to its value at a specific non-zero applied electric field and is known as relative tunability (T_r)

$$T_r = \frac{\mathcal{E}(0) - \mathcal{E}(V)}{\mathcal{E}(0)} \times 100 \tag{4.8}$$

Figure 4.11 shows the dielectric characteristics of NBT thin film at microwave frequencies for various DC bias voltages. The measured value of the dielectric constant reduces with an increasing bias field. The tunability of the NBT at 1 GHz is found to be 9.8 % for a DC bias voltage of 70V. The computed results of dielectric constant and loss are similar to that reported in literature earlier by other methods [19].

The dielectric constant remains almost constant over the measured frequency range, which is rather unusual for a ferroelectric film but is of great advantage for device applications. The dielectric loss also follows the same pattern. These results highlight the importance of investigating the microwave dielectric characteristics of ferroelectric thin films in the polar phase for designing microwave tunable devices. Further investigation in this area will help better understand the loss mechanism in dielectric thin films.

4.6 Ferroelectric properties

The ferroelectric hysteresis loop measured at room temperature for various voltages ranging from 5V to 20 V is shown in Fig. 4.13. The remnant polarisation (Pr) goes up to $12~\mu\text{C/cm}^2$. The coercive field in the positive and negative sides of the loop was slightly different. This variation is observed in similar material systems and stem from two factors. (i) Preferred orientation of FE domain due to stress generated during heat treatment. (ii) Defect complex generated local electric field. The strong coercive field in NBT may have resulted from the differently sized and randomly oriented grains resulting in wider grain boundaries and voids. The obtained values are comparable with P-E loop characteristics obtained by Zhou et al. and Tang et al. [20-23].

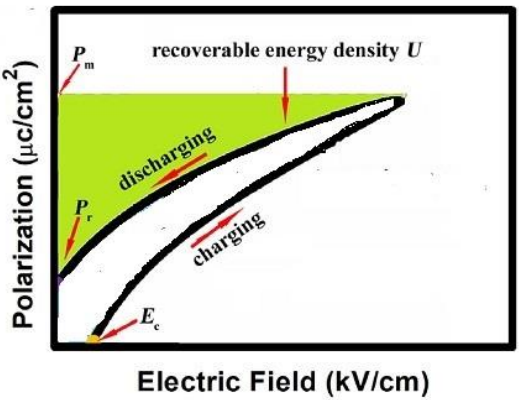


Fig 4.12: Schematic of stored and recoverable energy density from P-E loop.

Energy-storage capacitors are crucial in pulse power circuits, which produce significant amounts of electrical energy in a very short time (ultrashort discharge time). High energy-storage density capacitors with reduced volume, weight, and cost are required to fulfil the need for advances in microelectronics technologies. In Fig 4.12 the green shaded region represents the recoverable energy density (U) and is given by

$$U = \int_{P_r}^{P_s} E \ dP \tag{4.9}$$

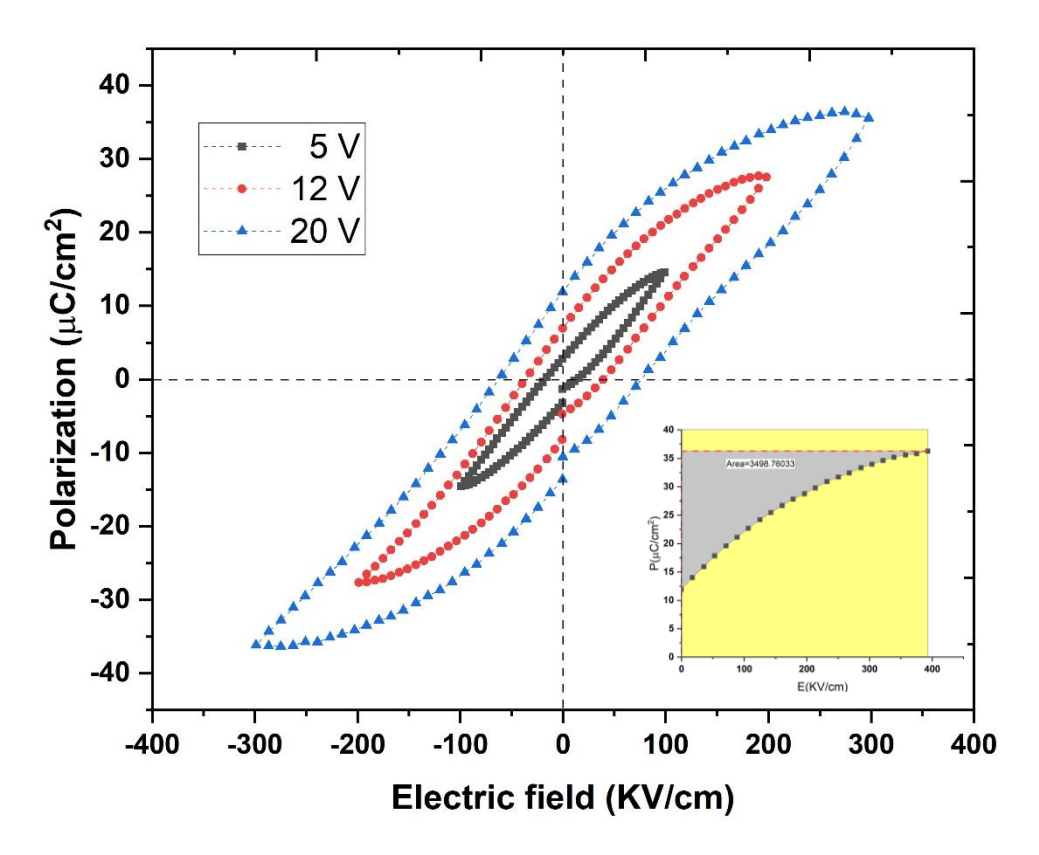


Fig 4.13: Room temperature ferroelectric hysteresis loops measured for NBT thin film at various voltages measured at 1KHz

Here E is the applied electric field, P is the polarization, P_s is Saturation polarization (or maximum polarization) and P_r is the remnant polarization. The substantial difference between the remnant and saturation polarization of the hysteresis curve indicates the suitability of NBT for energy storage applications. The calculation of yield gives a recoverable energy density of 3.5 J/cm³. This is slightly better than the energy density(U) of 2 J/cm³ obtained by Le Zhang et al on alumina substrate via screen-printing for NBT thin films [20]. The parameter of interest for engineering applications is energy storage efficiency(η), given by:

$$\eta = \frac{U}{U + U_{loss}} \tag{4.10}$$

Where U_{loss} energy loss is estimated by integrating the area of the hysteresis loop. In the present study, the value of efficiency obtained is 39 %, which is rather low compared to the currently used lead-based system (70%) but it is lead free [24].

4.7 Conclusion

NBT thin film was grown on fused silica substrates as well as on pt-coated sapphire to study the electrical characteristics of NBT thin films by PLD technique at elevated temperatures. The lattice parameter and phase of thin films are well-matched with standards. Interdigitated capacitor is fabricated on these films and room temperature dielectric constant and tunability are measured. The amorphous films show a low dielectric constant, which gradually increases as the deposition temperature increases. Temperature-dependent impedance data is fitted to an equivalent circuit model. Cole-Cole plot of NBT thin films from 50°C and 150°C shows only one depressed semicircle indicating a single major contribution from grain interior. Above 150°C grain, boundary contribution dominates and significantly increases with temperature. At microwave frequencies dielectric constant of NBT thin films shows only negligible dispersion and exhibits good tunability. These results indicate that NBT may be considered an alternative to Ba_{0.5}Sr_{0.5}TiO₃ for tunable microwave devices. The energy storage characteristics of NBT films are estimated from the P-E loop. The NBT films shows reasonable storage performance and with further optimization, they may replace the lead-based ferroelectric systems in pulsed-discharge and power conditioning electronic applications.

4.8 Reference

- [1] S. S. Gevorgian and E. L. Kollberg, IEEE. Trans. Microw. Theory. Tech. 49, 2117-2124 (2001).
- [2] G. Subramanyam, C. Chen and S. Dey, Integr. Ferroelectr. 77, 189-197 (2005).
- [3] J. P. Goud, S. Ramakanth, A. Joseph, K. Sandeep, G. L. Rao and K.C. J. Raju, Thin Solid Films, 626, 126-130 (2017).
- [4] J. Nath, D. Ghosh, J. P. Maria, A. I. Kingon, W. Fathelbab, P. D. Franzon, and M. B. Steer, IEEE Trans. MTT 53, 2707 (2005).
- [5] B. Acikel, T. R. Taylor, P. J. Hansen, J. S. Speck and R. A. York, IEEE Microw. Wirel. Compon. Lett. 12, 237 (2002).
- [6] D. Kuylenstierna, A. Vorobiev, P. Linner, and S. Gevorgian, IEEE Trans. Microw. Theory Tech. 53, 2164 (2005).
- [7] G. Subramanyam, M. W. Cole, Nian X. Sun, et al. J. Appl. Phys. 114, 191301 (2013).
- [8] D. Dimos, M. Raymond, R. Schwartz and C.H. Mueller, J. Electroceramics. 1, 145–153 (1997).
- [9]H. N. AL. Shareef, D. Dimos, M. V. Raymond, R. W. Schwartz and C. H. Mueller, J. Electroceramics. 1:2, 145 (1997).
- [10]G. Velu, J. C. Carru, E. Cattan, D. Remiens, X. Melique and D. Lippens, Ferroelectrics. 288, 59 (2003).
- [11] Y. Zhao, X. Hao and M. Li, J. Alloys Compd. 601, 112 (2014).
- [12] S. Pattipaka, A.R. James and P. Dobbidi, J. Alloys Compd. 765, 1195 (2018).

- [13] A.S. Daryapurkar, J. T. Kolte, P. R. Apte, P. Gopalan, Ceram. Int. 40, 2441 (2014).
- [14] T. van Dijk and A. J. Burggraaf, Phys. Stat. Sol. (a) 63, 229–240 (1981).
- [15] M. J. Verkerk, B. J. Middlehuis, and A. J. Burggraaf, Solid State Ionics 6, 159–170 (1982).
- [16] H. Cesiulis, N. Tsyntsaru, A. Ramanavicius, and G. Ragoisha, NanoScience and Technology; Tiginyanu, I., Topala, P., Ursaki, V., Eds.; Springer: Cham, Switzerland, 3–42 (2016).
- [17] S. P. Gevorgian, T. Martinsson, P. L. J. Linnkr and E. L. Kollberg, IEEE Trans. Microw. Theory. Tech. 44, 6 (1996).
- [18] N. Dib, J. Ababneh and A. Omar, Int. J. RF Microw. Comput. Aided Eng. 15, 551-559 (2005).
- [19] A. Joseph, J. P.Goud, S. R. Emani and K. C. J. Raju. AIP Conference Proceedings 1731, 080039 (2016).
- [20] L. Zhang, X.H. Hao, L.W. Zhang, J. C. Yang and S. L. An, J. Mater. Sci. Mater. Electron. 24, 3830–3835 (2013).
- [21] X. G. Tang, J. Wang, X. X. Wang and H. L.W. Chan, Chem. Mater. 16, 5293 (2004).
- [22] S. Pattipaka, A. Joseph, G. P. Bharti, K. C. J. Raju, A. Khare and D. Pamu, Appl. Surf. Sci. 488, 391-403 (2019).
- [23] Z. H. Zhou, J. M. Xue, W. Z. Li, J. Wang, H. Zhu and J. M. Miao, J. Phys. D: Appl. Phys. 38, 642 (2005).
- [24] H. Jung, J. Lim, M. Peddigari, J. Ryu, D. Choi and D. Jeong, J. Eur. Ceram. Soc. 40, 63–70 (2020).

Chapter-5

Effect of microwave annealing and laser fluence on NBT thin films

5.1 Introduction

The physical properties exhibited by ferroelectric thin films are influenced by deposition and annealing conditions. These differences mainly stem from the structural, morphological and compositional variations in the films. In the first part of the chapter, we investigate the role of microwave annealing method in determining the physical characteristics of NBT thin films. In the subsequent section, the role of laser fluence on the physical properties of deposited thin films is discussed.

5.2 Microwave annealing of NBT thin films

The ferroelectric thin films were often annealed in-situ or ex-situ in conventional or rapid thermal methods to obtain proper crystallization and electrical properties [1,2]. In the past, microwave annealing (MWA) is used in semiconductor processing for such processes as dopant activation and silicide formation in NiSi_{1-x}Ge_x, InGaZnO-based transistors, graphene oxide reduction and in various organic syntheses [3-8]. In conventional thermal processing, the material is heated from outward to inward by the temperature gradient created and most of the energy is wasted to heat the outside volume. But in microwave annealing, energy is generated inside the material by matter-radiation interaction. This leads to certain advantages such as a shorter heating cycle, uniform heat profile, reduced thermal budget, targeted area heating etc.

5.2.1 Experimental Procedure

In this study, microwave annealing of NBT thin films are performed in a multimode (applicator) microwave furnace with 1.3 KW power and 2.45 GHz operational frequency. The hybrid heating method was employed to obtain rapid uniform heating. In the hybrid heating method, the sample is heated by a conventional method using a microwave susceptor followed by the self-microwave absorption of the sample beyond critical temperature. This chapter investigates the effects of microwave annealing temperature on the structural, microstructural,

optical and dielectric characteristics of post-annealed NBT films. The detailed deposition conditions of amorphous NBT thin films are tabulated in Table 5.1. These films are further exsitu annealed in microwave furnaces for 20 min at various substrate temperatures (500°C-600°C) to form crystalline films.

Parameter	
Laser wavelength	248 nm
Laser shot frequency	5 Hz
Laser fluence	2 J/cm ²
Base pressure	6 x 10 ⁻⁶ mbar
Working pressure	3 x 10 ⁻² mbar
Substrate temperature	300°C
Annealing temperature	500°C - 600°C
Number of shots	6000

Table 5. 2: Deposition conditions of amorphous NBT thin films

5.2.2 Structural characterization

The grazing angle X-ray diffraction is carried out for NBT thin films that are post-annealed at 500°C, 525°C, 550°C and 600°C for 20 min and is presented in fig 5.1. The formation of phase with the R3c space group is confirmed by comparing it with the JCPDF card (number 04-012-5540). The crystallite sizes of the films are calculated using the Debye-Scherrer relation [9],

$$L = \frac{0.9\lambda}{\beta \cos \theta} \tag{5.1}$$

Where L is the crystallite size and λ is the wavelength of K_{α} source used in GI-XRD and θ is the angle of diffraction and β denotes the full width at half maximum. The increase in the intensity of prominent (110) peak and the emergence of (220) peak reveals that the crystalline quality is improved at higher deposition temperatures.

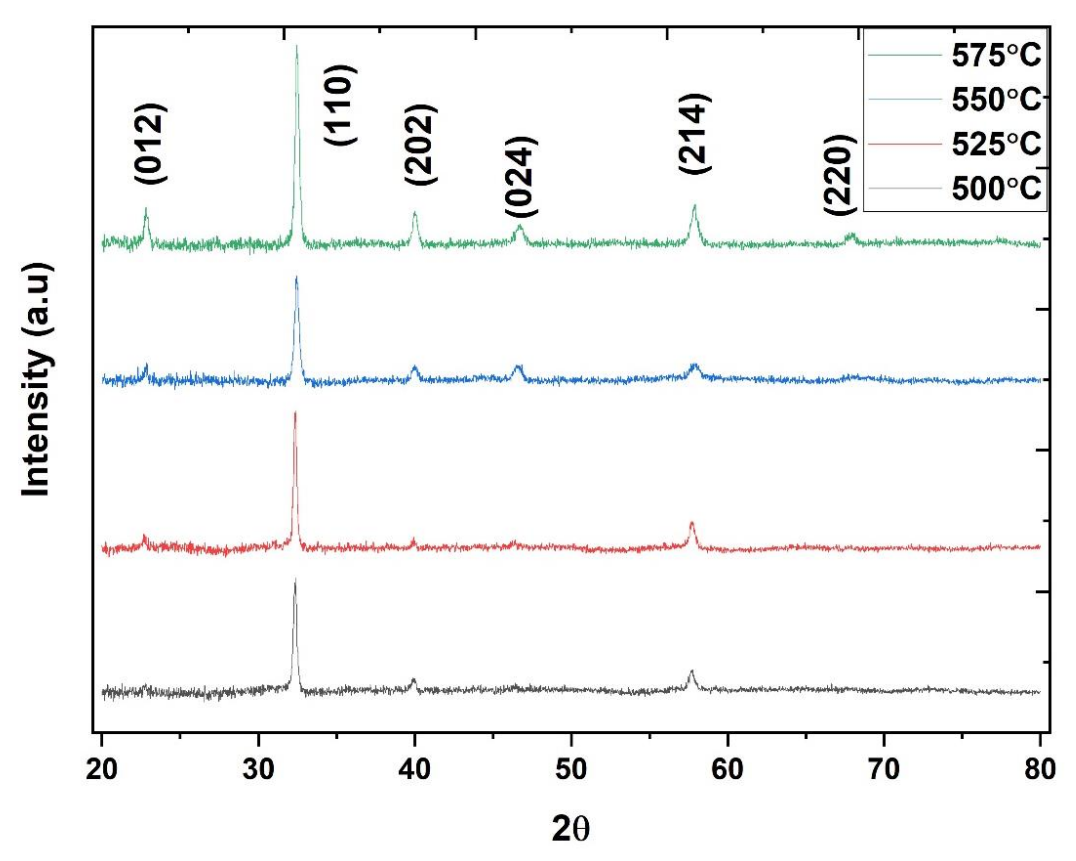


Fig 5. 1: XRD of NBT thin films annealed in microwave furnace at various temperatures

The crystallite size is determined by fitting the major (110) peak to the pseudo-Voigt function to obtain the diffraction angle and FWHM and substituting it in eq (5.1). With increase in the annealing temperature, computed crystallite size also increases from 23nm to 28nm as depicted in fig 5.2.

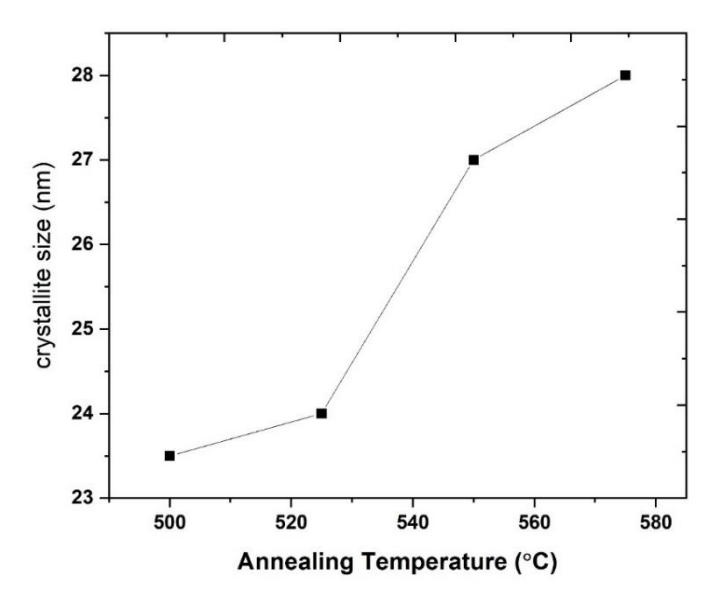


Fig 5. 2: Variation of crystallite size in NBT thin films with annealing temperature.

The inverse square of crystallite size is called dislocation density, a parameter used to quantify the amount of dislocation in a unit volume of the material. Since the crystallite size monotonically increases with temperature, dislocation density decrease with a rise in annealing temperature. The dislocation is reduced at higher annealing temperatures because of the enhanced diffusion rate and higher internal energy available for the dislocation motion [10].

5.2.3 Optical properties

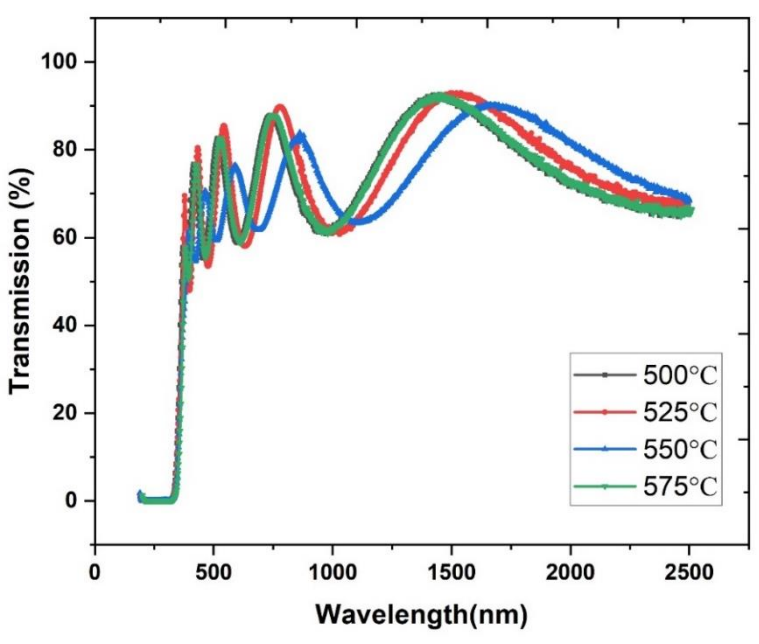


Fig 5. 3: Transmission spectra of NBT films annealed at different temperatures in a microwave furnace.

The optical spectra of NBT films annealed in the microwave furnace at various temperatures are presented in Fig 5.3. The spectra contain three different types of regions viz, (1) high transmittance oscillating region, (2) low transmittance region around 500nm and (3) strong absorption region (< 300nm). Multiple reflections from the film and substrate interface cause the Fabry-Pérot interference in the first region. The envelop method proposed by Swanepoel is utilized to extract the dielectric properties of the films [11]. The refractive index obtained by this method is fitted to the oscillator model (Fig 5.4) to calculate the oscillator parameter such as oscillator peak energy, dispersion energy, etc.

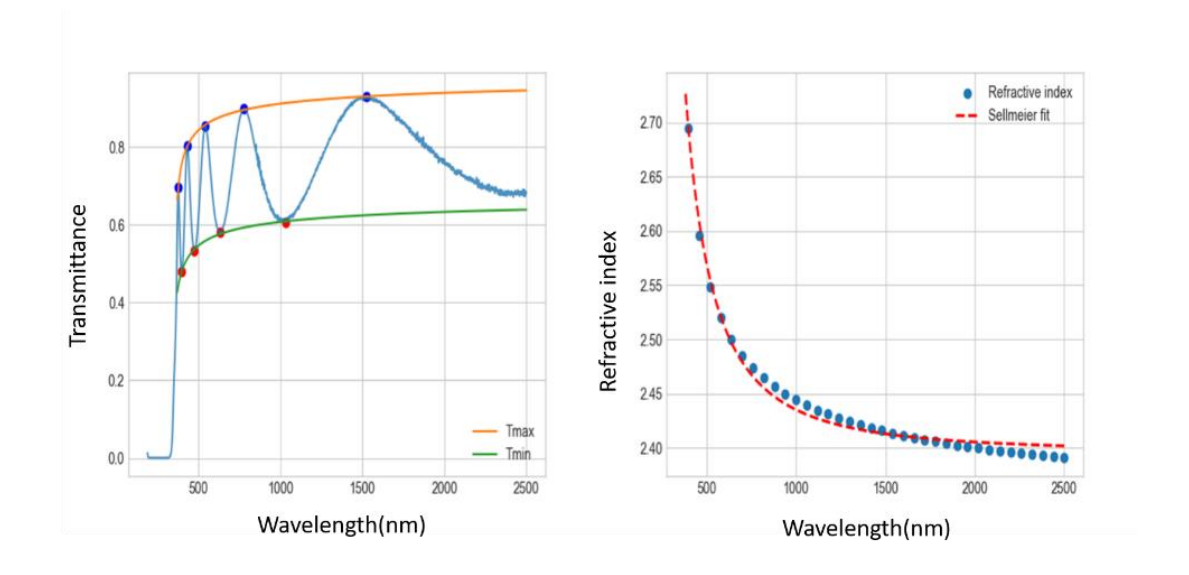


Fig 5. 4: (a) Envelop fit (b) Sellmeier fit for NBT film annealed at 525 °C.

The refractive index and estimated band gap at long wavelength limit of NBT thin films annealed at different temperatures are depicted in Fig 5.5. The band gap shows a red shift with an increase in annealing temperature, which is a common behaviour of FE oxides [12-14]. The extent of structural disorder present in the film strongly influences the refractive index of the thin films. Higher temperature near the crystallization threshold provides more energy to particle diffusion and hence often leads to improved packing density and, thus, the refractive

index, as evident from Fig 5.5. Interestingly, near the onset of crystallization, the band gap values show a remarkable difference above which it is nearly constant. The refractive index in the transmission region is fitted to Wemple–DiDomenico model represented by equation (5.2)

$$n^2 - 1 = \frac{E_0 E_d}{E_g^2 - E^2} \tag{5.2}$$

The dispersion energy (E_d) is a measure of the average probability (strength) of the inter-band transition. The dispersion energy for 500°C annealed film is 25.64eV, which rapidly grows to 28.48eV for 525°C annealed film. The dispersion energy is a linear function of the anion valency and coordination number of the nearest neighbour cation. Hence increase in the dispersion energy and consequent higher absorption may be the result of the increased oxygen vacancies at higher temperatures.

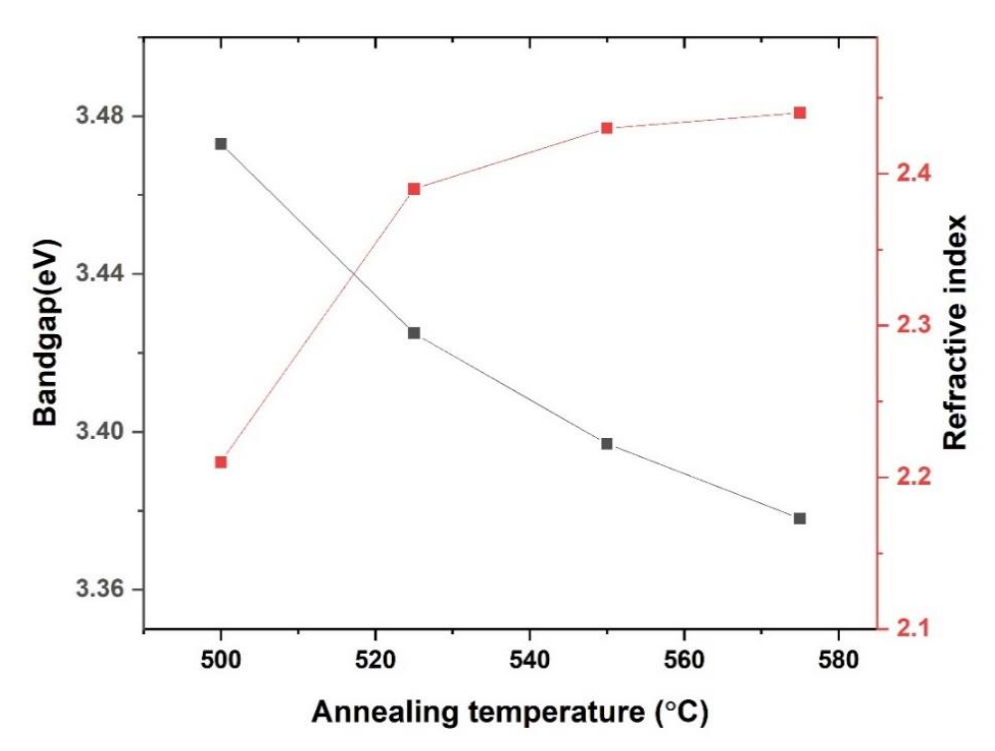


Fig 5. 5: Refractive index and band gap of NBT thin films annealed at various temperatures with microwaves.

5.2.4 Comparison of conventional and microwave ex-situ annealed samples

In this section, we compare the NBT thin films annealed at 550°C for 60 minutes in a conventional furnace and 20 minutes in a microwave furnace. The morphological and microwave frequency dielectric characteristics of both films were studied.

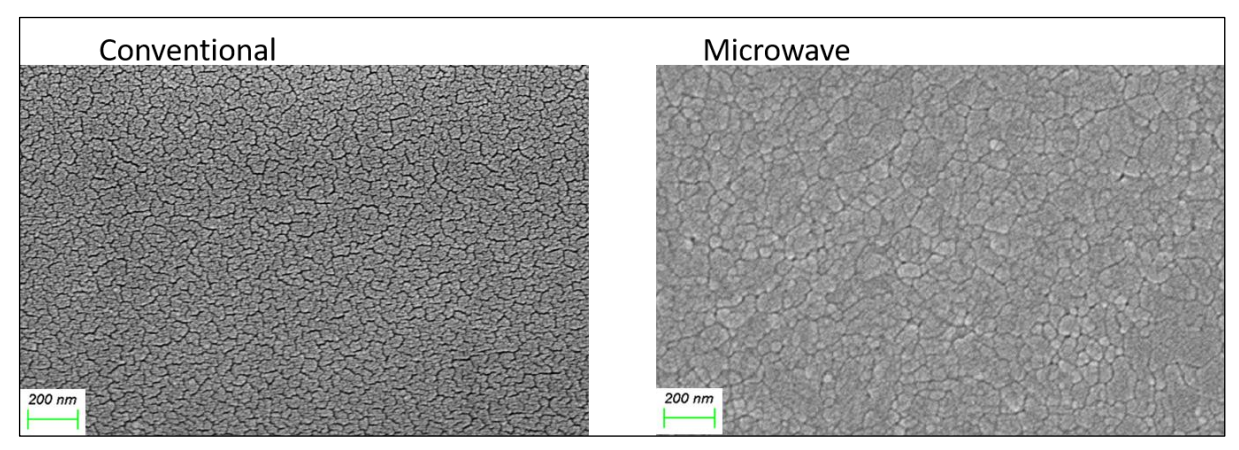


Fig 5.6: Shows the FE-SEM image of NBT thin films ex-situ annealed in (left) conventional and (right) microwave furnaces.

FE-SEM image of the conventional furnace annealed films shows a very small grainy surface structure, almost similar to the amorphous phase. On the other hand, the microwave furnace annealed films show clear grain formation (Fig5.6). The average grain size is found to be 40 ± 5 nm. The microwave frequency dielectric characteristics of both films are measured by the SPDR technique at 10 GHz. The microwave furnace annealed films show a dielectric constant of 177 and tan8 of 0.032, whereas conventional annealed films show a dielectric constant of 178 and a loss of 0.041. Apart from a bit higher loss in microwave dielectric characteristics of both films are identical. The increase in dielectric loss may stem from a trace amount of Bi rich in the secondary phase since these thin films were deposited from 2wt% excess bismuth added target, which gave a pure single phase in case of in-situ annealing. The lower annealing time used in the case of microwave annealing considerably reduces the chance of bismuth

volatilization. Hence microwave furnace annealing of NBT thin films is a more energy-efficient and effective means of obtaining high-quality NBT thin films compared to conventional ex-situ annealing for prolonged temperatures with comparable physical properties.

5.3 Effect of laser fluence

PLD is a good thin film deposition method for the depositing oxide thin films. NBT thin film deposition involves two volatile components. Hence, investigating each component's role is crucial to obtaining high-quality thin films. It is clear from Chapter 3 and numerous other studies that there exists only a narrow window of temperature and pressure in which single-phase device quality NBT thin films could be grown. The chamber parameters such as substrate temperature, background oxygen pressure, target substrate distance and laser parameters like laser fluence and pulse repetition rate determine the kinematics of plasma, which determine the deposited films' stoichiometry, microstructure and physical properties [15-17].

Laser fluence decides the quantity of ablated material and thus the deposition rate, characteristic of the plume and deposited film. The rate of deposition and hence the thickness of the deposited film varies with laser fluence. Some of the physical properties of thin films show a dependence on the film thickness. Hence in the present study, the substrate temperature and pressure were fixed to the one used in chapter 4 and varied the number of laser shots to keep the thickness the same (within ± 20 nm).

5.3.1 Structural characterization

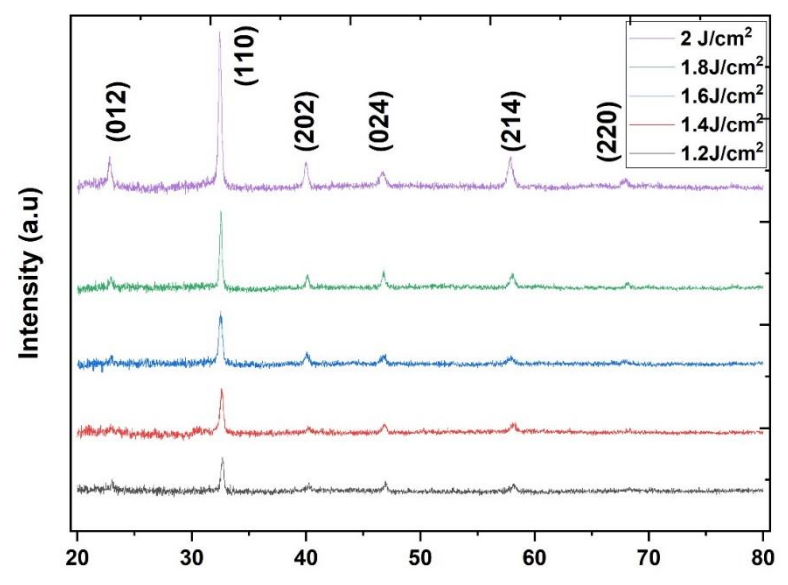


Fig 5. 7: XRD of NBT films deposited at different laser fluences

The XRD of NBT thin films deposited at different laser energy densities (fluences), starting from 1.2J/cm² to 2J/cm², is shown in Fig 5.7. It is evident from the XRD that all the films are crystalized in a single phase.

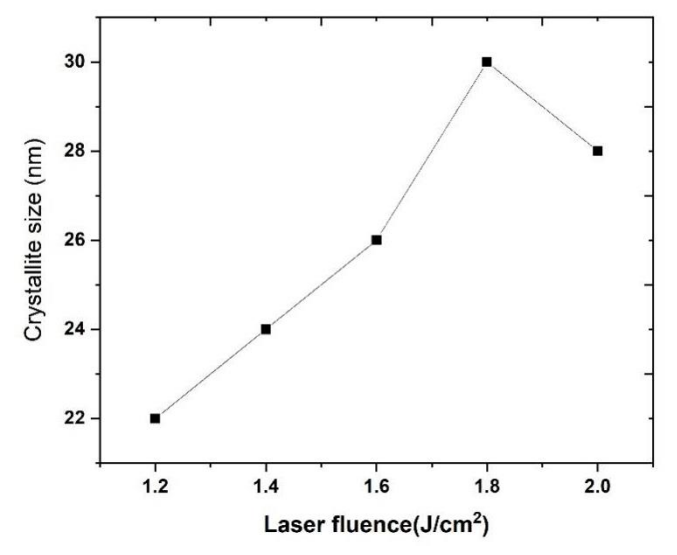


Fig 5. 8: Variation of crystallite size in NBT thin films with laser fluence.

Even though the intensity of the (110) peak keeps increasing with laser fluence, the crystallite size initially follows the trend but drops slightly after 1.8 J/cm² as shown in Fig 5.8.

5.3.2 FE-SEM and EDX

The microstructural features of NBT thin films deposited at various fluences show a very peculiar nature as depicited in Fig 5.9.

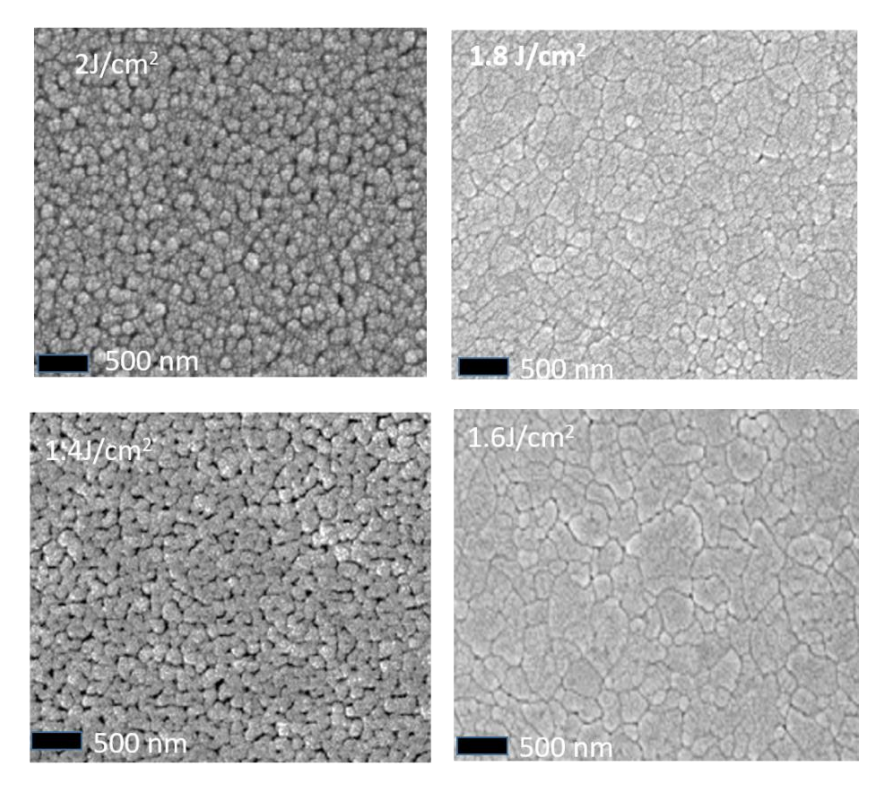


Fig 5. 9: The FE-SEM image of NBT thin films deposited at various laser fluences starting from 1.4 J/cm^2

Initially, grain size increases with laser fluence, but once the laser fluence is increased from 1.6 J/cm^2 to 1.8 J/cm^2 , the grain size reduces from $400\pm30\text{nm}$ to around $250\pm20\text{nm}$, followed by a further reduction in grain size below 100nm for 2J/cm^2 . In order to identify the compositional changes in the NBT thin films deposited by various laser fluences, Energy Dispersive X-ray (EDX) available as an accessory of the FE-SEM setup was used. Table 5.2 list the relative cation percentage in the NBT thin films deposited at different laser fluence (Fig 5.10).

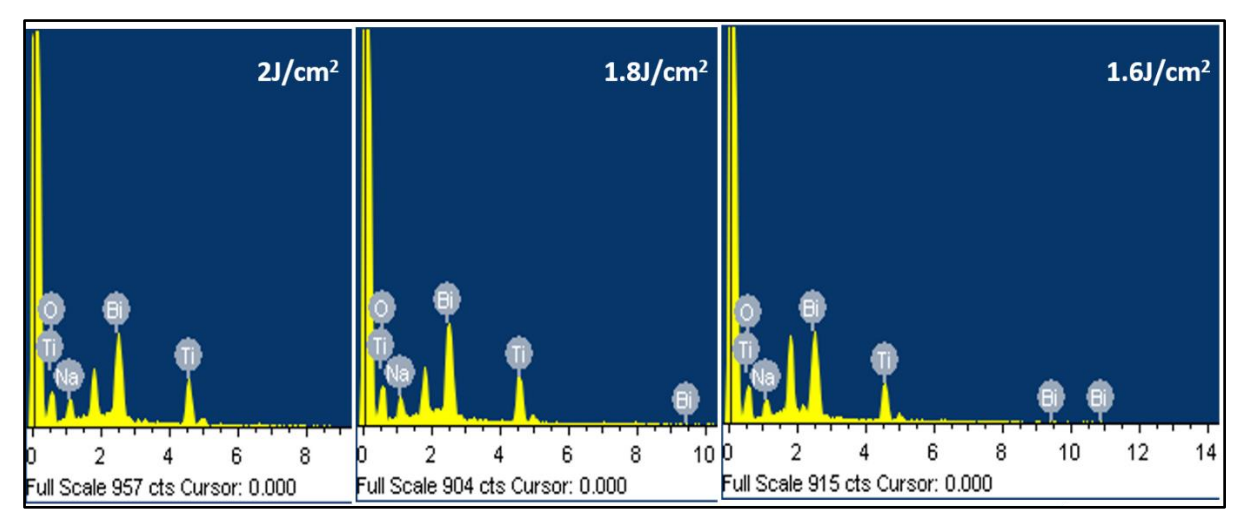


Fig 5. 10: EDX of NBT thin films deposited at various laser fluence (2J/cm² to 1.6 J/cm²)

The compositions of all the films were estimated using EDX measurement around ten random positions in each film. The estimated cation ratios of all the films are close to the stoichiometric composition. Even though we cannot unambiguously identify the compositional variations due to the accuracy limitation of EDX, a nominal but systematic increase of Bi content with laser fluence could be observed. Nazir Jaber et al. investigated the role of laser fluence on the deposition of BiFeO₃ and observed a similar Bi vacancy at a low laser fluence regime [18]. Unlike crystallite size, the decrease in grain size with an increase in fluence may be understood in terms of this cation vacancy. The A site non-stoichiometry in NBT ceramics is known to exhibit a similar trend in grain size [19-21]. The grain of NBT ceramic studied by Linhao Li et al. [22] noticed a decrease of grain size from $10 \mu m$ to 100 nm for a Bi composition variation from x=-0.01 to x=+0.01 in NBT represented by (Na_{0.5}Bi_{0.5+x}) TiO₃. The oxygen vacancies generated because of the Bi deficiency and their high ionic mobility lead to higher diffusion rates which result in larger grains [19].

Laser Fluence	Na (at%)	Bi(at%)	Ti(at%)
2 J/cm ²	24.75	25.41	49.84
1.8 J/cm ²	25.02	25.18	49.80
1.6 J/cm ²	25.18	24.88	49.94
1.4 J/cm ²	25.51	24.51	49.98

Table 5. 3: Cation atomic percentage of NBT thin films deposited at a different laser fluence

5.3.3 Optical Properties

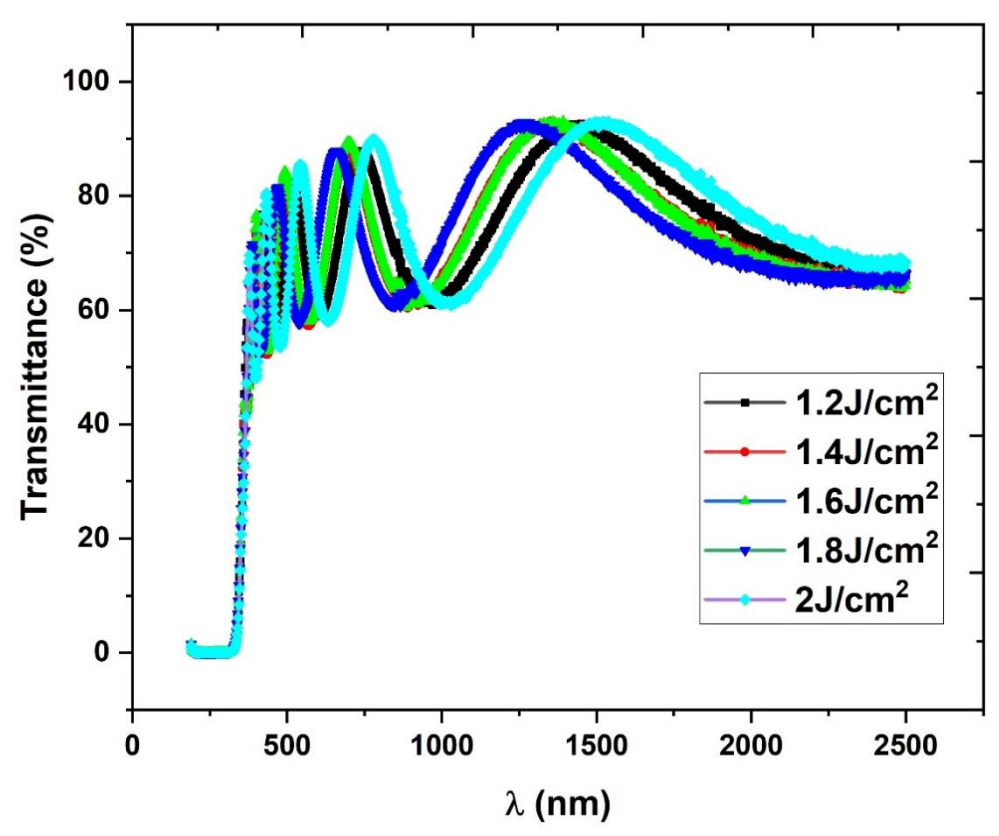


Fig 5. 11: Variation in optical transmittance with laser fluence.

Fig 5.11 displays the measured transmission spectra for NBT thin films deposited with different laser fluences. In NIR and visible regimes of the spectrum all the films show high transmittance but display sharp absorption edges around 350nm. With a closer look at the absorption region, we may understand that the laser fluence variation does not greatly influence the absorption region.

The refractive index is determined by the envelope method described in the previous chapter.

The refractive index is fitted to Wemple–DiDomenico model represented by equation (5.2)

$$n^2 - 1 = \frac{E_0 E_d}{E_g^2 - E^2} \tag{5.2}$$

Here the energy of incoming radiation is represented by E, peak oscillator energy by E_0 , and dispersion energy by E_d , respectively. Unlike the band gap (E_g), the refractive index and the dispersion energy show a noticeable dependence on the laser energy density used for the deposition of films. The refractive index of thin films depends on the packing density, polarizability, microstructure, and crystallinity. Here we observed a decrease in grain size at higher fluence, hinting at a reduced packing density at the high fluence range [23,24]. The relation connecting the film's packing density and refractive index is given by equation (5.3)

$$P = \left[\frac{n_f^2 - 1}{n_f^2 + 2}\right] \left[\frac{n_b^2 + 2}{n_{fb}^2 - 1}\right]$$
 (5.3)

Here n_f and n_b are the refractive indices of the thin film and the bulk sample respectively. The dependence of refractive index at IR frequencies and the band gap on the laser energy density used to deposit the NBT thin film are plotted in fig 5.12.

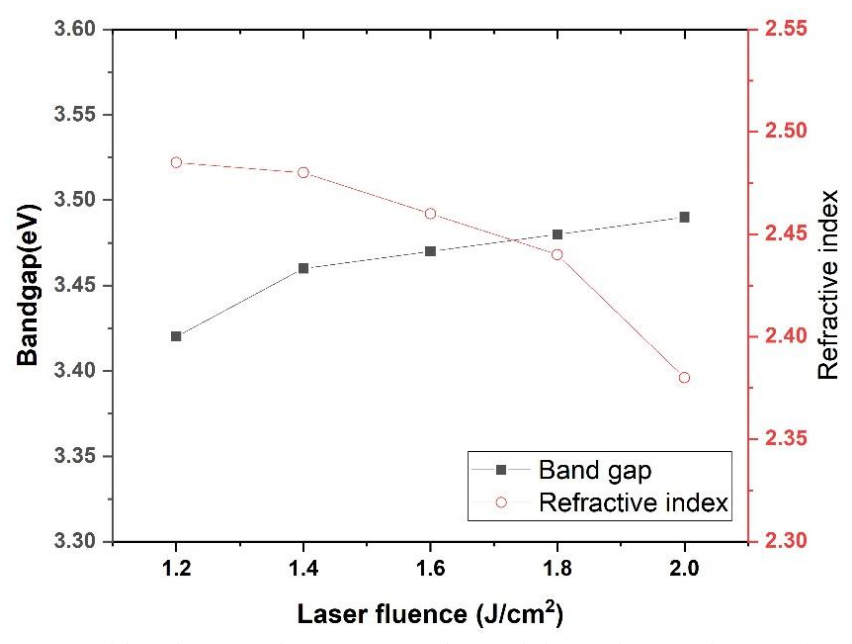


Fig 5. 12: Optical band gap and refractive index with laser fluence during film deposition.

It is worth noticing that the grain size from FE-SEM, refractive index and oscillator peak energy show similar dependence on the laser fluence. All these parameters decrease with increasing laser fluence. Hence the effect of laser fluence on physical properties may be correlated with compositional changes in the A-site and the rate of deposition, resulting in a change of microstructure and packing density which in turn modify the refractive index, dielectric loss and oscillator parameters. The low-frequency dielectric properties of Bi deficient films also show similar behaviour as reported by Ming Li et al in reference [19].

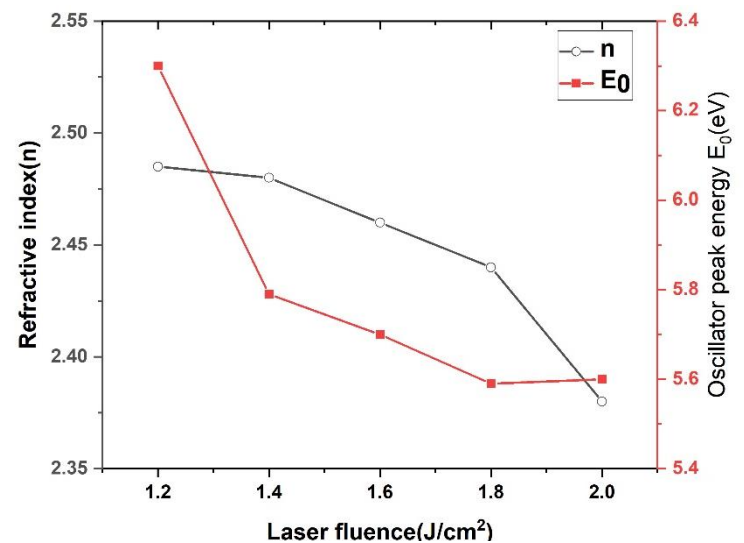


Fig 5. 13: Variation of Oscillator peak energy and refractive index with laser fluence during film deposition.

Even though we did not find a substantial change in the band gap with fluence, the refractive index and oscillator peak energy vary across the films deposited at different laser fluences. It is evident from fig 5.13 that NBT thin films exhibit a positive correlation of oscillator peak energy and refractive index with fluence. This is rather unusual as most of the semiconductors and insulators show an inverse correlation between the refractive index and oscillator peak energy [25]. Since the band gaps of all the films are nearly the same, the observed disparity originates from strong grain size or composition dependence of the dispersion energy. The dispersion energy almost linearly decreases from 26.6eV to 23.7eV, similar to the refractive index variation.

5.3.4 Microwave dielectric properties

The deposition of high-quality ferroelectric thin films is accelerated due to their distinct application in microwave devices. These research efforts require accurate and repeatable measurements of the dielectric characteristics of these films at microwave frequencies. Even though the microwave frequency dielectric characteristics of these films are important from both an application and academic standpoint, there aren't many studies on the subject. Utilizing SPDR techniques, the dielectric constant and loss tangent of the thin films prepared at different laser fluences are performed at an X-band spot frequency of 10GHz. The detailed measurement procedure is described in Chapter 3. Fig 5.14 depicts the dielectric constant and loss decrease with increasing laser fluence and the values are considerably lowest for films deposited at 2 J/cm². The decrease in dielectric properties may be because of the reduction in the grain size and oxygen vacancies at higher laser fluence.

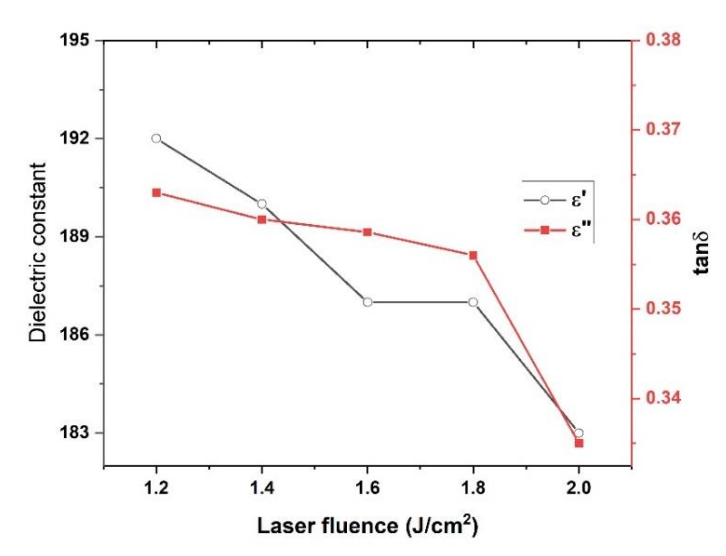


Fig 5. 14: Microwave frequency dielectric constant and loss with laser fluence during

5.4 Conclusion

This chapter investigates the role of annealing method and laser energy density used to deposit the thin films on their physical properties. The onset of crystallization temperature of NBT thin films is considerably lower in microwave furnace annealing than in conventional furnace annealing. The moderate heating rate and uniformity in heating are the primary reasons for the reduction in the low processing temperature of microwave-annealed films. The film annealed below 500°C are amorphous and films annealed above 500°C show a rhombohedral crystalline phase with an R3c space group at room temperature. An increment in the value of annealing temperature enhances the crystalline quality of the films, which is evident from the increase in crystallite size and refractive index.

The effect of laser energy density during thin film deposition on structural, microstructural, compositional and physical properties is investigated for NBT thin films. Even though XRD shows a single phase for all the films deposited in the investigated fluence range, the compositional analysis confirms the presence of lower bismuth content films in the lower fluence range. The NBT thin films with correct stoichiometry are obtained for films deposited at 2J/cm². The refractive index and microwave dielectric constant decreases with an increase in the laser fluence. This may also be associated with the differences in the bismuth stoichiometry obtained at higher laser fluence.

5.5 Reference

- [1] W. Weinreich, A. Shariq, K. Seidel, J. Sundqvist, A. Paskaleva, M. Lemberger and A. J. Bauer, J. Vac.Sci. Technol. B. 31, 01A109 (2013).
- [2] B. Zhao, Y. Yan, J. Bi, G. Xu, Y. Xu, X. Yang, L. Fan and M. Liu, Nanomaterials. 12, 3001, (2022).
- [3] Z. Zhao, N. D. Theodore, R. N. P. Vemuri, S. Das, W. Lu, S. S. Lau and T. L. Alford, Appl. Phys. Lett. 103, 192103 (2013).
- [4] P. Xu, C. Fu, C. Hu, D. W. Zhang, D. Wu, J. Luo, C. Zhao, Z. Zhang and S. L. Zhang, Appl. Phys. Lett. 102, 122114 (2013).
- [5] S. C. Fong, C. Y. Wang, T. H. Chang and T. S. Chin, Appl. Phys. Lett. 94, 102104 (2009).
- [6] C. Hu, P. Xu, C. Fu, Z. Zhu, X. Gao, A. Jamshidi, M. Noroozi, H. Radamson, D. Wu and S. L. Zhang, Appl. Phys. Lett. 101, 092101 (2012).
- [7] C. Wen, N. Zhao, D. W. Zhang, D. Wu, Z. B. Zhang and S. L. Zhang, Synthetic Met. 194, 71 (2014).
- [8] Fu, Chaochao, et al., AIP Advances 7.3: 035214(2017).
- [9] P. Scherrer, Nachr. Ges. Wiss. Göttingen 26, 98-100 (1918).
- [10] N. Birbilis, K. D. Ralston, S. Virtanen, H. L. Fraser, and C. H. J. Davies, Corros. Eng. Sci. Technol. 45, 224-230 (2010).
- [11] R. Swanepoel, J. Phys. E: Sci. Instrum. 16, 1214 (1983).
- [12] J. P. Goud, A. Kumar, K. Sandeep, S. Ramakanth, P. Ghoshal, and K. C. J. Raju, Adv. Electron. Mater. 7, 2000905 (2021).
- [13] Z. G. Hu and P. Hess, Appl. Phys. Lett. 89, 081906 (2006).
- [14] Z. G. Hu, Y. W. Li, F. Y. Yue and Z. Q. Zhu, Appl. Phys. Lett. 91, 221903 (2007).
- [15] A.S. Daryapurkar, J.T. Kolte and P. Gopalan, Thin Solid Films 579, 44-49 (2015).
- [16] Y. Zhang, Q. Yan, F. Yang, Y. Xu and L. Liu, Ceram. Int. 42. 12672–12674 (2016).
- [17] S. Amorusoa, C. Aruta, P. Aurinoa, R. Bruzzesea, X. Wang, F. Miletto, U. Granozio and Scotti di Uccio, Appl. Surf. Sci. 258, 9116–9122 (2012).
- [18] N. Jaber, J. Wolfman, C. Daumont, B. Negulescu, A. Ruyter, T. Sauvage, B. Courtois, H. Bouyanfif, J. L. Longuet, C. A. Lambert and F. Gervais, Thin Solid Films, 634, 107-111 (2017).
- [19] M. Li, H. Zhang, S. N. Cook, L. Li, J. A. Kilner, I. M. Reaney and D. C. Sinclair, Chem. Mater, 27, 629 (2015).
- [20] Y. S. Sung, J. M. Kim, J. H. Cho, T. K. Song, M. H. Kim and T. G. Park, Appl. Phys. Lett. 98, 012902 (2011).
- [21] B. Santhosh kumar, K. R. Priolkar, S. Pollastri, D. Oliveira de Souza, I. Carlomagno, A. K. Bera, S. M. Yusuf and B. Pahari, J. Phy. Chem. C, 125, 19621-19630 (2021).
- [22] L. Li, Oxide ion conduction in A-site Bi-containing perovskite-type ceramics, PhD thesis, University of Sheffield (2016).
- [23] P.Li, JF McDonald and TM. LU, J. Appl. Phys. 71, 5596 (1992).
- [24] G. Bauer, Ann. Phys, 19, 434 (1934).
- [25] D. J. Chadi and M. L. Cohen, Phys. Lett. 49A, 381 (1974).

Chapter 6 Laser Induced crystallization of NBT thin films

6.1 Introduction

The application of ferroelectric oxides in the industry is greatly limited by these materials' very high crystallization temperatures. Ferroelectric oxide exhibits unique physical properties, increased stability in harsh environments, and hence they got abundant device potential. Crystallising these films at a temperature compatible with on-chip integration will bring rapid technological advancement. Conventional methods like metal-induced crystallization in the glass and semiconductor industry and rapid thermal annealing often deteriorate the quality of the film. Reduction in temperature achieved in those methods are often inadequate to be applied in the flexible or semiconductor industry. Laser-annealing of perovskite films suitable for solar cells and local crystallization of ferromagnetic layer in spintronic and biomedical devices are other related emerging areas in laser crystallization. [1-6]

Currently, laser-induced crystallization is being applied in many areas of science and technology but understanding its mechanism is still in its infancy. The classical nucleation model (Johnson -Mehl-Avrami- Kolmogorov (JMAK)) is often used to investigate the crystallization behaviour of materials but that cannot be applied directly to the non-isothermal laser annealing process. However, the change in Gibbs free energy and the basic understanding of nucleation and growth barrier and other understanding is quite helpful.

In this chapter, an Excimer laser-based crystallization of NBT films is carried out at room temperature. Laser parameters are optimized to get high-quality NBT thin films and the understanding obtained from these parameters and the available theories of laser annealing are discussed.

6.2 Laser-induced crystallization mechanism

6.2.1 Laser annealing as a non-isothermal process.

Instantaneous crystallization of the surface and subsurface region of a selected area of the sample is feasible with laser annealing treatment. When the laser is irradiated on the sample, the materials in the regions of laser material interaction volume quickly absorb the energy and cool down quickly with rates in the order of 10° °C s⁻¹. Because of this very fast heating and cooling cycle, the crystallization characteristics of these non-isothermal laser annealing may differ from conventional isothermal annealing. As a result, the classical theory of crystal nucleation, which works well for equilibrium kinetics, fails to model the crystallization behaviour during laser annealing processing, which frequently occurs near or completely non-equilibrium thermal circumstances. In general, the onset of crystallization temperature moves to a higher one in a dynamic (non-isothermal) treatment [7-9]. This may be understood by the Ozawa equation

$$ln(H_{\rm R}) = \frac{-E_{\rm cryst}}{RT_{\rm cryst}} + B$$
(6.1)

 H_{R} . represent rate of heating, E_{cryst} and RT_{cryst} are the activation energy and the onset temperature of crystallization, respectively, and B is a constant. This calculation is performed for various materials systems [10,11] and the results indicate that the onset of crystallization and subsequent growth of crystallites in laser annealing compared to isothermal annealing.

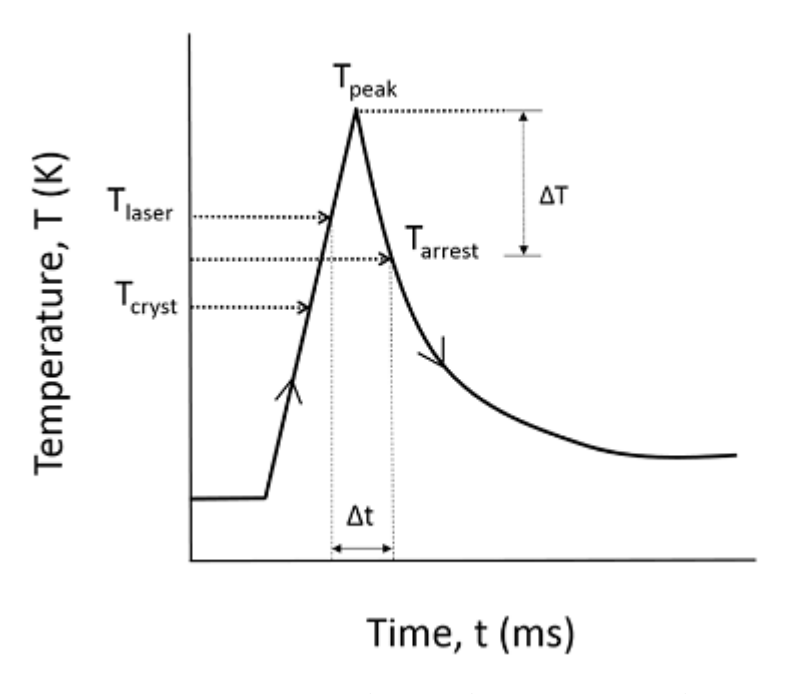


Fig 6. 1: Time-temperature curve of showing dynamic nature of laser processing.[10]

In isothermal heating cycles, the crystallization of an amorphous material begins at the crystallization onset temperature and the formation of crystallites continues during the heating or cooling process until the sample temperature returns to the crystallization onset temperature. During the non-isothermal heating cycles, the temperature rises to the maximum temperature after laser irradiation follows rapid cooling cycle after the termination of laser pulse. However, throughout the cooling cycle, crystallite formation continues until it is abruptly stopped (arrested) at the temperature of T_{arrest} because of the insufficient energy available to overcome the nucleation and growth barrier (Fig 6.1). Dynamic non-isothermal laser heating typically produces incredibly high heating and cooling rates, which significantly reduce the time interval of crystallite growth. The maximum temperature and cooling rate are influenced by laser fluence, repetition rate and the wavelength of the laser used. Thus, the laser process parameters had a significant impact on crystallization.

6.2.2 Transient Pressure Mechanism for Femtosecond Laser annealing

Pei Hsing et al. applied molecular dynamics and the continuum two-temperature model to the laser annealing process to predict the temperature evolution inside the material. This model considers the role of both electrons and lattices via an electron-phonon coupling mechanism. According to this lattice mending model, the energy of the laser beam is transferred to the electron subsystem in a few hundred femtoseconds, and energy is transferred to the lattice in a few picoseconds (<15ps) by electron-phonon coupling. The K.E of the shock waves generated by laser irradiation is diminished by non-reflecting boundaries, and energy equilibrium is between electron and lattice in achieved over 15ps as shown in fig 6.2. [12-14]

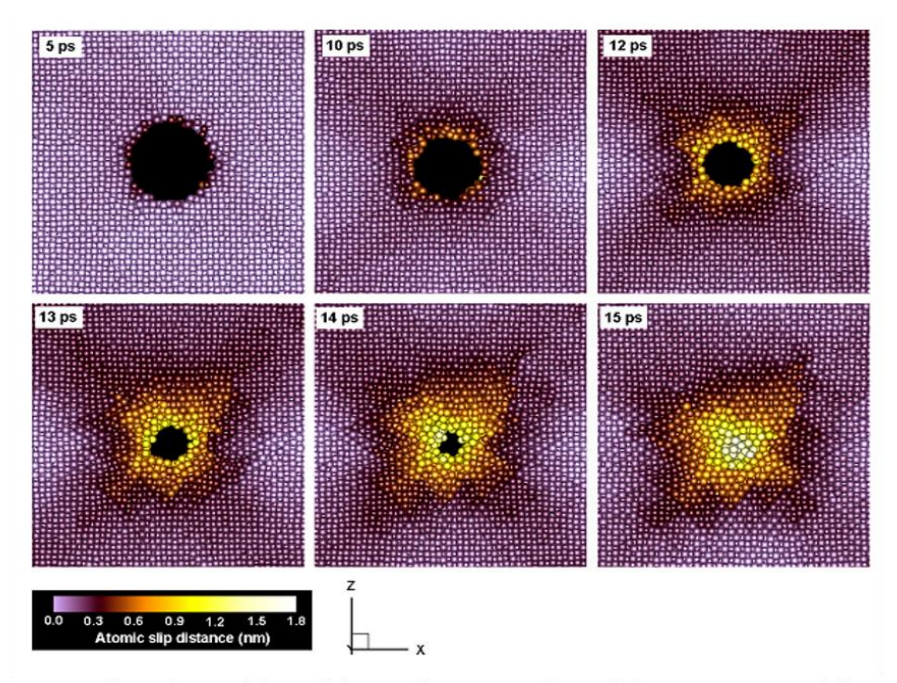


Fig 6. 2: Snapshots of the solid-state lattice mending of the nanopore at different progression times by an annealing fluence of 0.89Fth melt (Fth melt- is the fluence required to melt the sample)[5]

Pei Hsing et al. classified lattice mending process into three phases. In the first phase, lattice mending commences by surface nucleation of dislocation of the pore around time t = 5.0ps. In the next phase, the shock wave generated from the temperature gradient induces shear stress on the pore leading to atomic plane sliding(slips) at t = 10ps. This crucial cross-slip mode

through solid state mending mechanism quickly repairs the nanopore completely at around t= 14 ps. The shock wave amplitude is calculated using Viral theory using the momentum flux of atomic movements and intermolecular force. The maximum pressure experienced by the pore is -7 GPa and it occurs at t= 9ps. In the last stage, lattice recovery and reconstruction occur. They also estimated the lattice mending rate and found that shockwave driven mending rate is 10^4 times of the classical non-equilibrium atomic diffusion rate.

6.3 Experimental work

6.3.1 Deposition of amorphous NBT thin films

In laser parameter optimization experiments, amorphous NBT thin films were deposited on fused silica substrate at a substrate temperature of 300° C. The substrates were loaded 5 cm away from the target. In order to deposit the NBT films, the PLD chamber was first evacuated to a pressure of 6×10^{-6} mbar and afterward, oxygen has been introduced to the chamber, obtaining the required working pressure of 3×10^{-2} mbar. This constant pressure is maintained throughout depositions at a laser fluence of 2J/cm^2 . Post deposition, the thin films were in situ annealed at the same temperature for 20 min in the presence of oxygen. The thickness of the film is measured using a profilometer and found it to be 200nm.

6.3.2 Laser annealing of NBT thin films

The effect of laser parameters such as the number of pulses, energy density and thin film deposition conditions like deposition pressure and laser fluence during the deposition of amorphous NBT are investigated in this chapter. The laser annealing of these films is carried out at room temperature using the same KrF Excimer laser.

6.4 Effects of the number of laser shots

The deposited films are annealed by various number of laser shots starting from 10 to 20,000 shots. Films annealed above 10,000 shots are X-ray crystalline (Fig 6.4) though samples

discusses the effectiveness of optical microscopy and Raman spectral analysis in chapter -3 discusses the effectiveness of optical microscopy and Raman spectra to distinguish the crystalline and amorphous phases which are not possible to be detected by XRD. Fig 6.3 shows a few interesting microstructural development changes during laser annealing. It is evident from optical microscopic images that very small grains are formed after irradiating with 1K shots, and the grains are noticeably grown around 10K shots. But even after irradiating with 20K shots, complete surface crystallization does not occur. The corresponding XRD patterns are shown in Fig 6.4. The microwave dielectric permittivity of the amorphous films shows lower values compared to their crystalline counterparts due to the lower packing density in the amorphous phase. This also acts as a measure of the crystallinity developed. The microwave dielectric characteristics of these samples are measured using the cavity perturbation technique because the sample dimensions were small and an accurate determination of dielectric properties is required for proper identification of crystalline quality, which is only possible with resonance-based microwave measurements.

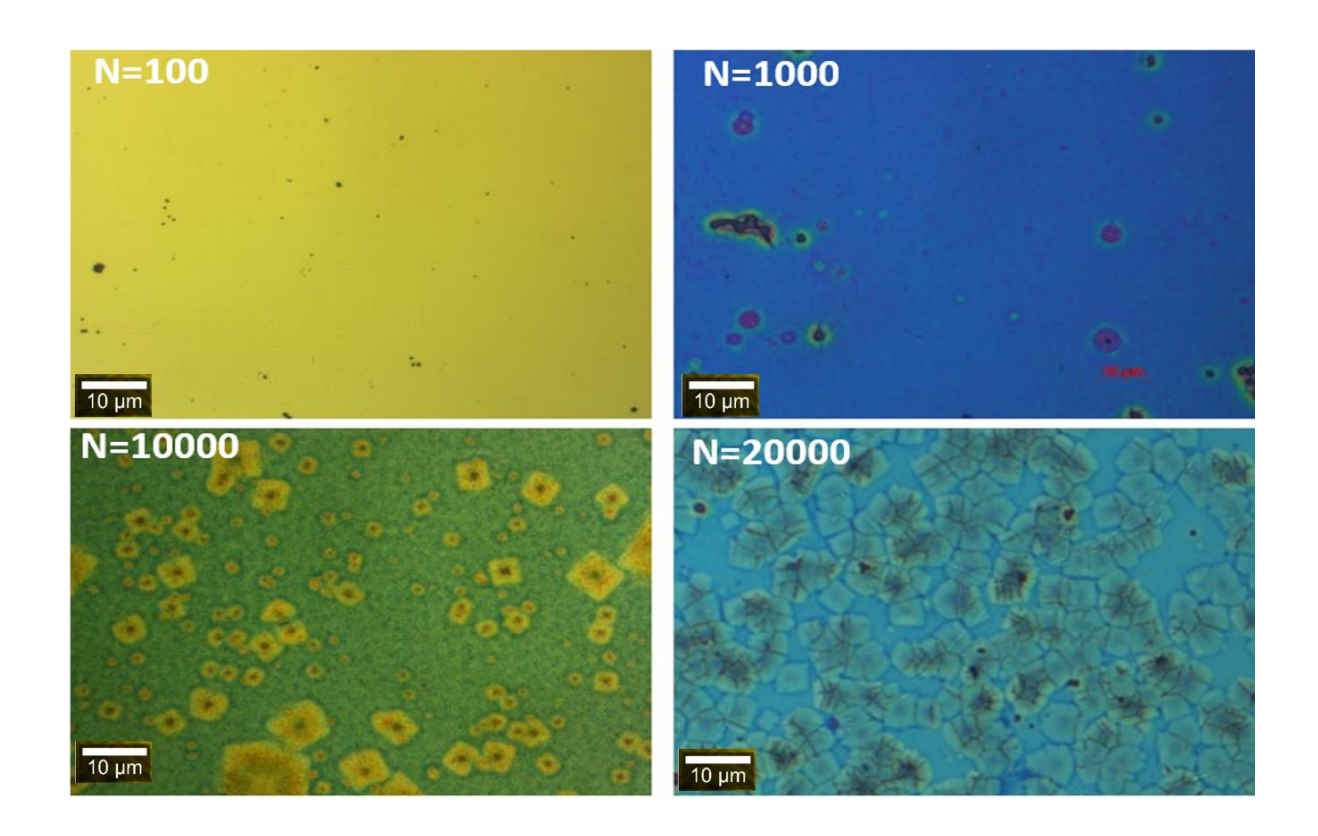


Fig 6.3: Optical images of laser-annealed films for various number of shots. The number of shots increases from top left to bottom right (100 to 20000)

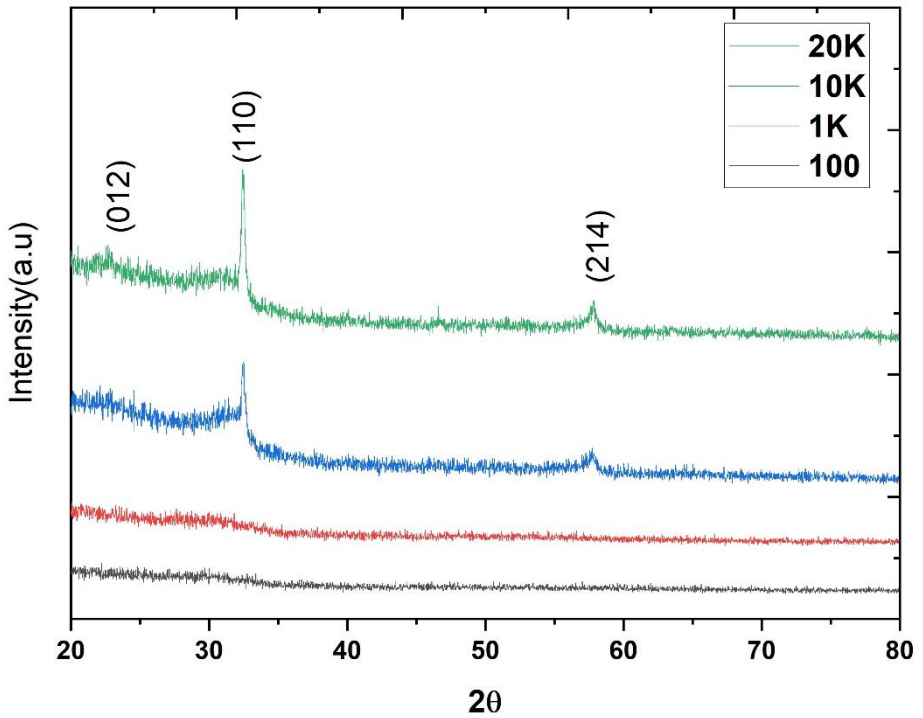


Fig 6.4: XRD of laser crystallized samples irradiated with various numbers of laser shots.

Microwave measurement by cavity perturbation method

Cavity perturbation theory is a general method in physics where the parameters of a complex system are expressed in terms of a standard system which do not differ greatly so that the difference can be treated as a perturbation. The complex permittivity of thin films can also be obtained using this principle. [15]. In the cavity perturbation method, the changes in the resonant frequency and quality factor Q of the resonant cavity after the introduction of the dielectric sample are compared with the corresponding values of the cavity without the sample [7]. The obtained shift in frequency and quality factor after introducing a sample with permittivity \mathcal{E} '- j \mathcal{E} " may be expressed as:

$$\frac{f_1 - f_2}{f_2} = (\varepsilon' - 1) \frac{\int_{V_s} E_1^2 dV}{\int_{V_c} E_1^2 dV}$$
(6.2)

$$\left[\frac{1}{Q_2} - \frac{1}{Q_1}\right] = \varepsilon'' \frac{\int_{V_S} E_1^2 dV}{\int_{V_{c-1}} E_1^2 dV}$$

$$\tag{6.3}$$

where,

$$E_{1} = E_{10} \sin\left(\frac{\pi x}{a}\right) \sin\left(n\frac{\pi z}{L}\right) \tag{6.4}$$

Here sample and cavity volumes are denoted by V_s and V_c , respectively, and f_1 is the resonance frequency of the empty cavity, f_2 is the resonance frequency of the cavity after the sample is inserted and Q_1 and Q_2 are the corresponding quality factors. The cavity perturbation technique is valid as long as the perturbation is small and does not drastically change the existing electric field distribution.

In order to measure the dielectric properties of thin films, a hole is drilled at the E_{max} position of the TE mode cavity and we treat the substrate as a part of the original cavity with resonance frequency f_1 , and E_1 is the electric field of the modified cavity (cavity with bare substrate) and is considered as the initial field E_1 . This will make the assumption that the dimension of the sample is small compared to the wavelength, which is always true in the case of thin films

coated on this substrate. A similar method is already used by many others to estimate the dielectric properties of liquids/solid and powder forms using a sample holder [15-17]. Now that the film has been inserted the shift in the resonance frequency and quality factor are measured(f_2 and Q_2 respectively). This shift in cavity properties is used to determine the dielectric parameters of the film using eq (6.5) [18]:

$$\varepsilon' = K \frac{L}{t} \frac{\Delta f}{f_1} + 1 \tag{6.5}$$

Here shift in frequency $\Delta f = f_2 - f_1$ where f_1 and f_2 are the resonance frequencies of the cavity with the substrate and the film-coated substrate, respectively and t is the film thickness. The coefficient K represents the fractional area of the sample with respect to the cross-sectional area of the cavity. The dielectric loss of the thin film may be computed by (6.6) as

$$\varepsilon'' = K \frac{L}{2t} \left[\frac{1}{Q_{L1}} - \frac{1}{Q_{L_2}} \right] \tag{6.6}$$

Where Q_{L1} and Q_{L2} represent the cavity's unloaded Q factors with and without the substrate coated with a film, respectively.



Fig 6. 5: WR-90 cavity connected to the VNA

Even though calibration is not necessary for resonance measurement, we perform one port calibration at the co-axial waveguide adaptor surface to improve the shape of the resonance peak. Later WR-90 rectangular waveguide, as shown in fig 6.5, is connected. There are many cavity modes present in the X band, and we used the TE_{107} mode for measurement purposes.

A thoroughly cleaned bare substrate of dimension 5mm x 1.2cm is introduced to the cavity and measured the resonance frequency and the quality factor of this modified cavity. This is followed by measuring the frequency shift and quality factor of the NBT film-coated substrate. The shift in parameters is used to estimate the dielectric properties using Eq 6.5 and 6.6. We measured a set of samples irradiated with the excimer laser with different numbers of pulses and tabulated them in Table 6.1.

Error analysis of dielectric permittivity

The error analysis for the dielectric constant may be carried out using Eq. 6.7.

$$d\varepsilon' = K \frac{\Delta f}{f_{0s}} \frac{1}{\tau} dL + K \frac{L}{\tau} \left[\frac{\Delta f}{f_{0s}} \left(\frac{d\tau}{\tau} + \frac{df_{0s}}{f_{0s}} \right) + \frac{d\Delta f}{f_{0s}} \right]$$
(6.7)

In this case, uncertainty associated with film thickness measurement is highest and all other terms are negligible. Hence we measured thickness accurately using the optical method and verified by profilometer measurement. The sample size is smaller and hence the film thickness obtained are without much variation. The calculated uncertainty for 5 % uncertainty in the thickness measurement is found to be \pm 2%. Similarly, the error analysis of Tan8 is also carried out using Eq 6.8.

$$d\varepsilon'' = \frac{KL}{2\tau} \left[\frac{1}{Q_{Ls}} - \frac{1}{Q_{L0}} \right] \left[\frac{dL}{L} + \frac{d\tau}{\tau} \right] + \frac{KL}{\tau} \frac{dQ_L}{Q_{Ls}}$$
(6.8)

This suggests that the accuracy of measuring the Q factor is the main cause of error in this measurement. Furthermore, there will be considerable inaccuracy in the estimation of the dielectric loss if the Q factor of the empty cavity is too low. Since we are using high Q cavities (~1500) in this case, the Q factor can be precisely determined by the VNA.

Sample/Number of Shots	Microwave dielectric constant	Tan8	Crystallite size (nm)
100	131	0.261	-
1000	138	0.264	-
5000	139	0.267	-
10000	155	0.310	26.1
20000	158	0.317	27.4

Table 6. 1: Microwave dielectric properties of NBT thin films annealed with different numbers of annealing shots.

The Raman spectra of NBT thin films laser annealed for 5 K shots are shown in Fig 6.6. The amorphous and crystalline regions in the thin films are evident in optical images and confirmed by Raman spectroscopy. This shows that films are only partially crystallized even after irradiation with a large number of shots.

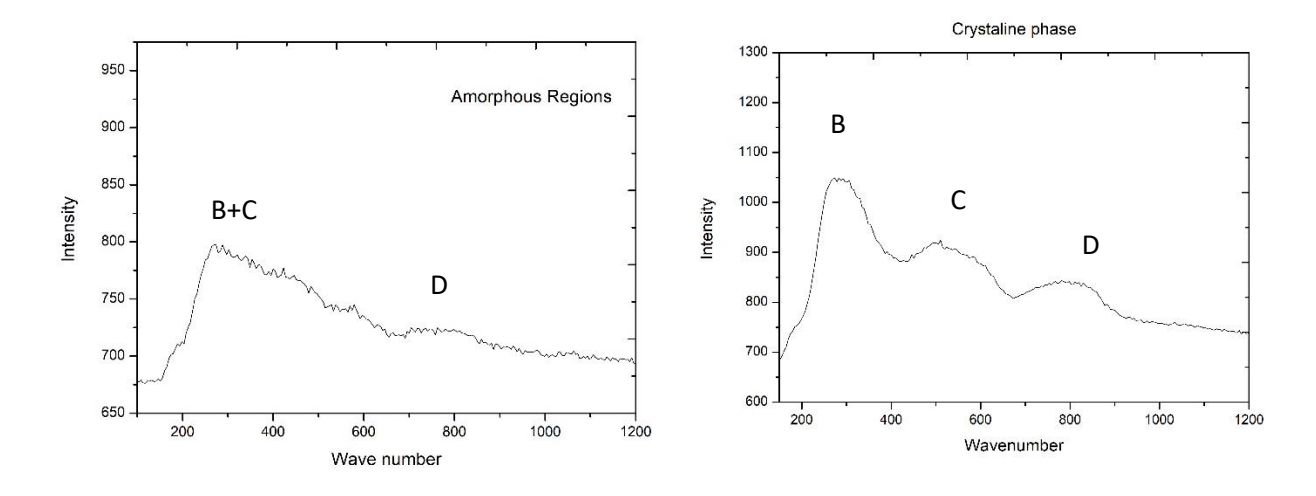


Fig 6. 6: Raman spectra of NBT thin films laser annealed for 5 K shots (left) Spectra collected from amorphous region (right) Spectra of crystalline region.

The Raman spectra of laser-annealed films show two different spectra, one corresponding to the amorphous phase and another corresponding to the crystalline phase. A complete Raman mapping of the area is required to be carried out to find out the fractional crystallized volume. The Raman spectra of NBT thin films are often categorized into four major bands denoted by

A, B, C and D. Each of these bands may be deconvoluted into various peaks representing different vibration modes. The spectrometer used in the present measurement uses a notch filter which eliminates the A band that lies close to the Rayleigh line. The Raman spectra of crystalline material show distinct B and C bands, whereas, in the amorphous phase, the B and C band are combined due to the inherent disorder of the amorphous phase. Thus from the above results of XRD and Raman spectrum for laser-annealed films, the NBT phase formation can be seen. Hence it is possible to state that the phase formation has begun at room temperature.

The above two investigations gave some insights into the laser annealing process with NBT thin films.

6.5 Effect of laser fluence

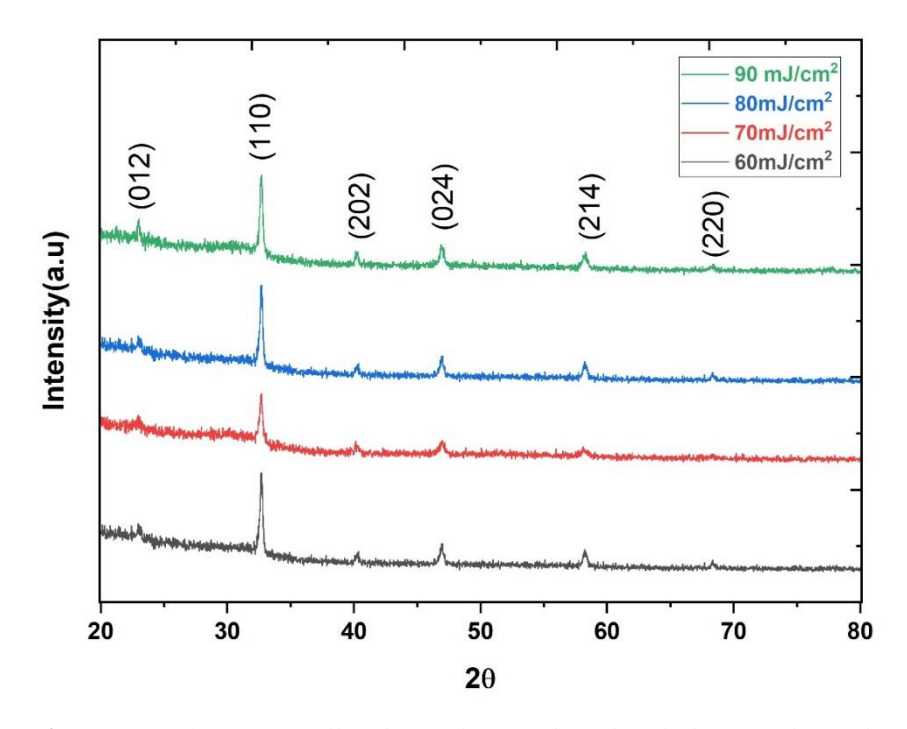


Fig 6.7: XRD of laser crystallized samples irradiated with different laser fluence

In the previous section by varying numbers of laser pulses, what is obtained are partially crystalized NBT thin films, even for 20K laser shots. The optical images of the sample surface indicate that even surface crystallization is incomplete. This suggests that the maximum surface temperature developed during the previous experiment is insufficient to crystallize the NBT

thin films. The laser parameter which influences the developed surface temperature during laser annealing is the laser energy density or laser fluence. Hence the effect of laser fluence is explored here. In this study, a series of amorphous NBT thins film deposited using PLD in the same conditions described in section 6.3 are utilized. In this study, the number of laser annealing shots is fixed to 10,000 (10K) and the laser fluence during the annealing process starting from 60 mJ/cm² to 90 mJ/cm². Similar to the previous laser annealing trials, this is also carried out at room temperature. Fig 6.7 shows the XRD and Fig 6.8 Shows the corresponding optical microscope image of laser annealed samples.

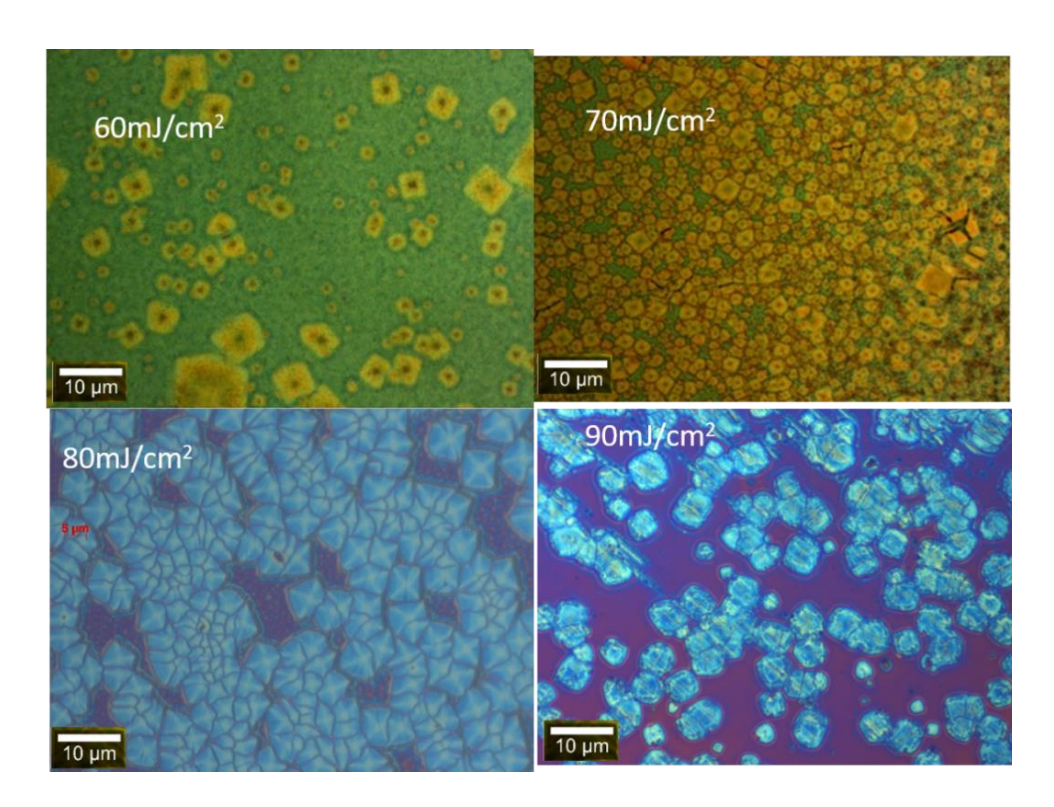


Fig 6.8: Optical images of laser-annealed films for various laser energy densities

The XRD intensity and crystallite size increase with laser fluence but show a dip above 80 mJ/cm². Whereas the optical images show changes in grain shape and damages above 70 mJ/cm². Hence 70 mJ/cm² is chosen as the laser fluences for further investigations. The microwave dielectric characteristics of these films are also measured and tabulated in table 6.2.

Sample/Number of Shots	Microwave dielectric constant	Tan8	Crystallite size (nm) ±2 nm
60 mJ/cm ²	155	0.310	26
70 mJ/cm ²	159	0.317	30.7
80 mJ/cm ²	161	0.423	32.1
90 mJ/cm ²	159	0.416	31.3

Table 6. 2: Microwave dielectric constant and loss of NBT thin film annealed at a different laser fluence.

6.6 Effect of thin film deposition pressure

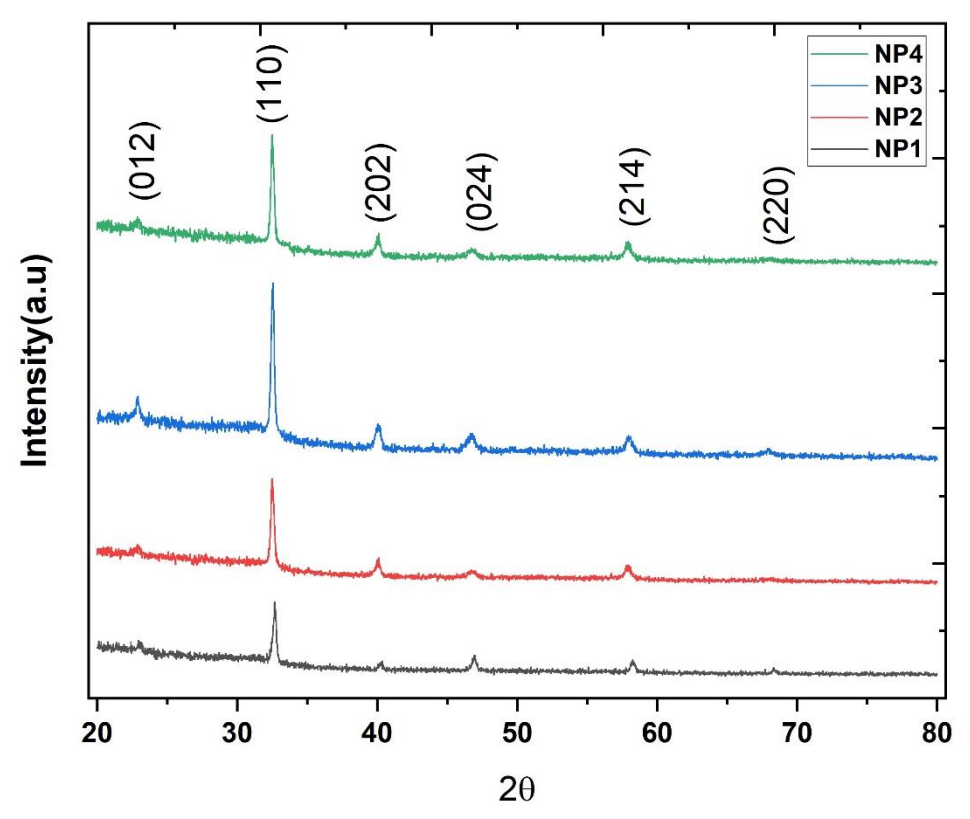


Fig 6.9: XRD pattern of NBT thin film deposited at various pressure and annealed at room temperature

The optimization process performed above reveals that the absorption and transportation of the laser energy by the NBT thin film is not sufficient to crystallize it completely under the

conditions employed. One way to overcome this problem is to heat the substrate and reduce the thermal gradient during the laser annealing. This also may reduce the cooling rate and provide more time for the crystal to grow. If this cooling rate is sufficiently slow, complete crystallization can occur. The reduced thermal gradient may improve the film's overall quality by reducing the possible generation of cracks. But it is a compromise for selective heating and needs an additional heating source. Another approach involves tuning the optical absorption characteristics of the materials

The optical absorption and electrical conductivity of the NBT thin film increase with decreases in working pressure during deposition [19]. Hence the films deposited at low working pressure may show improved crystallization. This is tested by depositing NBT thin films at various pressures in the range 9×10^{-3} mbar to 3×10^{-2} mbar and irradiated for constant number of pulses (10K). The details of sample used in this section is tabulated in Table 6.3

Sample code	Deposition	No pulses for	Deposition
	Pressure (mbar)	annealing	temperature
NP1	3 x10 ⁻²	10 K	300∘C
NP2	1 x10 ⁻²	10 K	
NP3	9 x 10 ⁻³	10 K	
NP4	9 x10 ⁻³	5K	

Table 6. 3: The Deposition pressure and number of annealing pulses.

The XRD analysis of the sample (fig 6.9) shows that the crystallite size and relative intensity of (110) peak increase with a reduction in the deposition pressure. A similar trend is shown by the grain size laser annealed films shown in fig 6.10). The larger grain growth and improved crystallinity may be resulting from the oxygen vacancies present in the films deposited at low pressure. This oxygen vacancy reduces the energy barrier for solid-state diffusion and leads to improved grain growth. Table 6.4 reports the high-frequency dielectric constant and crystallite size of the laser-annealed samples.

The sample NP4 is deposited at same conditions as NP3 but only irradiated with less laser annealing shots (5K). Comparing the microwave dielectric properties and optical images of NP3 and NP4 reveals that 10K laser shots is required to achieve better crystallization.

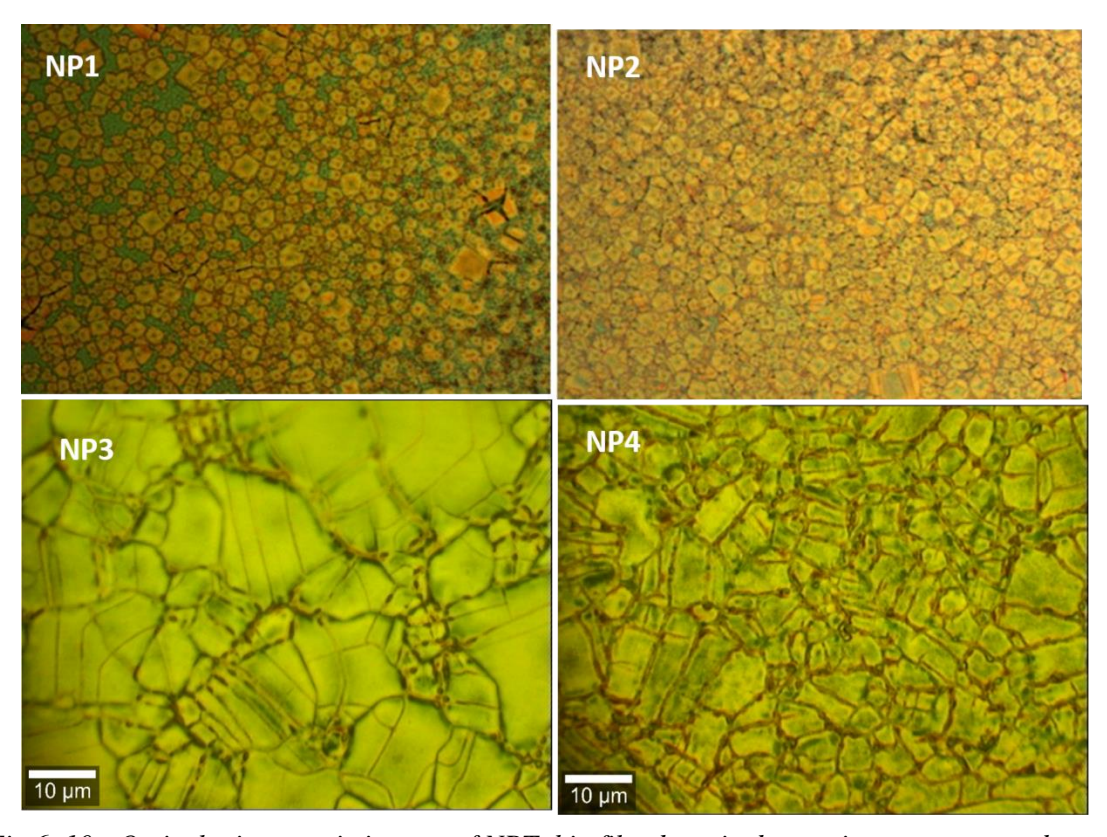


Fig 6. 10: Optical microscopic images of NBT thin film deposited at various pressure and annealed at room temperature.

Sample/Number of Shots	Microwave dielectric constant	Tan8	Crystallite size (nm)
NP1	159	0.317	30.7
NP2	162	0.321	31.4
<u>NP3</u>	<u>170</u>	0.373	34.2
NP4	165	0.361	32.6

Table 6. 4: Microwave dielectric constant and loss of NBT thin film deposited at various pressure and annealed at room temperature.

6.7 Effect of Bismuth deficiency on laser annealing

Sodium bismuth titanate ceramics with Bi deficient phase are known to exhibit oxide ion conduction, and the bismuth-rich phase exhibit mixed ionic and electronic conduction [20]. Hence investigating the effect of laser annealing on bismuth stoichiometry is important.

The Bi deficiency during the thin film deposition may be treated similarly to the Bi₂O₃ loss during ceramic processing, generating oxygen vacancies which are represented in Kroger–Vink notation by [20]

$$2Bi_{Bi}^{\times} + 3O_{O}^{\times} \! \to \! 2V_{Bi}''' + 3V_{O}^{\cdot \prime} + Bi_{2}O_{3}$$

These increased oxygen vacancies promote solid-state diffusion and grain growth, as observed in Bi deficient ceramics and could improve crystallinity during the laser annealing process as well [21]. In the previous chapter, we found that laser fluence during the deposition of NBT thin film significantly influences the bismuth stoichiometry, and bismuth-deficient films are obtained for the film deposited below 1.8 J/cm². Hence we deposited NBT thin films at 300°C at $3x10^{-2}$ mbar working pressure and at a laser fluence of 1.6 J/cm² and 2 J/cm². They were irradiated with 10K laser shot at room temperature.

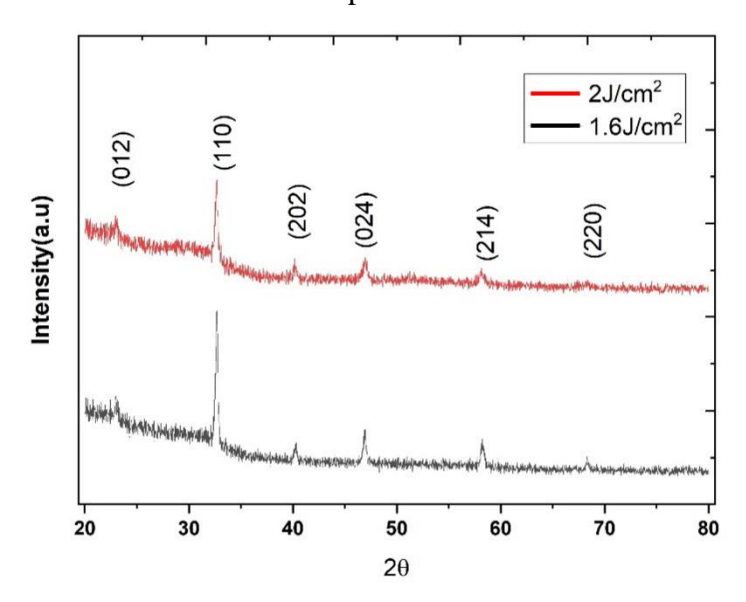


Fig 6. 11: XRD of NBT thin films deposited at various laser fluence and annealed 10K shots at room temperature

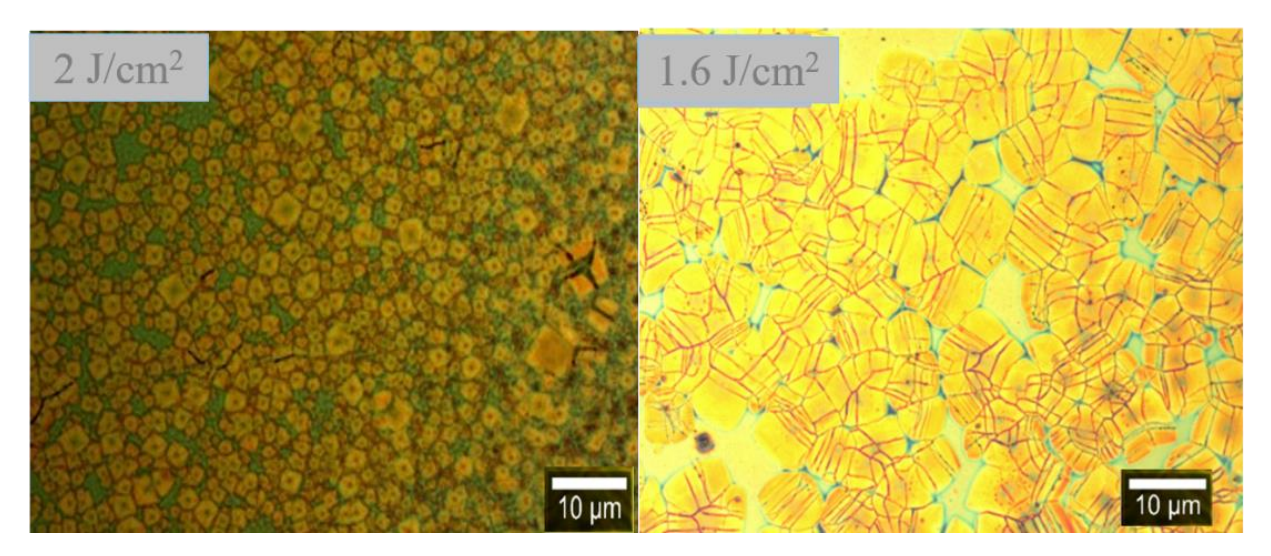


Fig 6. 12: Optical microscopic image of NBT thin films deposited at various laser fluence and annealed with 10K shots at room temperature

Table 6.5 report the crystalline size (calculated for XRD shown in Fig6.11) and microwave dielectric characteristics of NBT thin films deposited at 1.6J/cm² and 2J/cm² at higher working pressure (3x10-² mbar). The films deposited at lower working pressure and the films deposited at lower laser fluence (1.6J/cm²) contain oxygen vacancies. Hence the improvement in the crystallization, as evidenced by the larger crystallite size, grain size (Fig 6.12), and dielectric constant compared to other films, may be the result of enhanced diffusion assisted by the oxygen vacancies. The oxygen vacancies also change the optical absorption and thermal properties of NBT films which may also cause improvement in the reduction of the threshold number of laser shots for crystallization. Further studies are required to distinguish the influence of each of these factors and understand the dynamics of the enhanced crystallization behaviour caused by defects.

Deposition fluence	Annealing	number	Microwave	Tan8	Crystallite size
	fluence	of shots	dielectric		(nm)
			constant		±2 nm
2J/cm ²	70 mJ/cm ²	10,000	159	0.317	30.7
1.6 J/cm ²			164	0.371	34

Table 6. 5: Microwave dielectric constant and loss of NBT thin film deposited at various laser fluence.

6.8 Broadband Microwave Dielectric Properties of Laser annealed films

The comparison of spot frequency dielectric constant, crystallite size, and optical microscope images reveal that the NP3 film (Thickness 200 nm) deposited at 9×10^{-3} mbar shows the best physical properties. Hence, we chose these films to investigate the high-frequency tunability exhibited by laser-annealed films. (Fig 6.13)

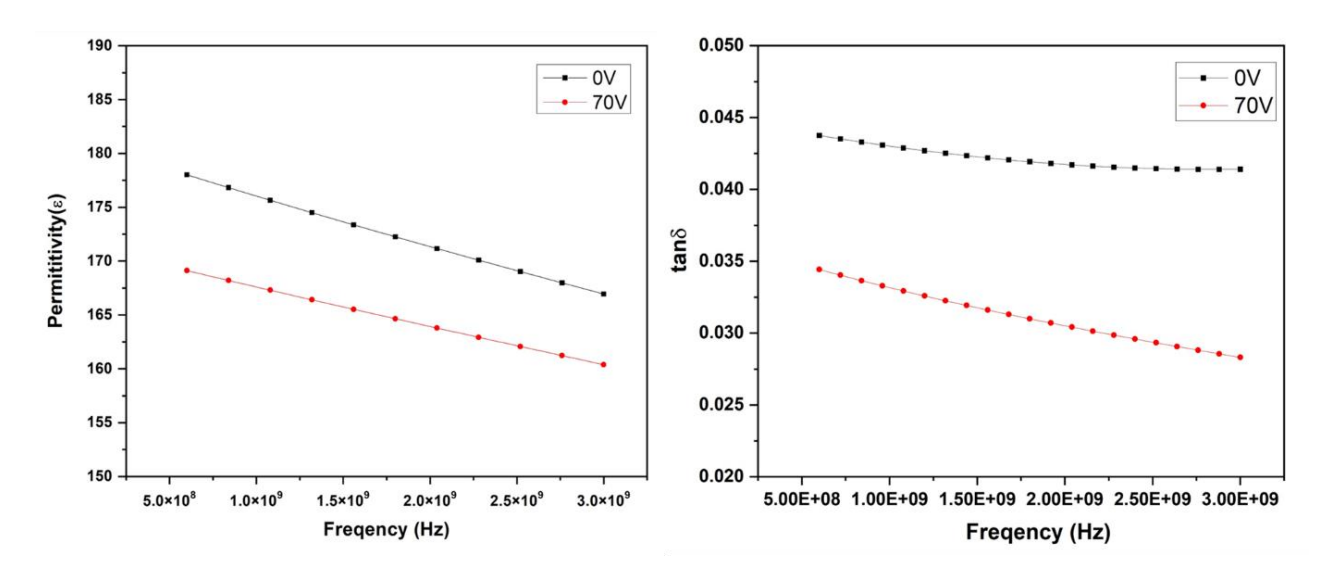


Fig 6. 13: Dielectric constant and dielectric loss (tan δ) of NBT thin films at zero and 70 V bias voltage (E=70 KV/cm) measured from 0.5 GHz to 3 GHz using IDC.

The dielectric properties and tunability obtained for conventionally crystallized and laser-induced crystallized sample are compared in Table 6.5.

Sample	Dielectric constant	Dielectric loss	Relative Tunability
	(Zero bias)	(tan 8) (Zero bias)	
High temperature	214	0.087	9.8 %
annealed			
Laser Annealed at	176	0.043	4.6 %
room temperature			

Table 6.6: High-frequency dielectric properties of laser-annealed and conventionally annealed NBT thin films

The dielectric constant and loss of laser annealed samples are low compared to the hightemperature annealed films. This is the consequence of partial crystallization, both in depth and in area. In laser annealing of thin films, the maximum temperature is attained at the surface, which progressively decreases along the thickness of the sample. Hence the temperature generated by the laser pulses may not create sufficient temperature change in substrate to transform the amorphous film into a crystalline phase. The depth of crystallization of PZT films of thickness 300nm under laser annealing performed by Adarsh R et al. [22] and the laser annealing of BST thin films by J.P. Goud et al. [23] confirm that the depth of crystallization achieved by KrF excimer laser is in the range of 100-140 nm range. The COMSOL Multiphysics simulation carried out by Adarsh et al. for PZT films of thickness 300 nm with an excimer laser of wavelength 248 nm and pulse width of 20 ns and an energy density of 60 mJ/cm² resulted in a peak temperature of 900°C at a depth of 100 nm and 600°C at 200 nm beneath the surface. Microwave tunability of ferroelectric material is a crystalline property. Hence it is heavily influenced by the extent of crystallization and nature of crystallization in the film. Also, other related factors associated with crystallization like the grain size, crystallite size or density also will influence the extent of microwave tunability. The relative extent of tunability of laser annealed films (4.6 %) which is half of the tunability obtained for conventionally crystallized films, also points to the incomplete crystallization of NBT thin films. Cross-sectional TEM and COMSOL Multiphysics simulation will provide a better understanding of the kinematics and depth of crystallization achievable by this process.

6.9 Comparison of laser annealing and microwave furnace annealing of thin films.

Laser-induced crystallization and microwave furnace annealing method are investigated to reduce the crystallization temperature of NBT thin films deposited at 300°C using PLD. In the microwave furnace annealing method, the crystallization initiates around 500°C, which is slightly above the processing temperature requirement for semiconductors and flexible electronic applications. On the other hand, laser-induced crystallization of NBT thin film is carried out at room temperature. The microwave dielectric constant show higher values for microwave-annealed films compared to laser-annealed films, but the grain size follows the opposite trend. This may be due to the fact that dielectric properties represent the bulk crystalline quality of the films. The large grain size may be the result of the very high transient temperature attained during laser annealing.

The microwave annealing process proceeds via dielectric heating from within the material. This results in the homogeneous heating of the sample. The moderate heating rate and uniformity in heating are the primary reasons for the reduction in the processing temperature of microwave-annealed films compared to conventionally crystallized films [24].

Laser energy absorption by material produces a pressure and temperature gradient inside the material, driving the diffusion necessary for crystallization. Femtosecond laser annealing and the recrystallization of ion-implanted semiconductors are explained by the shockwave-based laser-induced lattice mending process [5]. In the lattice mending model, the maximum

amplitude of the shock wave is present below the surface at a depth of approximately three times the optical penetration depth known as characteristic depth. Hence lattice mending of pore or dislocation and laser annealing is expected to be more effective near the characteristic depth. This is because the shock wave directly impinges on the pores near this location and drives rapid solid-state lattice mending. The computational model representing the lattice mending of a nanopore in copper is carried out by P.H Huang et al. [5]. The simulation results of this study demonstrates that the nanopores located at the characteristic depth of 45 nm are mended more effectively than the pores at the surface. Laser annealing studies of ions implanted silicon carbide by K.B. Mulpuri et al. [25] observed a donut-shaped area crystalized by the shock waves and a laser-irradiated area crystallized by bulk type heating.

The other prominent mechanism is the photothermal model used to explain the laser annealing of barium strontium titanate thin films by O. Baldus et al. [2] and the laser annealing of PZT film by S. N. Bharadwaja et al. [26]. According to this model, in nanosecond-pulsed laser annealing, the photothermal effects have been reported to be predominant and heat produced during laser annealing is mainly decided by the optical absorption characteristics of the material. By solving the heat equation for the specific laser and material pairs, the laser-induced temperature profile inside a material may be determined. The higher nucleation rate near the surface of PZT films observed by S. N. Bharadwaja is consistent with their thermal modelling. In our study, the sample area was around 0.5cm², whereas the annealing laser spot was above 2cm²; hence the whole sample is in the region of direct beam irradiation and the use of a photothermal model is appropriate here.

6.10 Conclusion

NBT thin films deposited at 300°C are successfully crystallized at room temperature by irradiating KrF excimer laser of appropriate fluence and number of shots. There is a requirement for a large number of laser shots to crystallize the NBT thin films deposited at

higher oxygen pressure. The extent of crystallization in NBT thin films is improved by (i) deposition of NBT thin films at low oxygen pressure containing a lot of oxygen vacancies and (ii) deposition of amorphous NBT thin film at lower laser fluence containing Bi deficient composition with oxygen vacancy and higher oxygen diffusion rate. This improvement in crystallization may be caused by freely available charge carriers in them. This charge carrier may also contribute to the increases in thermal conductivity and optical absorption leading to better crystallization. The tunability in the dielectric properties in the microwave frequency range for the laser-annealed films are measured by the IDC method. The dielectric tunability of laser-annealed film is half of the conventionally crystallized film of 200nm thickness. This hints that the crystallization achieved by laser annealing is only partial which is also seen from the microstructure and Raman spectra. The room temperature crystallization of NBT opens up the possibility of direct integration of these films in the functional device on polymer and other substrates or processes that are restricted to the lower temperature.

6.11 Reference

- [1] S.C. Lai, H.T. Lue, K.Y. Hsieh, S.L. Lung, R. Liu, T.B. Wu, P.P Donohue and P. Rumsby, J. Appl. Phys. 96, 2779-2784 (2004).
- [2] O. Baldus and R. Waser, J. Eur. Ceram. Soc. 24, 3013-3020 (2004).
- [3] K. Kim and S. Lee, J. App. Phys. 100, 051604 (2006).
- [4] P. Muralt, Integr. Ferroelctr. 17, 297-307 (1997).
- [5] P. H. Huang and H. Y. Lai, Nanotechnology. 19, 255701, 11 (2008).
- [6] J. Romain, Journal de Physique Colloques. 45, C8, 281-289 (1984).
- [7] Y. X. Zhuang, P. F. Xing, H. Y. Shi, J. Chen, P. W. Wang and J. C. He, J. Appl. Phys. 108, 033515 (2010).
- [8] K. Matusita and S. Sakka, Phys. Chem. Glasses. 20, 81 (1979).
- [9] A. Peker and W. L. Johnson, Appl. Phys. Lett. 63, 2342 (1993).
- [10] S. J. Sameehan, A. V. Gkriniari, S. Katakam and N. B. Dahotre, J. Phy. D: Appl. Phy. 48, 49, 495501 (2015).
- [11] H. W. Choi and Y. S. Yang, J. Therm. Anal. Calorim. 119, 2171–2178 (2015).
- [12] R.I. Eglitis, Phase Transit. 86 1115–1120 (2013).
- [13] M.V. Radhika Rao and A.M. Umarji, Bull. Mater. Sci. 20, 1023–1028 (1997).
- [14] R.I. Eglitis, G. Borstel, E. Heifets, S. Piskunov and E. Kotomin, J. Electroceram. 16, 289–292 (2006).
- [15] V. Subrahmanian, B.S. Bellubai and J. Sobhanadri, Rev. Sci. Instrum. 64, 231(1993).
- [16] D.C. Dube, M.T. Lanagan, J. H. Kim and S. J. Jang J. Appl. Phys. 63, 2466 (1988).
- [17] L. F. Chen, C. K. Ong and B. T. G. Tan. IEEE Transaction on instrumentation and measurement, 48, 1031(1999).
- [18] M. A. Rzepecka and M. A. K. Hamid, IEEE Trans. Microw. Theory. Tech. 20, 30 (1972).
- [19] S. Pattipaka, P. Dobbidi, J. P. Goud, K. C. J. Raju, G. Pradhan and V. Sridhar, J. Mater. Sci: Mater. Electron. 33, 8893–8905 (2022).
- [20] T. Zhao, Z. H. Chen, F. Chen, et al. Appl. Phys. Lett. 77, 4338 (2000).
- [21] Y.S. Sung, J.M. Kim, J.H. Cho, T.K. Song, M.H. Kim, and T.G. Park, Appl. Phys. Lett. 98, 012902 (2011).
- [22] A. Rajashekhar and S. T. McKinstry, Pulsed-Laser Crystallization of Ferroelectric/Piezoelectric Oxide Thin Films, Thesis, Pennsylvania State University, May 2017.
- [23] J.P. Goud, A. Kumar, K. Sandeep, S. Ramakanth, P. Ghoshal and K.C.J. Raju, Adv. Electron. Mater, 7, 2000905 (2021)

- [24] A. Bhaskar, H. Y. Chang, T. H. Chang, and S. Y. Cheng, Nanotechnology, 18, 39, 395704 (2007).
- [25] K.B. Mulpuri, S.B. Qadri, J. Grun, C.K. Manka and M.C. Ridgway, Solid-State Electronics, 50, 6,1035 (2006).
- [26] S. S. N. Bharadwaja, J. Kulik, R. Akarapu, H. Beratan and S. Trolier-McKinstry, IEEE Transactions on Ultrasonics, Ferroelectrics, and Frequency Control, 57, 10, 2182 (2010).

Chapter 7 Summary and future work

The key findings from earlier chapters on the impact of deposition parameters on the physical properties of NBT thin films and room-temperature crystallization of NBT thin films deposited at 300°C using the pulsed laser method are covered in this chapter.

7.1 Summary

Initially, the effect of deposition temperature on the structural, microstructural, optical and microwave dielectric characteristics of NBT thin films prepared from the lab-made target was investigated. This investigation shows that NBT films deposited below 550°C were in the amorphous phase, and thin films deposited at 650°C showed a secondary phase due to bismuth volatilization at high temperatures. The crystallite size and unit cell volume increase with deposition temperature showing improved crystallinity. UV- Vis NIR transmission spectra of all the deposited films are measured and used to derive optical characteristics like the refractive index, extinction coefficient, complex dielectric constant, and optical band gap. A single oscillator model with oscillator energies of 5.85 eV for amorphous and 10.37 eV for crystalline NBT thin films, respectively, has been used to explain the observed optical dispersion behaviour. Optical properties of the amorphous and crystalline films show a significant difference in their characteristics, which may arise from the coordination defects and shortrange order in amorphous material. The other important observation is the remarkable difference in the Raman spectra of amorphous and crystalline NBT thin films. This difference is explained based on conservation laws in crystalline solids. The films deposited at 500°C show both amorphous and crystalline region, which is identified by optical microscopy and confirmed by Raman spectroscopy. The microwave frequency dielectric permittivity is determined using the SPDR technique, and the dielectric constant of crystalline films is slightly higher compared to the amorphous thin films.

Then the room-temperature dielectric characteristics of these films are investigated by interdigitated capacitor method. The amorphous films show a smaller dielectric constant, which

gradually increases as the deposition temperature increases. Temperature-dependent impedance data is measured for the NBT films grown on Pt-coated sapphire substrates in optimized conditions. The obtained data is fitted to an equivalent circuit model. Cole-Cole plot of NBT thin films from 50°C and 150°C shows only one depressed semicircle indicating a single major contribution from grain interior. However above 150°C, the grain boundary contribution dominates, which significantly increases with temperature. At microwave frequencies dielectric constant of NBT thin films shows only negligible dispersion and exhibits good tunability. These results indicate that NBT may be considered as an alternative to Ba_{0.5}Sr_{0.5}TiO₃ for tunable microwave devices. The energy storage characteristics of NBT films are estimated from the P-E loop. The NBT films show reasonable storage capacity of a recoverable energy density of 3.5J/cm³. However, the efficiency obtained is 39%, which is rather low compared to the currently used lead-based systems (70%). Hence with further optimization and suitable doping only could replace lead-based ferroelectric systems.

Chapter 5 discusses the effect of microwave annealing and laser energy density used to deposit the thin films on their physical properties. The onset of crystallization temperature of NBT thin films is considerably lower in microwave furnace annealing compared to conventional furnace annealing. The x-ray diffraction studies of the films show that all of the films were crystallized in rhombohedral structure with an R3c space group at room temperature. An increase in annealing temperature improves the crystalline quality of the films, which is evident from the increment in crystallite size and refractive index. The measured optical band gap shows a red shift with a rise in annealing temperature, because of the improved crystallization. The refractive index increases with annealing temperature, which may be understood by the enhanced diffusion with the rise in temperature which leads to improved packing density and thus the refractive index. The effect of laser energy density during thin film deposition on structural, microstructural, compositional and physical properties are investigated for NBT thin

films. The interesting observation was the decrease in the grain size at higher laser fluence. Normally high laser fluence favors grain growth, but we observed the opposite trend, which stems from the higher Bi content at low fluence deposited film, as evident from the compositional analysis. The NBT thin films with correct stoichiometry are obtained for films deposited at $2J/cm^2$.

The crystallization temperature reduction obtained by the microwave annealing method was not that substantial to be utilized for depositing FE thin films on temperature-sensitive substrates hence another method popularly known as laser annealing not widely used in ferroelectric oxides crystallization is investigated. NBT thin films deposited at 300°C is successfully crystalized at room temperature by irradiating KrF excimer laser of appropriate fluence and number of shots. A larger number of laser shots are required to crystalize the films deposited at higher oxygen pressure. A closer observation of their optical images reveals that crystallization in NBT is nucleation limited. and the introduction of defects or seeding layer may significantly enhance the extent of crystallization. This is obtained using two approaches: (i) Deposition of amorphous NBT thin film at lower laser fluence, which creates a Bi deficient composition with improved oxygen diffusion rate. (ii) Deposition of NBT thin films at low working pressure resulting in a lot of oxygen vacancies. In both these cases, we obtain laserannealed NBT thin films of superior quality. This improvement in crystallization may be caused by freely available charge carriers in them, as evident from the higher measured electrical conductivity (dielectric loss). These charge carriers can also contribute to the increase in thermal conductivity and optical absorption.

7.2 Future work

- 1. Deposition and crystallization of NBT thin films on the temperature-sensitive flexible substrate.
- 2. Investigation of dynamics of crystallization using a non-isothermal model.
- 3. Fabrication of various piezoelectric and microwave devices on laser-annealed films.
- 4. Investigation of the effect of other material processing parameters like composition, substrate etc., on the laser annealing process to improve the quality of laser annealed films.
- 5. Laser annealing of other potential ferroelectrics and realizing lead-free devices competent with lead-based systems and compatible with temperature-sensitive substrates.
- 6. Modelling of the laser annealing process using simulation and validating them with experiments to derive a comprehensive physical understanding of the laser annealing process.

The field of laser annealing of ferroelectrics is in its development stage and hence much more investigation in this field will improve the understanding of laser-matter interaction and non-isothermal crystallization and much more interesting Physics.

List of Publications in part of the Thesis

- 1. **Andrews Joseph**, J. Pundareekam Goud, Sivanagi Reddy Emani, K. C. James Raju "Study of amorphous and crystalline phases of sodium bismuth titanate thin films by optical and Raman spectroscopy," J Mater Sci: Mater Electron 28:4362–4370 (2017).
- 2. **Andrews Joseph**, S. R. Emani, and K.C James Raju, Optical properties of sodium bismuth titanate thin films, Ferroelectrics 518 (1), 184 (2017).
- 3. **Andrews Joseph,** K.C James Raju, Effect of ex-situ microwave annealing of NBT thin films (under preparation)
- 4. **Andrews Joseph,** Akhil Raman, Arun B and K.C James Raju The role of laser fluence on the physical properties of NBT thin films (**under preparation**)
- Andrews Joseph and K.C James Raju Excimer laser-induced crystallization of Sodium Bismuth Titanate Thin films (under preparation).

List of Other Publications

- S Pattipaka, Andrews Joseph, Bharti G.P, KC James Raju, Khare, A. Pamu, D. Thickness-dependent microwave dielectric and nonlinear optical properties of Bi0.5Na0.5TiO3 thin films. Appl. Surf. Sci. 2019, 488, 391–403
- S. Manivannan, Andrews Joseph, P.K. Sharma, K.C.J. Raju, D. Das, Ceram. Int. 41, 10923–10933 (2015).
- 8. J. Pundareekam Goud, S Ramakanth, **Andrews Joseph**, Kongbrailatpam Sandeep, G L N Rao, and K C James Raju, "Effect of crystallinity on microwave tunability of Pulsed laser deposited Ba_{0.5}Sr_{0.5}TiO₃ Thin Films" Thin Solid Films 626 126–130 (2017)
- Swathi Manivannan, Andrews Joseph, P.K. Sharma, K.C. James Raju, Dibakar Das,
 Effect of colloidal processing on densification and dielectric properties of
 Ba(Zn_{1/3}Ta_{2/3})O₃ Ceramics, Ceramics International, 43, 15,12658-12666(2017)

- 10. G. Logesh, M. Rashad, M. Lodhe, U. Sabu, Andrews Joseph, K. J. Raju, M. Balasubramanian, Mechanical and dielectric properties of carbon fiber reinforced reaction bonded silicon nitride composites. Journal of Alloys and Compounds, 767 1083-1093 (2018)
- 11. G. Logesh, U. Sabu, C. Srishilan, M. Rashad, Andrews Joseph, K.C. James Raju, M. Balasubramanian, Tunable microwave absorption performance of carbon fiber reinforced reaction bonded silicon nitride composites, J Ceram Int 47 (16) 22540–22549 (2021).
- 12. P. Raju, G. Neeraja Rani, S. Udaya Kumar, Andrews Joseph and K. C. James Raju, ultrasonically induced in situ polymerization of PANI-SWCNT nanocomposites for electromagnetic shielding applications. J Mater Sci: Mater Electron 33, 5138–5148 (2022)
- 13. G. Logesh, C. Srishilan, Ummen Sabu, Kali Prasad, M. Rashad, Andrews Joseph, K.C. James Raju, M. Balasubramanian, Carbon fiber reinforced composites from industrial waste for microwave absorption and electromagnetic interference shielding applications, Ceramics International, 49, 2, 1922-1931 (2023).

Conference Proceedings

- Andrews Joseph, J. Pundareekam Goud, Sivanagi Reddy Emani, and K.C. James Raju
 "Microwave Dielectric and Optical Properties of Pulsed Laser Deposited Na_{0.5}Bi_{0.5}TiO₃
 Thin Film" AIP Conference Proceedings 1731, 080039 (2016).
- J. Pundareekam Goud, Andrews Joseph, S. Ramakanth, Kuna Lakshun Naidu, and K.
 C. James Raju "Microwave dielectric and optical properties of amorphous and crystalline Ba_{0.5}Sr_{0.5}TiO₃ thin films" AIP Conference Proceedings 1728,020293, (2016).

- 3. M.S. Alkathy, **Andrews Joseph**, K.C.J. Raju, Dielectric properties of Zr substituted barium strontium titanate, Mater. Today Proc. 3 (2016) 2321–2328.
- Sivanagi Reddy Emani, Andrews Joseph, K.C James Raju, "Optical and Microwave Properties of CaBi₄Ti₄O₁₅ Ferroelectric Thin Films Deposited by Pulsed Laser Deposition" AIP Conference Proceedings 1731(2016) 080015.

Conferences/Symposium/ Workshops attended

- Andrews Joseph, J. Pundareekam Goud, Sivanagi Reddy Emani and K.C James Raju,
 "Microwave Dielectric And Optical Properties Of Pulsed Laser Deposited
 Na0.5Bi0.5TiO3 Thin Films" 60th DAE Solid State Physics Symposium (DAE-SSPS2015) held at Amity University UP, Noida, Uttar Pradesh during December 21 25, 2015(Poster presentation)
- Andrews Joseph, Processing and Characterization of Thin Films, workshop, UGC-NRC, School of Physics, University of Hyderabad, 2018.
- 3. **Andrews Joseph**, Sivanagi Reddy Emani and K. C. James Raju, "Optical Properties of Sodium Bismuth Titanate Thin Films" ICTAM-AMF10 during 7-11 Nov.2016 at University of Delhi. (Poster presentation)
- J. Pundareekam Goud, Andrews Joseph, S. Ramakanth, Kuna Lakshun Naidu, and K.
 C. James Raju "Microwave dielectric and optical properties of amorphous and crystalline Ba0.5Sr0.5TiO3 thin films", ICC-2015, POSTER presentation.
- 5. Sivanagi Reddy Emani, Andrews Joseph, K.C James Raju "Optical and Microwave Properties of CaBi4Ti4O15 Ferroelectric Thin Films Deposited by Pulsed Laser Deposition" 60th DAE Solid State Physics Symposium (DAE-SSPS-2015) held at Amity University UP, Noida, Uttar Pradesh during December 21-25, 2015. (Poster presentation).

Low-temperature crystallization of sodium Bismuth Titanate thin films

by Andrews Joseph

Condbi Marrari

Indira Gandhi Memorial Library
UNIVERSITY OF HYDERABAD
Central University P.O.
HYDERABAD-500 046

Submission date: 14-Jan-2023 12:12PM (UTC+0530)

Submission ID: 1992661919

File name: Andrews Joseph.pdf (6.53M)

Word count: 23556 Character count: 125531

Low-temperature crystallization of sodium Bismuth Titanate thin films

ORIGINALITY REPORT

SIMILARITY INDEX

2%

INTERNET SOURCES

PUBLICATIONS

STUDENT PAPERS

PRIMARY SOURCES

Andrews Joseph, J. Pundareekam Goud, Sivanagi Reddy Emani, K. C. James Raju. "Study of amorphous and crystalline phases of sodium bismuth titanate thin films by optical and Raman spectroscopy", Journal of Materials Science: Materials in Electronics, 2016

2%

Publication

"Microwave Materials and Applications 2V Set", Wiley, 2017

Publication

<1%

Daryapurkar, A.S., J.T. Kolte, and P. Gopalan. "Influence of oxygen gas pressure on phase, microstructure and electrical properties of sodium bismuth titanate thin films grown using pulsed laser deposition", Thin Solid Films, 2015.

<1%

Publication

Sivanagi Reddy Emani, K. C. James Raju. "Effect of substrate temperature on the

optical properties of CaBi4Ti4O15 thin films deposited by pulsed laser ablation", Journal of Materials Science: Materials in Electronics, 2016

Publication

- dspace.uohyd.ac.in
 Internet Source

 Sameehan S Joshi, Anna V Gkriniari, Shravana
 Katakam, Narendra B Dahotre. "Dynamic
 crystallization during non-isothermal laser
 treatment of Fe–Si–B metallic glass", Journal
 of Physics D: Applied Physics, 2015
 Publication

 <1 %
 - Submitted to University of Hyderabad,
 Hyderabad
 Student Paper

<1%

<1%

A. Rambabu, S. Bashaiah, K. C. James Raju. "Nanomechanical and microwave dielectric properties of SrBi4Ti4O15 thin films sputtered on amorphous substrates by rf sputtering", Journal of Materials Science: Materials in Electronics, 2014

Publication

Daryapurkar, A.S., J.T. Kolte, P.R. Apte, and P. Gopalan. "Structural and electrical properties of sodium bismuth titanate (Na0.5Bi0.5TiO3) thin films optimized using the Taguchi approach", Ceramics International, 2013.

10	K Venkata Saravanan, K Sudheendran, M Ghanashyam Krishna, K C James Raju. " Effect of the amorphous-to-crystalline transition in Ba Sr TiO thin films on optical and microwave dielectric properties ", Journal of Physics D: Applied Physics, 2009 Publication	<1%
11	Linfeng Chen, C.K. Ong, B.T.G. Tan. "Amendment of cavity perturbation method for permittivity measurement of extremely low-loss dielectrics", IEEE Transactions on Instrumentation and Measurement, 1999 Publication	<1%
12	Rajan, G "Engineering of luminescence from Gd"20"3:Eu^3^+ nanophosphors by pulsed laser deposition", Optical Materials, 200911	<1%
13	www.freepatentsonline.com Internet Source	<1%
14	Springer Series in Materials Science, 2014. Publication	<1%
15	archive.org Internet Source	<1%
16	A. S. Daryapurkar, J. T. Kolte, P. Gopalan. "Effect of Barium Titanate buffer layer on dielectric properties of Sodium Bismuth	<1%

Titanate thin films grown using Pulsed Laser Deposition", Proceedings of ISAF-ECAPD-PFM 2012, 2012

Publication

Dinghua Bao. "Band-gap energies of sol-gel-derived SrTiO[sub 3] thin films", Applied Physics Letters, 2001

<1%

Publication

K. Sudheendran, K.C. James Raju. "Influence of Post Deposition Annealing Process on the Optical and Microwave Dielectric Properties of Bi Zn Nb O Thin Films ", Integrated Ferroelectrics, 2010

<1%

Publication

K. Sudheendran. "Effect of process parameters and post-deposition annealing onthemicrowave dielectric and optical properties of pulsed laser deposited Bi1.5Zn1.0Nb1.5O7 thin films", Applied Physics A, 05/2009

<1%

Publication

Venkatachalam, S.. "Preparation and characterization of nano and microcrystalline ZnO thin films by PLD", Current Applied Physics, 200911

<1%

Publication

21 monarch.qucosa.de

Dong Heon Kang, Yong Hee Kang. "Dielectric and Pyroelectric Properties of Lead-Free Sodium Bismuth Titanate Thin Films Due to Excess Sodium and Bismuth Addition", Journal of the Microelectronics and Packaging Society, 2013

<1%

Publication

J. P. Zhao. "Structural and bonding properties of carbon nitride films synthesized by low energy nitrogen-ion-beam-assisted pulsed laser deposition with different laser fluences", Journal of Applied Physics, 2001

<1%

Publication

K. Venkata Saravanan, K. Sudheendran, M. Ghanashyam Krishna, K.C. James Raju, Anil K. Bhatnagar. "Effect of process parameters and post deposition annealing on the optical, structural and microwave dielectric properties of RF magnetron sputtered (Ba0.5,Sr0.5)TiO3 thin films", Vacuum, 2006

<1%

Publication

Y. J. Han, S. F. Huang, C. H. Yang, X. J. Lin, Y. C. Wang, J. H. Song, J. Qian. "The microstructure, insulating and dielectric characteristics of Na0.5Bi0.5TiO3 thin films: role of precursor solution", Journal of Materials Science: Materials in Electronics, 2017

<1%

Publication

26	D. Pamu, K. Sudheendran, M. Ghanashyam Krishna, K. C. J. Raju. "Optical and microwave characteristics of ambient temperature deposited zirconium tin titanate high- films ", The European Physical Journal Applied Physics, 2008 Publication	<1%
27	C-J. Peng, S.B. Krupanidhi. "Structures and electrical properties of barium strontium titanate thin films grown by multi-ion-beam reactive sputtering technique", Journal of Materials Research, 2011 Publication	<1%
28	Shih-Chia Chang, Jeffrey M. Kempisty. "Lift-off Methods for MEMS Devices", MRS Proceedings, 2011 Publication	<1%
29	J. K. Kim, S. S. Kim, M. H. Park, J. W. Kim, E. J. Choi, T. G. Ha, H. K. Cho, R. Guo, A. S. Bhalla. " Effects of Annealing Temperature on the Electrical Properties of Cr-Substituted BiFeO Thin Films ", Ferroelectrics, 2007 Publication	<1%
30	etd.lib.metu.edu.tr Internet Source	<1%

Wei Qin, Yiping Guo, Bing Guo, Mingyuan Gu.

"Dielectric and optical properties of BiFeO3-

<1%

(Na0.5Bi0.5)TiO3 thin films deposited on Si substrate using LaNiO3 as buffer layer for photovoltaic devices", Journal of Alloys and Compounds, 2012

Publication

- baadalsg.inflibnet.ac.in <1% 32 Internet Source "Application of Lasers in Manufacturing", 33 Springer Science and Business Media LLC, 2019 Publication Tsuji, K.. "Grazing-exit electron probe X-ray <1% 34 microanalysis (GE-EPMA): Fundamental and applications", Spectrochimica Acta Part B: Atomic Spectroscopy, 200511 Publication link.springer.com <1% 35 Internet Source <1_% C. Feng, C.H. Yang, Y.Y. Zhou, F.J. Geng, P.P. 36 Lv, Q. Yao. "Substrate-dependent ferroelectric and dielectric properties of Mn doped Na0.5Bi0.5TiO3 thin films derived by chemical solution decomposition", Journal of Alloys and Compounds, 2016 Publication
 - Duclere, J.R.. "Lead-free Na"0"."5Bi"0"."5TiO"3 ferroelectric thin films grown by Pulsed Laser

Deposition on epitaxial platinum bottom electrodes", Thin Solid Films, 20081128

Publication

38	Submitted to Karunya University Student Paper	<1%
39	N. D., R. Birjega, A. Andrei, M. Dinescu, F. Craciun, C. Galassi. "Chapter 8 Phase Transitions, Dielectric and Ferroelectric Properties of Lead-free NBT-BT Thin Films", IntechOpen, 2012 Publication	<1%
40	Suryadi Ismadji, Felycia Edi Soetaredjo, Aning Ayucitra. "Clay Materials for Environmental Remediation", Springer Science and Business Media LLC, 2015 Publication	<1%
41	etd.lis.nsysu.edu.tw Internet Source	<1%
42	Krupka, J "Uncertainty of complex permittivity measurements by split-post dielectric resonator technique", Journal of the European Ceramic Society, 2001 Publication	<1%
43	Submitted to Luton Sixth Form College, Bedfordshire Student Paper	<1%

44	M Hashida. "Carbon-nanotube cathode modified by femtosecond laser ablation", Journal of Physics Conference Series, 04/01/2007 Publication	<1%
45	Ravi Bathe, R.D Vispute, Dan Habersat, R.P Sharma et al. "AlN thin films deposited by pulsed laser ablation, sputtering and filtered arc techniques", Thin Solid Films, 2001 Publication	<1%
46	Zhao Wang, Wei Ren, Xuelei Zhan, Peng Shi, Xiaoqing Wu. "Structure, composition and microwave dielectric properties of bismuth zinc niobate pyrochlore thin films", Journal of Applied Physics, 2014 Publication	<1%
47	etheses.whiterose.ac.uk Internet Source	<1%
48	A. Achiq. "Effects of prior hydrogenation on the structure and properties of thermally nanocrystallized silicon layers", Journal of Applied Physics, 1998 Publication	<1%
49	Submitted to Institute of Graduate Studies, UiTM Student Paper	<1%

- Kong, L.B.. "Electrically tunable dielectric materials and strategies to improve their performances", Progress in Materials Science, 201011

 Publication
- <1%

<1%

- Muhammad Shemyal Nisar, Xiangjie Zhao, An Pan, Shui Yuan, JinSong Xia. "Grating Coupler for an On-Chip Lithium Niobate Ridge Waveguide", IEEE Photonics Journal, 2017
- Rivera, V.A.G., and L.C. Barbosa.
 "Spectroscopic properties of Er3+-doped sodium-modified tellurite glasses for use as optical amplifiers at 1540nm", Journal of Luminescence, 2014.

<1%

Publication

Xianghui Zhou, Holger Geßwein, Mohsen Sazegar, Andre Giere, Florian Paul, Rolf Jakoby, Joachim R. Binder, Jürgen Haußelt. "Characterization of metal (Fe, Co, Ni, Cu) and fluorine codoped barium strontium titanate thick-films for microwave applications", Journal of Electroceramics, 2009

<1%

Z.W. Chen, Z. Jiao, M.H. Wu, C.H. Shek, C.M.L. Wu, J.K.L. Lai. "Microstructural evolution of oxides and semiconductor thin films", Progress in Materials Science, 2011

<1%

Exclude quotes On Exclude matches < 14 words

Exclude bibliography On